

Application of Micro-Rotors to Induce Crystal Nucleation:  
Challenges, Takeaways, and Future Prospects

PhD Thesis

D. Maciver

Chemical and Process Engineering Department

University of Strathclyde, Glasgow

August 14, 2024

This thesis is the result of the author's original research. It has been composed by the author and has not been previously submitted for examination which has led to the award of a degree.

The copyright of this thesis belongs to the author under the terms of the United Kingdom Copyright Acts as qualified by University of Strathclyde Regulation 3.50. Due acknowledgement must always be made of the use of any material contained in, or derived from, this thesis.

# **Abstract**

# Contents

<b>Abstract</b>	<b>ii</b>
<b>List of Figures</b>	<b>vii</b>
<b>List of Tables</b>	<b>xix</b>
<b>Preface/Acknowledgements</b>	<b>xx</b>
<b>1 Introduction</b>	<b>2</b>
1.1 Nucleation . . . . .	3
1.1.1 Primary & Secondary nucleation . . . . .	4
1.2 Nucleation Theories . . . . .	5
1.2.1 Classical Nucleation Theory (CNT) . . . . .	5
1.2.2 Two Step Nucleation . . . . .	8
1.3 Crystallisation methods . . . . .	9
1.3.1 Cooling Crystallisation . . . . .	9
1.3.2 Evaporative Crystallisation . . . . .	10
1.4 Optical Tweezers . . . . .	11

## Contents

1.4.1	Background . . . . .	11
1.4.2	Literature related to laser induced nucleation . . . . .	12
1.4.3	Optical Torque . . . . .	14
1.5	Shear induced Nucleation . . . . .	16
1.6	Aims and Objectives . . . . .	18
<b>2</b>	<b>Theory and methods</b>	<b>19</b>
2.1	Working Principle . . . . .	19
2.2	Electromagnetism and optical tweezing . . . . .	21
2.2.1	Ray-Optics Regime . . . . .	23
2.2.2	Lornez-Mie Theory . . . . .	24
2.2.3	Rayleigh Scattering . . . . .	26
2.3	Scattering methods . . . . .	27
2.3.1	T-matrix Method . . . . .	28
2.3.2	Discrete Dipole Approximation . . . . .	29
2.4	Langevin Equation . . . . .	30
2.4.1	Finite Difference . . . . .	33
2.5	Calibration Techniques . . . . .	35
2.5.1	Potential Well Analysis . . . . .	37
2.5.2	Equipartition method . . . . .	38
2.5.3	Mean Square Displacement . . . . .	39
2.5.4	Power Spectrum Density (PSD) . . . . .	42
2.6	Simulation of spherical aggregates . . . . .	46

## Contents

2.6.1	Simulation parameters . . . . .	49
2.7	Simulated Quadrant Photodiode . . . . .	50
<b>3</b>	<b>Effects of localised shearing on crystal growth and nucleation</b>	<b>55</b>
3.1	Optical Tweezer Equipment . . . . .	57
3.1.1	Position detection methods . . . . .	59
3.1.2	Fourier Optics and 4f correlators . . . . .	61
3.2	Synthesis of Birefringent Micro spheres . . . . .	62
3.2.1	Liquid Crystal Rotors . . . . .	64
3.3	Rotation of birefringent micro spheres . . . . .	65
3.3.1	Estimation of fluid flow around micro-rotors in bulk fluid . . . . .	67
3.4	Micro-rotors in Supersaturated solution . . . . .	69
3.5	Shearing via Galvano-mirror manipulation . . . . .	72
3.6	Nucleation with a Stationary and Moving Beam . . . . .	74
3.6.1	Stationary beam . . . . .	75
3.6.2	Moving Beam . . . . .	75
3.6.3	Direct trapping of Glycine clusters . . . . .	79
3.7	Influence of a moving beam front on seed crystals . . . . .	79
3.8	Summary of Moving Beam Phenomena . . . . .	81
3.9	Conclusion . . . . .	83
<b>4</b>	<b>Complex Langevin dynamics of spherical dimers</b>	<b>84</b>
4.1	Positional and Orientational dependence of Trapping forces . . . . .	85
4.1.1	Non-trivial equilibrium configurations . . . . .	92

## Contents

4.2	Continuous rotational motion due to second-order scattering . . . . .	94
4.2.1	Gyroscopic Precession using asymmetric dimers . . . . .	103
4.3	Characterisation of asymmetric dimers via PSD analysis . . . . .	106
4.4	Conclusions . . . . .	108
<b>5</b>	<b>Detection and Characterisation of rotational spherical aggregate rotational dynamics</b>	<b>110</b>
5.1	Simulative QPD . . . . .	111
5.1.1	Incident beam . . . . .	111
5.1.2	Scattered and Total Fields . . . . .	113
5.2	Rotations and Asymmetric particles . . . . .	118
5.3	Power Spectra of single sphere vs spherical aggregates . . . . .	119
5.4	Monitoring Stochastic rotational motion using static light scattering . .	121
5.4.1	Coordinate System . . . . .	121
5.4.2	Beam . . . . .	121
5.4.3	Dimer . . . . .	122
5.4.4	Detectors and Pixels . . . . .	122
5.5	Interpretation of scattering data into orientation estimates . . . . .	123
5.5.1	Calculation of error . . . . .	127
5.5.2	Brownian Simulation . . . . .	129
5.5.3	Testing the Model . . . . .	131
5.5.4	Asymmetric dimer dynamics . . . . .	134
5.5.5	Accounting for sources of error in light scattering measurements	135

Contents

5.6 Conclusion . . . . .	140
<b>6 Closing Remarks</b>	<b>142</b>
<b>A Stuff That Didn't Fit Anywhere Else</b>	<b>143</b>
<b>Bibliography</b>	<b>143</b>

# List of Figures

1.1 Secondary Nucleation mechanisms, classified by Agrawal and Paterson [Agrawal2015] . . . . .	5
1.2 Free energy diagram of a newly formed nucleus according to the Classical Nucleation Theory. The total free energy (blue) is due to the competition between the volume free energy gain (green) and the interfacial free energy cost (orange). Dotted lines are for a higher supersaturation than the solid lines, the interfacial energy cost is independent of supersaturation.	7
1.3 Typical Concentration vs Temperature plot with the solubility curve (black) and metastable zone (red). 3 different cooling curves are shown as well: a high rate of cooling (orange) shows the mixture quickly dropping below the solubility curve resulting in no new nuclei forming; a low rate of cooling (green) shows the mixture exceeding the metastable zone, where now nucleation occurs freely; and a typical cooling rate (blue) shows how a typical cooling crystalliser will operate, sitting in the middle of the other two curves. . . . .	11

## List of Figures

2.1 Working principle for an optical trap, upper image shows a sphere at the centre of a trap experiences equal forces directed towards inwards. Lower image shows that when displaced 'ray a' is refracted far more than 'ray b' resulting in a net force back towards the centre. . . . .	20
2.2 Example trajectory created using Finite Differences method for a $2\mu m$ diameter sphere. Trap stiffness's were estimated using <i>ott</i> at $\kappa_x = \kappa_y = -100 \text{ pN}/\mu m$ and $\kappa_z = -25 \text{ pN}/\mu m$ . The particle's motion can be localised around the shaded ellipsoid. . . . .	36
2.3 Example mean squared displacement using (2.40), for a $1\mu m$ sphere trapped by an optical potential well. The dotted line represents the upper limit of the sphere's displacement due to the optical trap. . . . .	41
2.4 Example PSD fitted using (2.44), power spectra is collected from an optically trapped silica sphere suspended in water. The difference in magnitude is due to the asymmetry of the quadrant photo diode having a stronger signal response in the direction of the polarisation vector. Using a correction factor (see (??)) will adjust the power spectra to better describe the trap shape. . . . .	44

## List of Figures

2.5 Ray scattering render of both the laboratory frame and particle frame for a dimer and a Gaussian beam. The origin of the laboratory frame is defined as the focus of the trapping beam, with the positive $z$ -axis being aligned with the direction of beam propagation. The particle frame is centered on the dimer's centre of mass with the primary axis $U_z$ being aligned with the centres of the two spheres. Black line is scaled to represent 1 $\mu m$ . . . . .	50
2.6 Total Field incident on the quadrant photo diode for a several different displacements. Top Left: 2 $\mu m$ diameter silica sphere placed at the focus of a beam. Top Right: silica sphere is now displaced by 1 $\mu m$ along the x-axis. Bottom Right: silica sphere is now displaced by 1 $\mu m$ along the y-axis. Bottom Left: silica sphere is now displaced by 0.707 $\mu m$ along the x and y axis. The trapping beam is a $TEM_{00}$ Gaussian, polarised along the along the x-axis. $S_x$ , $S_y$ , and $S_z$ are shown to the right of each graph, $Q_1$ , $Q_2$ , $Q_3$ , and $Q_4$ are shown above each graph. . . . .	53
2.7 Comparison between QPD response signal versus work conducted by Rohrbach, single sphere ( $r = 150 nm$ , $n = 1.57$ ) is scanned by a 1064 nm laser and the QPD signal recorded. Solid lines represent the signal produced by QPD using <i>ott</i> and points represent the signal response collected from [Rohrbach2002]. . . . .	54

## List of Figures

3.1 Optical tweezer set up used for the majority of the PhD. The focal lengths of $f_1$ , $f_2$ , $f_3$ , & $f_4$ are $-20\text{ mm}$ , $60\text{ mm}$ , $150\text{ mm}$ , & $200\text{ mm}$ respectively. Diagram not drawn to scale. . . . .	58
3.2 Comparison between QPD and Lateral effect photodiodes. The four quadrants of a QPD (left) experience different photocurrents based on the total intensity of light incident on each section (labelled A, B, C, D). Whereas a Lateral effect sensor (right) uses the resistive properties of the photodiode surface to vary the create different photocurrents passing through the anodes A, B, C, and D. . . . .	60
3.3 Signal generator galvano mirror controller, channel 1 controls the x-axis mirror, while channel 2 controls the y-axis mirror. Both channels can be manipulated independently. . . . .	61
3.4 (a)Sample Vaterite sphere suspended in water and trapped by circular polarised trap. (b) Collected power spectrum from rotating Vaterite, peaks in the power spectrum appear at integer multiples of the rotational frequency ( $f_{rot} \approx 49.8\text{ Hz}$ ) . . . . .	63
3.5 Liquid crystal undergoing rotation due to the circularly polarised trap. .	65

## List of Figures

3.6 (Top) Fluid flow radiating out from the surface of a rotating Vaterite sphere. (Bottom) Shear rates computed using Eq.3.4, optimal shear rate is of $3000\text{s}^{-1}$ is indicated by the dotted line. Vaterite radii and rotation frequencies are shown, the laser power was kept constant at 450 mW. Reported rotation rates, and their corresponding fluid flow and shear rates, for Vaterite are also plotted alongside lab results. Results from [Parkin2009, Arita2016] are included as well. . . . .	68
3.7 Diagram of optical trapping set up for rotating birefringent particles in a supersaturated solution. Left: side view of the trapping set up showing the location of the trap focus at the edge of the droplet of a supersaturated solution. Right: top down view of the glycine droplet with a trapped birefringent particle shown close to edge of the trap. As the particle rotates the drag force from the surrounding fluid generates a flow field around itself (see Eq. 3.3). . . . .	70
3.8 Shear rate generated by a silica microsphere ( $a = 1.57 \mu\text{m}$ ) in bulk fluid moving at different speeds. The shear rate is calculated using (3.8), with the assumption that the bead is moving in a circular path and so the speed is constant through out its path. . . . .	74
3.9 Laser induced nucleation at the edge of a droplet of supersaturated glycine solution. (b) shows the first instance of a crystal nucleus, growing quickly through (c)-(e) until after 6.665 s the crystal begins to escape the trap. . . . .	76

## List of Figures

3.10 Frames from a longer video depicting the growth of a nucleus using a moving beam. Initially the crystal shape is amorphous (a) but eventually reaches a more regular shape (b). This crystal is still influenced by the optical trap as even when not directly irradiated by the laser the crystal rotates between (c) and (d). When the laser is focused on a corner the crystal growth is localised to that region, resulting in an elongated section forming between frames (e) and (f). . . . .	78
3.11 Frames from a longer video demonstrating the trapping of a glycine droplet. Solution is undersaturated glycine and water ( $S = 0.86$ ), with the laser power set at $750\text{ mW}$ . (a) shows a trapped droplet (outlined in black) being brought into contact with a larger droplet. (b) upon contact a nucleus can be seen between the two droplets. The growth is rather slow with the crystal having no clear defined morphology through (c) and (d). Between frames (e) and (f) the larger droplet finally joins the main crystal. . . . .	80
3.12 Diagram outlining how a moving beam assists in the growth of a crystal nucleus. (a) a crystal nucleus is partially trapped by a moving beam with solute droplets close to its surface. (b) droplets close to the laser focus are drawn in by gradient forces and moved towards the crystal surface. (c) these droplets provide material to the main crystal, resulting in localised growth around the laser focus. (d) eventually the crystal area either fully surrounds the laser focus or the solution surrounding the laser is depleted of solute material. . . . .	82

## List of Figures

4.1	Plots of force vs displacement of the centre of mass of the dimer ( $\mu\text{m}$ ) for the case of a dimer of size ratio 2. (a) is the case where the dimer is in its' 'standard' orientation, where the dimer is trapped at $z = 1.71 \mu\text{m}$ . (b) is the case where the dimer is in its' 'inverted' orientation, the dimer is trapped at two positions: $z = 1.20 \mu\text{m}$ & $z = -1.63 \mu\text{m}$ . On the left are renders to visualise the dimer orientation are shown below each plot. The black lines on each force-curve is a linear fit with the slope being reported as the trap stiffness in the legend. . . . .	88
4.2	Plots of force vs displacement of the dimer's centre of mass spheres, where a positive force indicates the dimer is directed right on the x-axis, and vice versa for a negative force. The same simulation parameters are used here as in fig 4.1(a) and (c). The blue curve representing the force response for a dimer in its standard orientation, orange being the inverted case, and green the same case but placed below the focus. . . .	89
4.3	Equilibrium positions of optically trapped dimers with varying size ratio, dashed lines represent unstable traps whereas solid lines are for stable equilibrium positions. (a) shows that dimers while in their 'standard' orientation will always have a single equilibrium position. (b) shows that when the same dimer is in its' 'inverted' orientation can be trapped in two axial positions, one below the focus and one above the focus. . .	91

## List of Figures

4.4 Map of $z - \theta$ phase space using a dimer of size ratio 2 with a laser power of 500 mW ( $\theta = 0^\circ$ is the 'standard' orientation and $\theta = 180^\circ$ is the 'inverted' orientation). The stable configurations are indicated by the larger circles and the starting conditions are colour coded to match the stable point they end up in. Right hand render shows a dimer in its off-axis configuration. . . . .	93
4.5 Rotation frequency vs component phase difference for differently sized dimers. The solid lines represent the rotation rate experienced while the dimer is in its standard orientation, whereas the solid points are for the case where the orientation is inverted. Laser power = 100 mW. . . . .	96
4.6 Figure reused from [Ruffner2012]. (a) shows how the momentum density of a Gaussian beam is twisted while using circularly polarised light. The top row (figures (b)-(d)) shows a 7 sphere cluster trapped in a circularly polarised beam. Due to the clusters asymmetric susceptibility to polarization the cluster rotates in the $x - y$ plane. Whereas the bottom row (figures (e) - (g)) show the similar results for a single sphere. In this instance the sphere does not rotate but instead orbits the beam axis. In both instances the motion is proportional to the degree of polarisation (see figures (d) and (g)) but for the single sphere this motion is only revealed when using (4.2) & (4.3). Reused with permission from author	97

## List of Figures

4.7 Optical torque experienced by a dimer ( $a_I/a_{II} = 10$ ) and a single isotropic sphere. Both were rotated in the $x - z$ plane and the angle between $U_z$ and the beam axis gives the polar angle. The solid lines denote the torque experienced by the dimer whereas the dashed lines represent the torque experienced by the sphere. . . . .	99
4.8 Rotation rate plotted against dimer size ratio while trapped in a circularly polarised beam; a positive rotation rate indicates clockwise rotation, whereas a negative rotation rate indicates counter-clockwise rotation. The red line is for the case of a dimer in its 'standard' orientation. The blue line is for the case when the dimer is in its 'inverted' orientation while trapped above the focus of the beam. And lastly the green line is for the case when the dimer is in its 'inverted' orientation, but when it is trapped below the focus of the beam. . . . .	100
4.9 Optical torque against polar angle $\theta$ about the three primary axis (top: torque about the x-axis; middle: torque about the y-axis; bottom: torque about the z-axis) on a symmetric dimer in linear, elliptical, and circular polarisation beams. Diagram to the right is for visual clarity about the direction of $\theta$ . . . . .	102

## List of Figures

4.10 3 second trajectory of a dimer ( $a_I/a_{II} = 2$ ) trapped in an off axis orientation with a circularly polarised beam ( $P = 100 \text{ mW}$ ). The far left column depicts the dimer's centre of mass position with time; middle two columns are the $x$ , $y$ , and $z$ components of the vectors $u_x$ and $u_y$ ; last column depicts the components of the vector $u_z$ which defines the dimer's orientation. . . . .	103
4.11 Rotational frequency vs laser power for a dimer in both vertical orientations. . . . .	104
4.12 Recorded power spectra fitted to eq. 2.45, scattered points represents the blocked data ( $n_b = 100$ ). Corner frequency for the Lorentzian curves are reported in the legend. . . . .	107
5.1 (a) Example dimer in orientation $\hat{s}$ , (b) 30 Reference orientations represented by vectors pointing from [0,0,0] to each point . . . . .	124
5.2 (a) Distribution of orientation vectors and (b) their respective scattering signals. Points are coloured according to their distance from the centre of each cluster (red points centred around [0.00, 0.00, 1.00], blue points centred at [0.71, 0.00, 0.71]) . . . . .	126
5.3 Expected scattered signals from reference orientations -see fig 5.1 - when: (a) all three detectors are in the X-Y plane, (b) when 1 detector is raised out of the X-Y plane. . . . .	130

## List of Figures

5.4 Model's estimation of dimer orientation over the simulation time, assuming uniform prior $p(\hat{\mathbf{n}}_\alpha)$ , broken up into x, y, and z components for clarity. Blue line denotes the best result we can achieve (the reference orientation $\hat{\mathbf{n}}_{best}$ that is closest to the actual orientation), orange line denotes the result provided by eq 5.13: where the orange line is not visible, the model's prediction agrees with $\hat{\mathbf{n}}_{best}$ . Dotted black line is the instantaneous orientation $\hat{\mathbf{s}}$ .	132
5.5 Estimation of dimer orientation with $p(\hat{\mathbf{n}}_\alpha)$ defined by Eq (5.17). Blue line denotes the best result we can achieve, orange line denotes the result provided by eq 5.13. Dotted black line is the instantaneous orientation $\hat{\mathbf{s}}$ (see Section ??).	134
5.6 Simulation results of: (a) the dimer's orientation vector with time, (b) the dimer's [x,y,z] position with time.	135
5.7 Model estimates of orientation when neural net has been trained on dimer of size ratio: (a) 1:2 [ $F(K_l) = 9.456$ ], (b) 1:2.05 [ $F(K_l) = 1.324$ ], (c) 1:1.95 [ $F(K_l) = 1.325$ ] ( $n_{refs} = 30$ )	136
5.8 Model estimates of orientation when neural net has been trained on dimer of size ratio: (a) 1:2 [ $F(K_l) = 11.756$ ], (b) 1:2.05 [ $F(K_l) = 1.233$ ], (c) 1:1.95 [ $F(K_l) = 2.128$ ], ( $n_{refs} = 126$ )	137
5.9 Model prediction for signal error of (a) 1% [ $F(K_l) = 7.246$ ], (b) 15% [ $F(K_l) = 0.511$ ], and (c) 25% [ $F(K_l) = 0.536$ ].	138
5.10 Model prediction for signal error of (a) 1% [ $F(K_l) = 4.823$ ], (b) 15% [ $F(K_l) = 1.494$ ], and (c) 25% [ $F(K_l) = 0.882$ ], time averaged over 1 ms .	139

# List of Tables

3.1 Results from rotating Vaterite within supersaturated solution of $H_2O$ and Glycine. Solubility concentration for Glycine at 16° was $C^* = 0.2016g/g$ . . . . .	71
--	----

# Preface/Acknowledgements

I would like to acknowledge...

## Chapter 0. Preface/Acknowledgements

# Chapter 1

## Introduction

Crystallisation is one of the oldest forms of phase separation used by humanity [**Schoen1956**], put simply, it is the formation and growth of a new structured phase within a disordered bulk phase. This has applications in a number of industries such as pharmaceuticals, food production, and electronics [**Myerson2002**]. Where the extraction of dilute materials can help improve product quality while keeping production costs low. The industrialisation of crystallisation has allowed engineers to reliably and efficiently induce the crystal formation within a bulk phase. However, while on a large scale crystallisation is seemingly an understood physical process, just a small amount of investigation into the literature reveals that at a micro scale there is yet to be unifying theory that can accurately explain the process of crystallisation [**Fu2021**]. Of which there two primary areas of focus, nucleation and crystal growth. The latter focusing on how an already stable crystal grows and how it takes on its final shape. Whereas the former is more concerned with which factors contribute to its formation in order to control crystal growth.

The focus of this research is partly based around investigating the impact of a focused electromagnetic (EM) field can influence the nucleation process by inducing shear flow within the bulk phase. This in hope that the localised EM field can be used to study different phenomena in nucleation in order to develop a better understanding of the underlying mechanisms.

## 1.1 Nucleation

Nucleation is an example of a binary phase separation, where a dilute phase is miscible in a bulk phase, more often called the solute and solvent respectively. Because of thermodynamics, the two can only remain in equilibrium while below a specific concentration ( $C_{eq}$ ) - below which the chemical potential  $\mu$  for a miscible solution is greater than the potential required to separate the two phases. Once  $C_{eq}$  is exceeded there is a chemical potential difference driving the solution to separate the two phases. Since different combinations of solute and solvent will have different equilibrium concentrations, researchers often instead measure the ratio between the solute and solvent by using 'supersaturation', one form of measuring supersaturation is shown below [Mullin2001]:

$$S(T) = \frac{C_{sol}}{C_{eq}(T)} \quad (1.1)$$

Where  $C_{sol}$  is just the solute concentration, and  $C_{eq}(T)$  is the equilibrium concentration at temperature  $T$ . While the solution remains supersaturated there is a chemical potential driving force for the solute to coalesce and separate from the solution as an ordered solid, the first formation of the crystal is referred to as the nucleus and under-

## Chapter 1. Introduction

standing its formation of has been the focus of researchers for decades now. Typically, for an industrial crystallisation process the working principle is based on controlling and manipulating the supersaturation of the system. Of course nucleation events in a variety of different situations which each require their own classification.

### 1.1.1 Primary & Secondary nucleation

From an industrial perspective, the nucleation process can be broadly categorised into either primary or secondary nucleation. The former describes the formation of an initial nucleus within the bulk phase, absent of any external stimuli. Primary nucleation is therefore considered stochastic as there is no reliable means of predicting where a nucleus may form, or how long it will take. The only reliable indicator being that higher supersaturations will result in faster nucleation rates. At a small scale one can estimate the nucleation rate by making repeated measurements of sample solutions and seeing how many have nucleated after a given time, giving us a Poisson probability distribution.

$$P(t) = 1 - \exp[-JV(t - t_g)] = \frac{M^*(t)}{M} \quad (1.2)$$

Where  $J$  is the nucleation rate,  $t_g$  is the 'growth time',  $V$  is the volume of the individual samples, and  $M^*(t)$  &  $M$  are the number of nucleated samples and the total number of samples used respectively. While this is useful for studying the effects of different parameters at a small scale, for industrial applications there are too many

## Chapter 1. Introduction

external factors for primary nucleation to be the only

In contrast, secondary nucleation is the result of a initial seed crystal inducing further nucleation within the bulk solution [Botsaris1976], in absence of a seed crystal nucleation is near impossible. The research of Secondary Nucleation is fascinating for its own merits; is it speculated that the supersaturation barrier is non-existent [Cashmore2022], and furthermore there are a multitude of mechanisms that can induce secondary nucleation making it imperative that researchers can control the nucleation rate at an industrial scale.

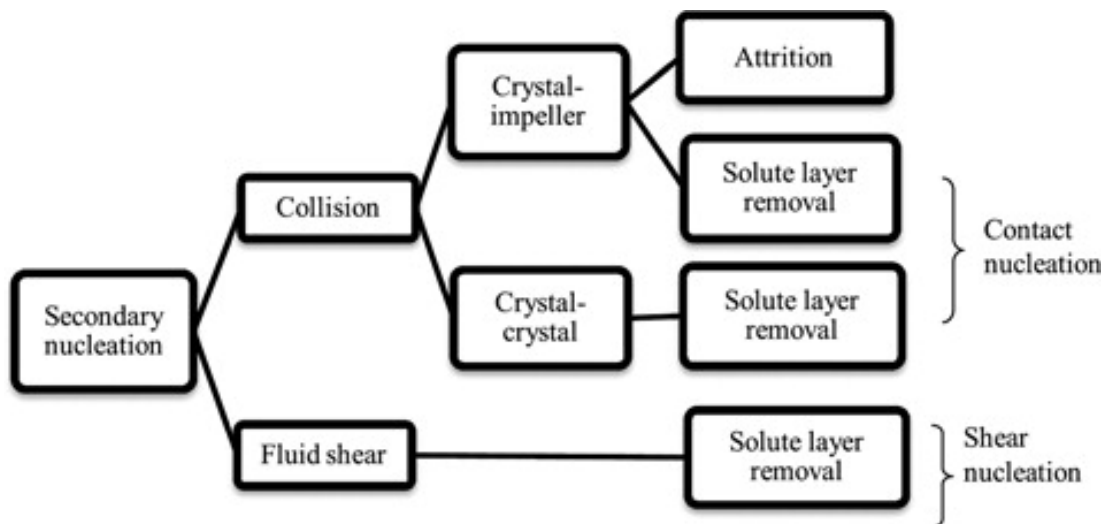


Figure 1.1: Secondary Nucleation mechanisms, classified by Agrawal and Paterson [Agrawal2015]

## 1.2 Nucleation Theories

### 1.2.1 Classical Nucleation Theory (CNT)

Sometimes referred to as 'Gibbs Nucleation Theory' the original theory was first formed from the works of Volmer and Weber, and Frenkel [Frenkel1939, Volmer1926]. While

## Chapter 1. Introduction

initially it was more focused into describing droplet formation in condensing vapours it was extrapolated to describe crystallisation. The central premise of classical theory is that nucleation occurs stochastically due to collisions between individual solute molecules, ions, or atoms. At the same time the bulk phase is resistant to the formation of a new phase. The competition between these random collisions and the bulk solution can be used to predict the probability of a newly formed nucleus.

Consider a supersaturated solution, after some time enough individual sub units collide, forming a nucleus of volume  $4\pi r^3/3$ . The newly formed phase has a lower chemical potential than the surrounding solution, reducing the free energy of the system. Simultaneously, the formation of a new interface is resisted by the bulk phase due to surface tension. The net free energy of the system for a nucleus of radius  $r$  is given as [Karthika2016]:

$$\Delta G = \frac{-4\pi r^3}{3v} k_B T \ln(S) + 4\pi r^2 \sigma_{inf} \quad (1.3)$$

Where  $v$  is the approximate volume of an individual molecule,  $k_B$  is the Boltzmann constant, and  $\sigma_{inf}$  is the interfacial tension of the bulk solution. This assumes that the nucleus will have a spherical morphology so that the surface tension  $\sigma_{inf}$  is a scalar value. Looking at (1.3) suggests that there must be some critical size  $r$  where the free energy gain from the nucleus exceeds the surface tension of the surrounding fluid. Plotting the free energy of the system against nucleus size reveals a critical size above which the gain in free energy exceeds the interfacial tension. Furthermore it shows how increasing the supersaturation of the system reduces said barrier.

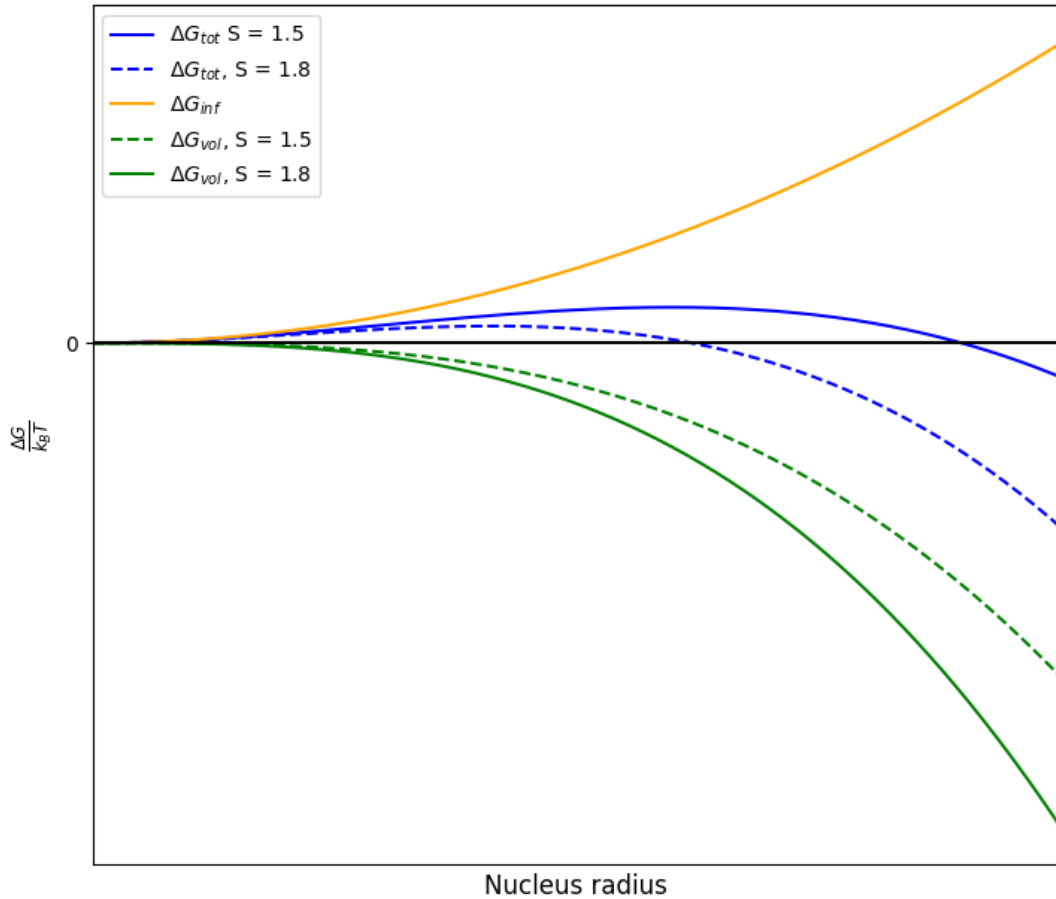


Figure 1.2: Free energy diagram of a newly formed nucleus according to the Classical Nucleation Theory. The total free energy (blue) is due to the competition between the volume free energy gain (green) and the interfacial free energy cost (orange). Dotted lines are for a higher supersaturation than the solid lines, the interfacial energy cost is independent of supersaturation.

The maximum value of  $\Delta G_{tot}$  is the free energy barrier that any newly formed nucleus needs to overcome in order to stabilise. The nucleation rate (the volume of new crystalline material formed per unit time), is therefore commonly defined as being dependent on the energy barrier  $\Delta G^*$ :

$$J = A \exp \left[ -\frac{\Delta G^*}{k_B T} \right] \quad (1.4)$$

## Chapter 1. Introduction

Where  $A$  is a pre-factor that can be fine tuned to the exact demands of the system (typically involving Zeldovich Factor,  $Z$ ) the free energy barrier can be found by finding the turning point of  $\Delta G_{tot}$ .

CNT is often regarded as a good description of the macro system, its obvious that for all crystallization systems there is an inherent energy barrier that dictates the nucleation rate. Where it falters is in its predictive ability, both in estimating nucleation rates [**Gharibeh2005, Vekilov2010**], and in the structure of newly formed nuclei [**Lee1999, Yau2001**]. Recent studies suggest classical nucleation is merely one of many possible pathways that can be taken to produce a structured crystalline phase. Prompting the development of alternative theories to better describe the nucleation process.

### 1.2.2 Two Step Nucleation

The two step nucleation theory is an extension to the CNT, colloid simulations showed that short range (such as in proteins [**Wolde1997, Gliko2005**]) interactions allow for the formation of a liquid-liquid metastable phase from which a new solid phase could form [**Anderson2002, Karthika2016**]. *in situ* techniques for studying nucleation several papers reported the presence of stable liquid-like clusters that formed prior to nucleation [**Savage2009, Wolde1997, Soga1999**]. It can be understood by Oswald's rule [**Ostwald1897**], which says that any crystallising system does not immediately take the path to the lowest possible energy state but instead first transitions to the state with the smallest free energy barrier, further transitions can still occur but this pathway minimises the overall free energy cost. If we consider the free energy diagram

## Chapter 1. Introduction

from before (fig. 1.2) we can consider a case where the supersaturation is low ( $S \approx 1.01$ ) then a dense liquid droplet will have a lower chemical potential than the surrounding fluid but the crystalline phase will have a subsequently lower chemical potential than the dense liquid phase. Initially it was suspected that the formation of the dense liquid phase was a result of stochastic density fluctuations in the system; further simulations suggest that the local bond order is a stronger driving force than the local density [Tan2013].

The current research into two step nucleation (or now more commonly referred to as multi-step nucleation theory) is developing a robust framework to describe what nucleation pathway will occur given the initial conditions. Reviews of all currently documented nucleation pathways identified highlighted the fact the need for the development of *in situ* techniques that can induce nucleation locally but can also reliably identify the nucleation pathway across a broad range of experimental conditions [Karthika2016, Fu2021].

## 1.3 Crystallisation methods

### 1.3.1 Cooling Crystallisation

For some binary mixtures the supersaturation is heavily dependent on the solution temperature, therefore a simple method of producing crystals is by cooling the mixture to induce crystal formation. At ambient temperatures the solute concentration is too high to be fully incorporated into the solution ( $S \gg 1$ ), after heating however the solute is fully dissolved into the solution ( $S < 1$ ). Now as the mixture is allowed to cool to

## Chapter 1. Introduction

room temperature the supersaturation will increase until crystal formation begins, the rate of cooling drastically influencing the size and number of crystals produced.

If  $dT/dt$  is high then the final product will consist of large crystal and be low in number, as the nucleation rate is directly related to the supersaturation only a handful of nuclei can form before the remaining solute grows onto the surface. If  $dT/dt$  is low then the final product will consist of smaller crystals and be far more numerous, as the supersaturation is so large that the new nuclei are forming continuously. Between these two extremes, one can define the meta-stable zone width, a region in the temperature-concentration phase space where both nucleation and crystal growth can be reliably controlled. The lower limit being given by the solubility curve of the binary mixture, and the upper limit being defined by the metastable zone.

The viability of cooling crystallisation is dependent on the meta-stable zone width, too narrow and the process is difficult to control, too wide and the crystal growth rate may be insufficient for the desired outcome.

### 1.3.2 Evaporative Crystallisation

In situations where control of the final product size or shape is not the main focus, often the cheapest method of producing a crystalline product is simply to allow the solvent evaporate and separate from the solute. Depending on the total volume of solvent to evaporate this process can take on time scale of several days to complete.

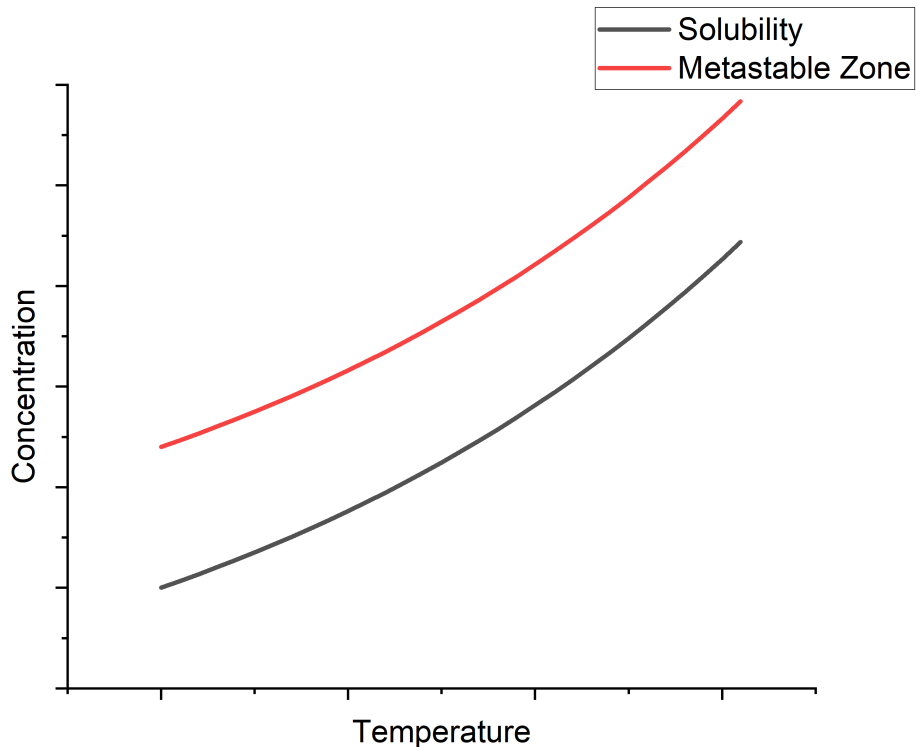


Figure 1.3: Typical Concentration vs Temperature plot with the solubility curve (black) and metastable zone (red). 3 different cooling curves are shown as well: a high rate of cooling (orange) shows the mixture quickly dropping below the solubility curve resulting in no new nuclei forming; a low rate of cooling (green) shows the mixture exceeding the metastable zone, where now nucleation occurs freely; and a typical cooling rate (blue) shows how a typical cooling crystalliser will operate, sitting in the middle of the other two curves.

## 1.4 Optical Tweezers

### 1.4.1 Background

Optical tweezing has been a field of applied optics ever since the 1970s when Ashkin [Ashkin1970] first showed that focused light was capable of trapping micron sized particles due to light exerting 'radiation pressure'. The working principle was that a light source such as a laser could trap small objects within a 2D plane, as long as the

## Chapter 1. Introduction

light source had an approximately Gaussian profile. Soon after, Ashkin showed that the introduction of a microscope objective would allow one to focus the light source to a diffraction limited point that would stably trap small objects within a confined volume [Ashkin1980]. This allowed Ashkin and others to study biological material and would later be used to probe microscopic properties such as the formation of colloidal aggregates [Yi2021] to the drag forces exerted by a pure vacuum [Ahn2018, Monteiro2018]. Due to the predictable behaviour of light, optical tweezers have become essential for measuring and exerting precise forces on the magnitude of pico-newtons allowing one to probe the material properties of the smallest materials.

### 1.4.2 Literature related to laser induced nucleation

From as early as 1996 it has been known that laser irradiation is a viable method of inducing nucleation within a supersaturated solution [Garetz1996], the first reported case was notable as it used a  $1.064 \mu m$  laser meaning it was unlikely to be a photo-chemical reaction but rather a physical one. Future research has found nucleation can be induced by 1 of 3 routes involving direct laser induction: firstly, Non-photochemical laser induced nucleation (NPLIN) where the solution is irradiated with a pulsed laser [Garetz1996, Garetz2002, Sun2006], several papers have debated the exact mechanism that induces NPLIN [Garetz2002, Knott2011]. Two suggested hypothesis are: an optical Kerr effect, where the solute molecules are aligned to lower the nucleation barrier [Knott2011]; a dielectric polarisation effect, in which solute clusters are stabilised within the electric field which drastically increases the likelihood of nucleation[Alexander2008]. Both hypothesis have their limitations and there has

## Chapter 1. Introduction

yet to be a single theory that explains NLPIN thoroughly. In either case the mean pulse intensity needs to be kept relatively low (on the order of  $0.1 - 0.01\text{GW}/\text{cm}^2$ ), as high intensity pulses lead to a completely different nucleation mechanism.

High intensity laser induced nucleation (HILIN), where the pulse intensity is on the order of several  $\text{PW}/\text{cm}^2$  is far simpler a mechanism to explain in comparison to NPLIN. The production of nuclei can be wholly associated to a cavitation process within the target solution, where the laser focus results in thermo-cavitation and the subsequent pressure change leads to a nucleation event around the focus of the laser [ , ]. There is still not a general consensus on how cavitation influences the local supersaturation [ , ], nor is there a clear understanding of what properties of the crystal can be controlled [ , ]. It has been suggested that in theory any solution can undergo HILIN [ ], proving such a theory requires a strong understanding of the phenomena both before and after cavitation occurs.

Lastly, there is trapping induced nucleation, this is where optical tweezers come into play, the optical trap has been shown to have different effects on supersaturated solutions depending on where it has been focused. When focusing on the cover slip, supersaturated solutions of glycine and  $D_2O$  were shown to create a dense liquid droplet of glycine and water [ , ], applying DLS analysis showed that the dense liquid region was populated by clusters that would consolidate together upon being focused by the optical trap [ ]. Molecular simulations of glycine solutions showed that these clusters are unstable when using pure glycine below the saturation point [ ] suggesting that the clusters are formed due to glycine reaction products. When the optical trap was moved from the cover slip to the air-solution interface nucleation would occur before

a dense liquid region could form [ ]. Repeated experiments where the laser is focused on the air-solution interface have lead to a variety of different nucleation events. In some instances the nucleation occurs spontaneously after a short period of time [ ]; whereas allowing a solution to age results in the formation of amorphous precursors that when irradiated will nucleate immediately [ ]. The precursors are only seen when the solution is irradiated by an optical tweezer and the growth rate can be controlled somewhat by varying the laser power [ ]. Notably the only work has been done with simply irradiating the solution with a trapping potential, there has not been an attempt to introduce a trappable object into the solution, the trapping potential has been used to influence the growth of a crystal front [ ].

### 1.4.3 Optical Torque

For any electromagnetic field it is possible to transfer both linear and angular momentum [**Beth1936MechanicalDA**]; more accurately the field is said to have both orbital and spin momentum. Though there is some debate on how to decompose the total momentum into these two components [**Bruce2020, Svak2018**], for this thesis we do not need to calculate the exact quantities and will instead look at the broader effects of both components. Orbital angular momentum arises from the shape of the wavefront of the particular field in question; for simple Gaussian beams the wavefronts are uniform and equally spaced resulting in the typical radiation pressure that Ashkin and co demonstrated [**Ashkin1980**]. However, higher order modes of a Gaussian beam (for example: Laguerre-Gaussian modes) have non-uniform wave fronts meaning the orbital momentum has both angular and linear components; depending on the relative size of

## Chapter 1. Introduction

the target particle one can induce rotation, or orbiting [**Bruce2020, Courtial2000**].

Spin angular momentum (SAM) is attributed to the spin density of the field, early research has shown that the spin density is non-zero for any beam despite the fact that the total SAM transferred to a medium is 0 [**Svak2018, Bliokh2014**]. This has sparked debate if SAM is even a physical quantity as it does not aid in the transport of energy directly [**Bliokh2014**] and so cannot be directly observed in some cases despite being non-zero. This paradox is resolved by representing the wave as an array of spin momentum loops that all together cancel one-another out when the medium is homogeneous. Spacial inhomogeneities cause these spin loops to no longer be equal, resulting in non-zero spin density, anisotropic mediums (such as birefringent crystal lattices) experience a transfer of spin angular momentum allowing for optical torque transfer. It has even been shown that in the case of homogeneous spheres, the spin component of a focused beam can result in additional orbital angular momentum via spin-to-orbital conversion [**Yevick2017**].

Birefringence is a material property often seen in crystalline materials, if the crystal lattice has a different structures when viewed at different orientations then light will be refracted differently depending on its polarisation. For circularly polarised light the inhomogeneity results in a high degree of SAM being transferred to the target object [**Parkin2009, Arita2016**], this has been exploited to rotate microspheres as fast as 1000 Hz while suspended in a bulk medium [**Arita2016**] as well as a means of measuring the local temperature and shear response of said medium [**Millen2014, RodriguezSevilla2018**]. Calculating the optical torque applied to a birefringent material is given via:

$$\begin{aligned}\tau_{opt} = & -\frac{\epsilon}{2\omega_{laser}} E_0^2 \sin(kd(\Delta n)) \cos 2\theta \sin 2\phi \\ & + \frac{\epsilon}{2\omega_{laser}} E_0^2 (1 - \cos(kd(\Delta n)) \sin 2\phi)\end{aligned}\quad (1.5)$$

Where  $\theta$  is the angle between the particle's long axis and the Poynting vector of the local EM field, and  $\phi$  is the phase shift in the EM field. The first term represents the 'orientational' torque which is due to the target particle being aligned along the EM field, when aligned  $\theta = 0$  meaning the entire term is negligible for particle's with a stable orientation. The second term is due purely to the polarisation of the optical trap, for circularly polarised light  $\phi = \pi/4$  thus maximising the torque transferred to the target particle. Birefringence can also be induced if the target particle has an anisotropic shape, in particular if the particle shape is elongated along one major axis; the go to particle shape is a silica dimer (two spheres tangentially attached) due to silica's stability and strong adhesion. Using a silica dimer research groups have achieved a rotation frequency in the realm of several GHz [**Ahn2018**] in a vacuum.

## 1.5 Shear induced Nucleation

It has long been known that fluid shear rate plays a role in influencing nucleation; however, the exact relationship between shear rate and nucleation rate has only been recently understood for specific solutions. Theoretical research into shear induced nucleation suggests that there should be a slight increase in the nucleation rate at low shear rates, reaching a maximum increase in nucleation rate, and then at higher shear rates the nucleation rate begins to drop off. This has been shown theoretically for both simple colloidal [**Mura2016**, **Debuyschere2023**, **Richard2015**] and ice crys-

## Chapter 1. Introduction

tal formation [**Goswami2020**]; however, no experimental work into these systems has been conducted to prove this is the case. There is some experimental evidence for this phenomena in simple salt and protein solutions - though the authors emphasise that mechanical agitation cannot be ruled out - there has not been a exhaustive study into the shearing effects apart from in glycine solutions. In [**Debuysschere2023**] it was found that a shear rate of around  $3000\text{ s}^{-1}$  was the maximum shear rate that would yield the highest nucleation rate. Using the theoretical model established in [**Mura2016, 2001**] which modifies the CNT to account for the effects of a nucleus undergoing shearing, accounting for the fact that a nucleus' growth is undergoing competition between flow-mediated molecular transport and the strain applied by the flow field which inhibits the growth of the nucleus. There central conclusion (from both the theoretical and experimental results) is that there is an optimal shear rate in which the nucleation rate is maximised. However, a question that arises from this result, if there is a optimal shear rate in which molecular transport is maximised and strain is minimised, then surely there should also be a shear rate in which the molecular transport and strain are equal - allowing one to suspend a nucleus at a constant radius. In this scenario, the molecular transport would prevent the nucleus from dissolving, but the strain would prevent the nucleus from growing. This however would require one to be able to apply a continuous shear rate to a targeted nucleus with high precision, there is also no model for an individual nucleus undergoing growth.

## 1.6 Aims and Objectives

Overall the aim of the PhD is to study viability of using micro-rotors to generate localised fluid flow around the beam focus. The results are reported in chapter 3, this is then succeeded by experimental work where we instead use a galvano-mirror to generate shear flow. While overall unsuccessful the addition of a moving beam focus showed that the growth of a nucleus can be localised around the trap focus.

In addition, computer simulations studying the dynamics of asymmetric dimers and their applications as complex micro-rotors are discussed in chapter 4. Lastly two novel methods of measuring rotational motion are discussed in chapter 5; firstly via a novel detection fibre method that allows for instantaneous measurements of the orientational behaviour of optically trapped ellipsoids/dimers; and secondly we create a simulative quadrant photo diode that replicates laboratory results, utilising linear regression techniques we measure the change in orientation in order to measure the optical torque applied to a non-birefringent particle.

# Chapter 2

## Theory and methods

The two key areas of this project cover two widely different fields; crystallisation theory, which is covered in the previous introduction section, and tweezing theory. The following chapter summarises the working principles behind optical tweezing, the work being done with optical tweezers in particle classification, and how tweezing has been used to investigate nucleation events.

### 2.1 Working Principle

Optical tweezing operates on the principle that light carries both linear and angular momentum, which can be transferred to other objects. If light is reflected or refracted by a medium part of the light's momentum is transferred to the medium itself. While at large scales this effect is insignificant in most cases, at micron scales the forces imparted by individual photons begin to become significant enough to influence the trajectory of individual particles. Ashkin's work into optical tweezing found that micron sized entities could be spatially locked by aiming a laser with a Gaussian intensity profile

## Chapter 2. Theory and methods

directly upward at a particle while being suspended in a liquid medium [Ashkin1970].

This is demonstrated in fig. 2.1 where we have a simple sphere trapped by a circularly symmetrical beam with the intensity falling off from the centre in a normal distribution (commonly referred to as a Gaussian beam). If we consider two rays of light hitting our sphere we see that while in the centre each ray is refracted in an equal opposite direction to one another and so the net force imparted is 0. When displaced in the x-y plane the net force is unbalanced and points towards the centre of the trap. This principle can be generalised to 3 degrees of freedom if we consider a focused beam instead of a para-axial beam, typically the trap will be weaker along the beam axis compared to the transverse trap strength.

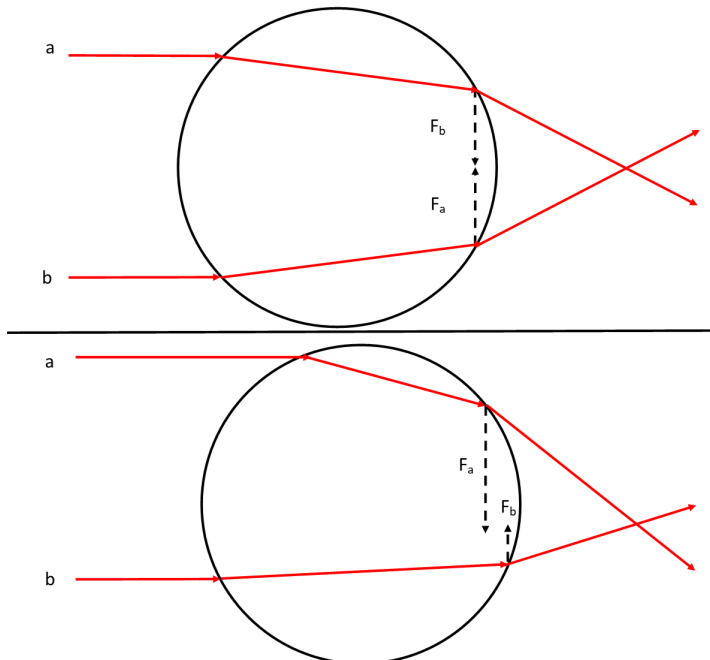


Figure 2.1: Working principle for an optical trap, upper image shows a sphere at the centre of a trap experiences equal forces directed towards inwards. Lower image shows that when displaced 'ray a' is refracted far more than 'ray b' resulting in a net force back towards the centre.

## 2.2 Electromagnetism and optical tweezing

Proper understanding of optical tweezing requires an understanding of how the trapped particle interacts with the trapping laser. From an electromagnetism perspective the laser creates a spatially and temporally coherent electric field that scatters light off of a trapped particle. The laws governing electric and magnetic fields are summarised most succinctly via the Maxwell equations. The differential forms of which are given below

[Jackson 1975]:

$$\nabla \cdot \mathbf{E} = \frac{\rho_v}{\epsilon_0} \quad (2.1)$$

$$\nabla \cdot \mathbf{B} = 0 \quad (2.2)$$

$$\nabla \times \mathbf{E} = -\frac{\partial \mathbf{B}}{\partial t} \quad (2.3)$$

$$\nabla \times \mathbf{B} = \mathbf{j} + \frac{\partial \mathbf{E}}{\partial t} \quad (2.4)$$

where  $\rho_v$  is the free charge density,  $\mathbf{j}_0$  is the charge current, and  $\epsilon_0$  is the permittivity of free space.

These four equations describe how the electric and magnetic fields behave and relate to one another at a microscopic level. Any discussion of optical trapping is underpinned by the fact that in all cases the Maxwell equations must be satisfied at the macroscopic level, where one must account for the medium's interactions with the

## Chapter 2. Theory and methods

EM field. Macroscopic forms of the Maxwell equations are given below [**Jackson'1975**]:

$$\nabla \cdot \mathbf{D} = \rho_f \quad (2.5)$$

$$\nabla \cdot \mathbf{B} = 0 \quad (2.6)$$

$$\nabla \times \mathbf{E} = \frac{\partial \mathbf{B}}{\partial t} \quad (2.7)$$

$$\nabla \times \mathbf{H} = \mathbf{J}_f + \frac{\partial \mathbf{D}}{\partial t} \quad (2.8)$$

Where  $\rho_f$  and  $\mathbf{J}_f$  are the charge density and current caused by the presence of free charges in the medium, and  $\mathbf{D}$  and  $\mathbf{H}$  are the displacement and magnetising fields respectively. The latter two are defined by:

$$\mathbf{D} = \epsilon_0 \mathbf{E} + \mathbf{P}$$

$$\mathbf{H} = \frac{1}{\mu_0} \mathbf{B} - \mathbf{M}$$

Where  $\mathbf{P}$  is the polarization field and  $\mathbf{M}$  is the magnetisation field, these fields arise due to the bound charges throughout the medium interacting with the EM field.

The force exerted by an optical tweezer can be subdivided into the gradient and scattering components, for most modelling research this is how the force fields are reported. The gradient force is a conservative force brought about by the polarisation of dielectric materials which is directed towards the point of maximum intensity (for a simple Gaussian beam this would be at it's focal point) [**YasuhiroHarada1996**].

Typically, optical tweezers will utilise higher numerical aperture lenses in order to increase the intensity, thus allowing for stronger gradient forces.

## Chapter 2. Theory and methods

The scattering force arises from the scattered field of the trapping beam pushing the target object away from the focal point. The equilibrium position (where the mean squared displacement is minimised) is found when the gradient force far exceeds the both the scattering force, and the thermal energy of the particle. Describing and calculating the optical forces is dependent on the ratio between the particle size and the trapping wavelength.

### 2.2.1 Ray-Optics Regime

The Ray-Optics model is the simplest to understand, this theory models the laser as a collection of individual 'rays' that propagate and are refracted according to Snell's Law. Based on the change in direction momentum is transferred to the target particle; with rays closest to the centre of the beam having greater intensity than those rays at the very edge of the beam. Consider a particle struck by two rays in a Gaussian beam (see Fig below), one coming close to the centre, and the other ray coming from the edge. As each ray is refracted by the target sphere a force is imparted onto it, the total force imparted is given by:

$$F_i = Q_i \frac{\Delta n P_i}{c} \quad (2.9)$$

where  $Q_i$  is the trapping efficiency,  $\Delta n$  is the difference in refractive indices between the solution and the target particle, and  $P_i$  is the power of the individual ray. The net force can be subdivided into its gradient and scattering components, where the latter directs the particle to the centre of the beam, and the latter acts on the particle in the

## Chapter 2. Theory and methods

direction of beam propagation. For a beam with a Gaussian intensity distribution  $P_i$  will fall off as you move from the centre of the beam. The ray optics model is ideal when dealing with larger particles whose diameter far exceed the wavelength of light being scattered. While it can be useful in predicting the forces experienced by said particle's it does not fully capture the behaviour of light when considering interference between different rays.

### 2.2.2 Lorenz-Mie Theory

The Lorenz-Mie theory provides an exact solution to the Maxwell equations for the scattering caused by an isotropic sphere. This theory describes the scattered wave given off by a dielectric sphere when incident by a plane wave as a summation of partial spherical waves. For any spherical wave the vector fields must solve the Helmholtz wave equation given by:

$$\nabla^2 \mathbf{E} + k^2 \mathbf{E} = 0 \quad (2.10)$$

Where  $k$  is the wave number of the electromagnetic radiation ( $k = 2\pi/\lambda$ ). This combined with the constraints of Maxwell's equations leaves very few exact solutions apart from spherical or planar waves, both of which can be converted between with relative ease. For example, a plane wave electric field can be expanded into spherical harmonics and likewise any spherical wave can be described as a combination of plane waves offset from one another. For a single plane wave the incident, internal, and

## Chapter 2. Theory and methods

scattered fields are given as:

$$\mathbf{E}_{\text{inc}}(\mathbf{r}) = E_0 \sum_{nm}^{\infty} \left[ a_{nm} \mathbf{M}_{nm}^{(1)}(\mathbf{r}) + b_{nm} \mathbf{N}_{nm}^{(1)}(\mathbf{r}) \right] \quad (2.11)$$

$$\mathbf{E}_{\text{int}}(\mathbf{r}) = E_0 \sum_{n=1}^{\infty} i^n \frac{2n+1}{n(n+1)} \left[ -id_{nm} \mathbf{N}_{nm}^{(1)}(\mathbf{r}) + c_{nm} \mathbf{M}_{nm}^{(1)}(\mathbf{r}) \right] \quad (2.12)$$

$$\mathbf{E}_{\text{scat}}(\mathbf{r}) = E_0 \sum_{n=1}^{\infty} i^n \frac{2n+1}{n(n+1)} \left[ -ip_{nm} \mathbf{N}_{nm}^{(3)}(\mathbf{r}) + q_{nm} \mathbf{M}_{nm}^{(3)}(\mathbf{r}) \right] \quad (2.13)$$

$$\mathbf{E}_{\text{tot}}(\mathbf{r}) = \begin{cases} \mathbf{E}_{\text{inc}}(\mathbf{r}) + \mathbf{E}_{\text{scat}}(\mathbf{r}) & \text{if } \mathbf{r} \text{ outside} \\ \mathbf{E}_{\text{int}}(\mathbf{r}) & \text{if } \mathbf{r} \text{ inside} \end{cases} \quad (2.14)$$

where  $a_{nm}$ ,  $b_{nm}$ ,  $c_{nm}$ ,  $d_{nm}$ ,  $p_{nm}$ , and  $q_{nm}$  are the expansion coefficients of each of the fields, and  $M_{nm}^{(1)}$  and  $N_{nm}^{(1)}$  are the vector spherical harmonics. For the incident field computing its expansion coefficients is possible via analytical methods and are completely dependent on the beam conditions imposed by the user. However, computing the expansion coefficients of the internal and scattered fields is far more tedious depending on the shape of the target and what properties of the scattered field are desired — see sec. 2.3. From an optical trapping perspective the force exerted by a focused electric field can be found by computing the Maxwell stress tensor which only requires the total magnitude of the incident and scattered fields. By computing the momentum contained in the incident and scattered fields we can measure the total momentum transferred to the target particle.

Lorenz-Mie theory can be applied to describe the scattering from any particle regardless of size, though as the size of the target particle changes - relative to the light being scattered - the theory describing the scattered light is better approximated by

## Chapter 2. Theory and methods

alternative theories. For particles that are far larger than the wavelength of light the scattering is best described by the Ray-Optics theory. In the opposite case the target particle is better approximated as a single electric dipole as described by the Rayleigh scattering field.

### 2.2.3 Rayleigh Scattering

The Rayleigh approximation is the limiting approximation for describing a particles motion in an electromagnetic field whose wavelength is several times greater than the particle's size. The underlying theory is that a dielectric sphere can be treated as a dipole while in the presence of the electromagnetic field; in which case the scattering force is given simply by the scattering of the induced dipole, and the gradient force is due to the Lorentz force [**Gordon1973**]. The gradient forces in the principle Cartesian axis are described by Harada et al [**YasuhiroHarada1996**] in MKS units as a restorative rectangular force field:

$$F_{grad,x} = -\hat{x} \frac{2\pi n_2 a^3}{c} \left( \frac{m^2 - 1}{m^2 + 2} \right) \frac{4\tilde{x}/w_0}{1 + (2\tilde{z})^2} \times I(r) \quad (2.15)$$

$$F_{grad,y} = -\hat{y} \frac{2\pi n_2 a^3}{c} \left( \frac{m^2 - 1}{m^2 + 2} \right) \frac{4\tilde{y}/w_0}{1 + (2\tilde{z})^2} \times I(r) \quad (2.16)$$

$$\begin{aligned} F_{grad,z} = & -\hat{z} \frac{2\pi n_2 a^3}{c} \left( \frac{m^2 - 1}{m^2 + 2} \right) \frac{4\tilde{z}/w_0}{1 + (2\tilde{z})^2} \times I(r) \\ & \times \left[ 1 - \frac{2(\tilde{x}^2 + \tilde{y}^2)}{1 + (2\tilde{z})^2} \right] \end{aligned} \quad (2.17)$$

where:

$$I(r) = \left( \frac{2P}{\pi w_0^2} \right) \frac{1}{1 + (2\tilde{z})^2} \exp \left[ -\frac{2(\tilde{x}^2 + \tilde{y}^2)}{1 + (2\tilde{z})^2} \right] \quad (2.18)$$

## Chapter 2. Theory and methods

Where  $m$  is the relative refractive index ( $n_1/n_2$ ),  $\omega_0$  is the beam waist, and  $a$  is the radius of the particle. The scattering force however, is dependent on the effective scattering cross-sectional area.

$$F_{\text{scat}} = \hat{z} \left( \frac{n_2}{2} \right) C_{pr} I(r) \quad (2.19)$$

where:

$$C_{pr} = \frac{8}{3} \pi (ka)^4 a^2 \left( \frac{m^2 - 1}{m^2 + 2} \right)^2 \quad (2.20)$$

The Rayleigh regime allows for easy computation of the gradient and scattering forces due to the assumption that the particle is a point dipole. So much so that higher order scattering problems can be simplified by subdividing the particle into discrete dipoles (see Sec 2.3). However, as the target particle gets larger this assumption fails to accurately describe the trapping force due to the complexity in the gradient field. For particle sizes close to the laser wavelength the scattered field is best described by Lorenz-Mie theory.

### 2.3 Scattering methods

There are several methods available to calculate the scattered field produced by a particle. While one can compute this by directly applying Lorenz-Mie theory, describing the interactions between focused beams and complicated shapes can be computationally slow and memory intensive. As a result, several alternative scattering approaches have been developed that allow for faster computation times simplifying the scattering problem.

### 2.3.1 T-matrix Method

The  $T$ -matrix method was first developed by Peter Waterman with his research into acoustic wave scattering [Waterman1969], this would later be extended to electromagnetic waves. Sometimes referred to as the extended boundary condition method (ECBM), the method replaces the scatterer with a series of surface currents over the targets surface. These currents are chosen so that the electromagnetic field outside is identical to the original problem [Wriedt1998]. This choice of currents negates the need to compute the internal fields which reduces the scattering problem to a system of linear equations relating the incident beam coefficients to the scattered beam coefficients. The relationship between each can be summarised as:

$$\begin{pmatrix} q_{mn} \\ p_{mn} \end{pmatrix} = \mathbf{T} \begin{pmatrix} a_{mn} \\ b_{mn} \end{pmatrix} = \begin{pmatrix} T_{11} & T_{12} \\ T_{21} & T_{22} \end{pmatrix} \begin{pmatrix} a_{mn} \\ b_{mn} \end{pmatrix} \quad (2.21)$$

Where  $q_{mn}$ , and  $p_{mn}$  are the scattering beam coefficients, and  $a_{mn}$ , and  $b_{mn}$  are the coefficients of the incident beam. For this project we utilised an extension of the ECBM known as multi-sphere  $T$ -matrix method (*mstm*). Developed by Mackowski [Mackowski2011] the computational code computes the scattered field from each sphere within the target cluster and the incident field itself. The scattering between spheres slowly converges to a final result but modern codes truncate the calculations to an upper number of iterations (denoted by  $N_{max}$ ) to fit a desired accuracy and computational time.

The  $T$ -matrix method is exceptionally useful for computing the scattering from any

arbitrary spherical aggregate. However, the  $T$ -matrix method by itself can be computationally taxing as the number of spheres increases [Mackowski2011]. While it is possible to solve for the full electromagnetic field of each the entire cluster this is only applicable for a single orientation and can be even slower for large aggregates [Mackowski1996, Xu1995]. The benefit of *mstm* is that the major scattering properties (scattering and extinction cross sections, scattering matrices, etc) can all be computed both for single orientations, or averaged over multiple orientations to determine the average scattering from the target particle.

### 2.3.2 Discrete Dipole Approximation

The discrete dipole approximation (DDA) is a general method that can be applied to the scattering from particles of arbitrary composition and geometry. Developed by Purcell and Pennypacker [Purcell1973], the DDA method approximates the particle as being constructed of dipoles. Each dipole interacts with both the incident field and the scattered fields from every other dipole surrounding it. The resulting scattered field is identical to the scattered field produced by direct integration of Eq. (2.12) throughout the full particle volume [Goedecke1988]. The integral form for the internal electric field inside a scatterer is given as:

$$\mathbf{E}(\mathbf{r}) = \mathbf{E}_{\text{inc}}(\mathbf{r}) + \int_{V/V_0} d^3 r' \bar{\mathbf{G}}(\mathbf{r}, \mathbf{r}') \chi(\mathbf{r}') \mathbf{E}(\mathbf{r}') \quad (2.22)$$

Where  $\bar{\mathbf{G}}$  is the Greens dyadic function of free space, which defines the impulse response between two separate dipoles; and  $\chi$  is the susceptibility of the medium,

which describes the degree of polarisation of the medium in the presence of an electric field. With the internal field calculated, the scattered field can be computed, one of the primary advantages of DDA over the T-matrix method is that the composition of the target can be changed freely. When comparing different computational scattering methods, the ECBM was found to be better suited for simulating the scattering of symmetric targets as the ECBM can use the target's symmetry to speed up calculations [Wriedt1998]. But when dealing with inhomogeneous media DDA is more efficient compared to ECBM.

## 2.4 Langevin Equation

Describing any microscopic motion requires an understanding of a molecules diffusive behaviour, for the case of optical tweezers the most complete model of diffusion is the Langevin equation. Models such as the Fickian, and Einstein derivations are sufficient for macroscopic behaviours the Langevin equation better describes the microscopic characteristics of any diffusive behaviour.

The Fickian model describes the net flux of solute molecules into a finite volume of fluid being proportional to the density gradient  $\delta\rho(u, t)/\delta u$  [Gillespie2012]. It assumes that the solute molecules do not collide with one another or with molecules in the solution; overall, the Fickian model is used to describe how solute molecules disperse over long periods of time. It does not provide any incite into the forces acting on individual molecules, whereas the Langevin model captures the physical interactions between an individual molecule and the surrounding fluid over a wide range of time

## Chapter 2. Theory and methods

scales.

The Einstein model of diffusion expands upon the Fickian model by considering the collisions between individual molecules. If we consider a single particle suspended in a solution it will experience multiple collisions with other molecules [Gillespie2012a] over a given time interval  $\delta t$ . The Einstein molecule allows us to consider how individual molecules behave while suspended in a surrounding fluid. Where it begins to falter is when we consider bringing  $\delta t$  to 0; in this scenario the molecule experiences not many but only individual collisions. The Einstein model does not consider the inertia of the molecule in question and so for very short time frames the model implies that the molecule's velocity changes instantly after each collision [Gillespie2012a, Gillespie2012b]. Furthermore, the kinetic energy of each collision is not limited by the thermal energy of the system, meaning that using the Einstein model to predict a particle's trajectory to an finite degree of accuracy implies that the particle has infinite kinetic energy [Gillespie2012b]. This failure to describe motion over smaller time frames is addressed in the Langevin model by accounting for the fluid drag of the system, where any sudden change in velocity must result in a proportionally opposed drag force [Gillespie2012c].

The Langevin model of diffusion assumes that the net force on a particular particle is described fully by these individual collisions [Gillespie2012c]. Unlike the Fickian model it provides a full description of the interactions between the target molecule and the surrounding fluid; while also being able to describe its motion over any time scale,

## Chapter 2. Theory and methods

unlike the Einstein model:

$$m \frac{dv}{dt} + \gamma_0 v + F(t) = W(t) \quad (2.23)$$

Where the first term accounts for inertial forces, the second term accounts for friction forces which counteract the particles current motion ( $\gamma_0$  is the friction coefficient), and the final term accounts for the random Brownian force. The  $F(t)$  is there for convention which accounts for any external forces acting on the particle. We can say that the noise term  $W(t)$  has a Gaussian probability, with a correlation function of:

$$W(t) = \sqrt{2k_B T \gamma_0} \eta(t) \quad (2.24)$$

$$\langle W_i(t) W_j(t') \rangle = 2k_B T \gamma_0 \delta(t - t') \quad (2.25)$$

The Langevin model can be extrapolated to describe the diffusive behaviour of an overall system, but for this project we can instead consider the behaviour of some particle with a diffusion tensor  $D$  suspended in a viscous fluid and spacially localised by an optical potential with trap strength  $\kappa$ . Assuming the only external force acting on our particle is the laser, the net force should be exactly equal to force of the stochastic collisions due to the fluids thermal energy. If we focus our analysis when the particle is stably trapped and assume that the trap is harmonic, we can model the trapping force as a Hookean spring ( $F(t) \approx \kappa x(t)$ ). The full Langevin equation for an optically

trapped particle is therefore given as:

$$m \frac{\delta^2 x(t)}{\delta t^2} + \gamma_0 \frac{\delta x(t)}{\delta t} + \kappa_x x(t) = \sqrt{2k_B T} \eta(t) \quad (2.26)$$

(2.26) provides an accurate description of strongly trapped particles. Despite this the analytical solution of the Langevin equation requires integration of the noise term making it difficult to simulate the trajectory of a given particle [Volpe2013]. Instead, it is often far easier to solve the equation numerically and use the analytical solution to calibrate and extract information about the particle and fluid, and how the two interact with the optical trap.

#### 2.4.1 Finite Difference

The Finite Difference approach involves discretizing the time and spatial elements in order to approximate the higher order terms. If we assume that  $x(t)$  is differentiable to n (we can find its  $n^{th}$  derivative) then we can use the Taylor series expansion to get:

$$x(t + \Delta t) = x(t) + \frac{x'(t)}{1!} \Delta t + \frac{x''(t)}{2!} \Delta t^2 + \dots + \frac{x^n(t)}{n!} \Delta t^n + R_n(x(t)) \quad (2.27)$$

Where  $R_n(x(t))$  is the remainder term between the Taylor expansion to term n and the actual expression. If we limit our approach to the first derivative only, we find that for sufficiently small values of  $R_1$  the velocity and acceleration can be approximated

## Chapter 2. Theory and methods

as:

$$x'(t) \approx \frac{x(t + \Delta t) - x(t)}{\Delta t} \quad (2.28)$$

$$x''(t) \approx \frac{x'(t + \Delta t) - x'(t)}{\Delta t} = \frac{x(t) - 2x(t + \Delta t) + x(t + 2\Delta t)}{\Delta t^2} \quad (2.29)$$

By reversing the time step (i.e. use  $-\Delta t$ ) to approximate the velocity and acceleration based on the previous time steps, we can discretise the position by taking finitely small time steps (i.e.  $x(t) = x_i$ ,  $x(t - \Delta t) = x_{i-1}$ ). The same cannot be done for noise, as no information is known about  $W(t)$  at any time. We can instead say that the velocity of a Brownian particle should approximate our noise as a random walk, where at each new time step, the position changes randomly within a given range. Constricting the variance to  $\sqrt{2D}/\Delta t$  allows us to represent the noise using the finite-difference approach as:

$$m \frac{x_i - 2x_{i-1} + x_{i-2}}{\Delta t^2} = -\gamma \frac{x_i - x_{i-1}}{\Delta t} + \sqrt{2k_B T \gamma} \frac{w_i}{\sqrt{\Delta t}} \quad (2.30)$$

Where  $w_i$  is a random real number between -1 and 1, we can say that it is normally distributed around 0 for simulation purposes. We can rearrange this for  $x_i$  to approximate the Brownian motion of a particle (setting  $x_0 = 0$ ), where the characteristic time is  $\tau = m/\gamma$ . Now in the case of an optical trap, the restoration time scale is given by  $\tau_{OT} = \kappa_x/\gamma$  which for strongly trapped particles is far greater than the characteristic time. Therefore for simulation purposes, we can neglect the particle's inertia which

## Chapter 2. Theory and methods

allows the motion of an optically trapped particle to be written as:

$$x_i = x_{i-1} - \tau_{OT} x_{i-1} \Delta t + \sqrt{2D\Delta t} w_i \quad (2.31)$$

This result can be generalised for a 3-dimensional description of an optically trapped particle, where each Cartesian direction has its own unique characteristic restoration time. We see from the result that trajectory is dependent on only a handful of factors, the trap stiffness  $\kappa_x$ , the fluid viscosity  $\gamma$ , and the thermal energy of the system  $k_B T$  (with the latter two being related by Einstein's formulation of the diffusion coefficient  $D = k_B T / \gamma$ ). Therefore, by calculating these parameters to a high degree of precision allows one to get a precise description of the forces experienced by a target particle, which in the past has been used for highly accurate force transduction [BergSoerensen2004, Smith2003].

## 2.5 Calibration Techniques

There are several approaches for calibrating and characterizing the optical trap, each approach has its drawbacks and benefits so each option should be chosen based on what elements want to be characterized. The basis for each of these methods stems from the analytical solution of the Langevin equation:

$$x(t) = x(0)e^{-t/\tau_{OT}} + \sqrt{2D} \int_0^t ds W_x(s) e^{-(t-s)/\tau_{OT}} \quad (2.32)$$

Positional data is often acquired in an experimental setting either using image

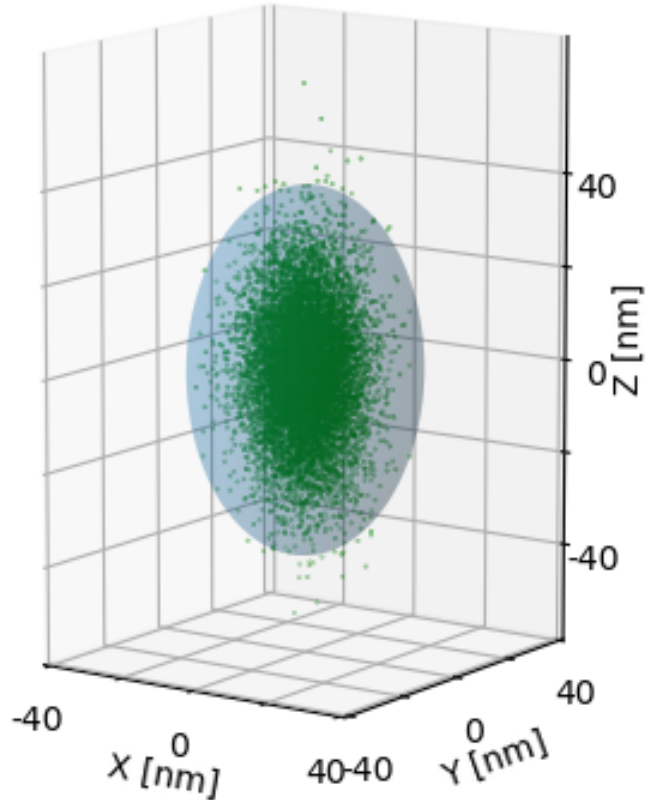


Figure 2.2: Example trajectory created using Finite Differences method for a  $2\mu m$  diameter sphere. Trap stiffness's were estimated using *ott* at  $\kappa_x = \kappa_y = -100\text{ pN}/\mu m$  and  $\kappa_z = -25\text{ pN}/\mu m$ . The particle's motion can be localised around the shaded ellipsoid.

analysis or photodiodes to infer the particles position relative to the beam focus. The former is often used in cases when precision is not a key concern, as often a standard CCD camera will have limited spacial and temporal resolution. The latter method often requires the use of a quadrant photo diode(QPD), the data provided by the QPD will often need to be converted to physical units to compute the force directly - see Eq. (2.46).

### 2.5.1 Potential Well Analysis

The Langevin equation for an optically trapped assumes that the trap acts similar to a Hookean spring that creates a potential well about its centre. Therefore a simple analysis method is to understand the height and width of said potential well.

Potential analysis is a useful technique for estimating the strength of an optical trap; this method assumes that the force acting on the particle is purely conservative, an accurate presupposition if we ignore the motion of the particle as it enters the trap. This is because the scattering force is far more significant far away from the potential well and is negligible if the trap strength is much greater than the thermal fluctuations. With this in mind we can write the probability of finding the particle at position  $x$  as:

$$\frac{\rho(x)}{\rho_0} = e^{-\frac{U(x)}{k_B T}} \quad (2.33)$$

which therefore means we can write the potential well as:

$$U(x) = -k_B T \ln \left( \frac{\rho(x)}{\rho_0} \right) \quad (2.34)$$

Now assuming our laser acts as a Gaussian beam we should be able to describe the probability distribution  $\rho(x)$  centred at some equilibrium position  $x_0$ :

$$\rho(x) = \sqrt{\frac{\kappa_x}{2\pi k_B T}} \exp \left( -\frac{\kappa_x}{2k_B T} (x - x_{eq})^2 \right) \quad (2.35)$$

By inserting (2.35) into (2.34) we can fit the potential well in order to determine the trap strength  $\kappa_x$ , and an estimation of the equilibrium position  $x_{eq}$ . This has

## Chapter 2. Theory and methods

some limitations in that the large fluctuations can throw off the fit meaning a longer acquisition time is necessary to properly fit the potential well, making it difficult to characterise weakly trapped particles who may not remain trapped for long. It also provides no information on the particle itself (i.e. the friction coefficient  $\gamma$  and diffusion coefficient  $D$ ).

### 2.5.2 Equipartition method

The Equipartition method is by far the fastest and simplest means for estimating the trap strength but unlike Potential Analysis is limited strictly to harmonic potentials. This can be often not the case for highly focused beams, as the trap strength can vary due to polarisation differences. Simply put we can use the equipartition theorem to relate the potential well to the particle's thermal energy using (2.35):

$$\langle U(x) \rangle = \frac{1}{2} \kappa_x \langle (x - x_{eq})^2 \rangle = \int_{-\infty}^{\infty} \rho(x) (x - x_{eq})^2 = \frac{1}{2} k_B T \quad (2.36)$$

$$\implies \kappa_x = \frac{k_B T}{\langle (x - x_{eq})^2 \rangle} \quad (2.37)$$

By taking a time average over multiple trajectories to get  $\langle x - x_{eq} \rangle$  we can get a fairly accurate estimation of the trap strength. Because of this requires a time average of the particle's displacement any large errors in the position measurement can have knock-on effects. Likewise with the potential analysis route, no information is gleaned about the particle itself.

### 2.5.3 Mean Square Displacement

Mean square displacement (MSD) is a common means of describing the random motion of a given particle (or group of particles). This is useful information if say for example we want to understand reaction kinetics on the surface of a catalyst, if we know how far its likely to move from the surface we can tell if its likely to react when a catalytic site becomes available. As it pertains to colloids, consider a suspension of silica spheres immersed in a fluid undergoing Brownian motion (as described by the Langevin Equation) so that:

$$mx''(t) + \gamma x'(t) = \eta(t) \quad (2.38)$$

Where  $\gamma$  is the objects friction coefficient which for spheres is given as  $\gamma = 6\pi\eta r$ , and  $\eta(t)$  is a random white noise variable that is directly related to the thermal energy of the surrounding fluid. If the motion is truly random then we should see an average displacement of 0 regardless of how long we measure for. If we wish to understand the effects of a given external factor (i.e. an electric field or localised heating), simply looking at displacement will reveal nothing of value as its difficult to differentiate between diffusive and a biased motion.

For each sphere we can record its position in the  $x - y$  plane and measure its displacement from a set reference point; for example with an optical tweezer this could be the beam focus. We can measure the MSD by forming a 'window' between two points in time of the trajectory (i.e.  $t & t + \tau$ ) and sliding this window along the entire trajectory length - to eliminate -ve displacements we take the square - we can then take

## Chapter 2. Theory and methods

the average of this series. Repeating over a range of time lags allows us to describe the MSD as a function of  $\tau$ :

$$MSD(\tau) = \langle |x(t + \tau) - x(t)|^2 \rangle \quad (2.39)$$

If we use (2.32) for an optical tweezer we can expand out the squared term to get an analytical expression for the MSD as a function of time lags:

$$MSD(\tau) = \langle |x(t + \tau)^2 - 2x(t + \tau)x(t) + x(t)^2| \rangle = \frac{2k_B T}{\kappa_x} \left[ 1 - e^{-\frac{\tau}{\tau_{OT}}} \right] \quad (2.40)$$

From this expression it's evident that the mean squared displacement increases with larger values of  $\tau$  until it reaches a maximum value as shown below by the dotted line.

The MSD plot can be subdivided into two regimes, when  $\tau \gg \tau_{OT}$  the particle is experiencing the harmonic potential described by the equipartition theorem, and when  $\tau \ll \tau_{OT}$  the particle is said to be freely diffusing within the trap focus. Of course for a freely diffusing object the MSD will never reach a plateau value, comparing MSD's for different particles provides a simple visual indicator of the difference in trapping strength. The MSD method is an already very versatile analytical tool for diffusive motion, however it is rather slow in computing time meaning it is only really beneficial when a high degree of accuracy is required and shorter time resolutions are unavailable - such as using a quadrant photo diode instead or a high speed CCD.

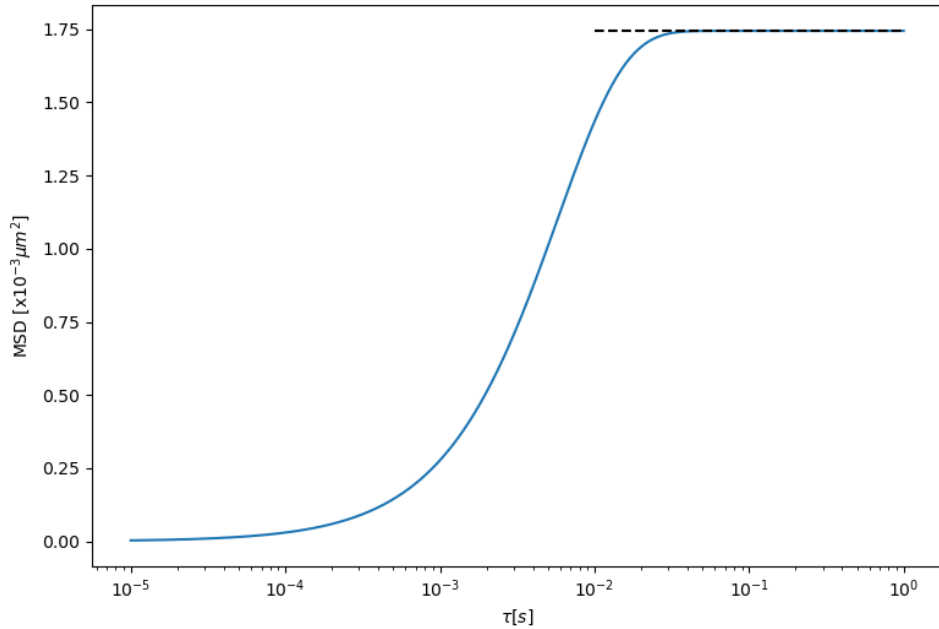


Figure 2.3: Example mean squared displacement using (2.40), for a  $1\mu\text{m}$  sphere trapped by an optical potential well. The dotted line represents the upper limit of the sphere's displacement due to the optical trap.

#### 2.5.3.1 Angular Mean Square Displacement (MSAD)

It is also possible to plot the angular MSD (MSAD) using simulative data, however using this to describe the torque acting on an asymmetric object is difficult due to fact there is no simple approximation of the rotational stiffness. Vigilante *et al* [Vigilante2020] derived the upper limit of a dimer's MSAD along its long axis by assuming it was strongly trapped and so had limited angular motion, there expression gives:

$$\lim_{\tau \rightarrow \infty} \langle (\Delta u_z)^2 \rangle = 2 \left[ 1 - \frac{1}{4\beta\kappa_r} \left( \frac{\exp(\beta\kappa_r) - 1}{\exp(\beta\kappa_r) F(\sqrt{\beta\kappa_r})} \right)^2 \right] \quad (2.41)$$

Where,  $u_z$  is the unit vector connecting the two spheres of the dimer,  $\beta = 1/k_B T$ ,

## Chapter 2. Theory and methods

$\kappa_r$  is the rotational stiffness of the trap, and  $F$  is Dawson's integral [**Oldham2008**].

Vigilante's paper expressed that they couldn't compute  $MSD(\tau)$  because they couldn't solve the Einstein-Smoluchowski equation which describes the diffusion constant for dielectric particles. This would require a full description of a particle's electrical mobility and charge distribution - the latter could be achieved via a discrete dipole approximation, the former would be dependent on both the particle's position and relative orientation to the electric field.

### 2.5.4 Power Spectrum Density (PSD)

The power spectral density (PSD) method is by far the most versatile method for observing the dynamics of any object within an optical trap, allowing for fast calibration times while also quickly filtering out typical noise sources. Taking the Fourier transform of a particle's trajectory yields:

$$\hat{x}(f) = \frac{(2D)^{1/2}\hat{\eta}}{2\pi(f_c - if)} \quad (2.42)$$

where  $\hat{\eta}$  is the Fourier transform of the white noise, where the values are exponentially distributed as opposed to being normally distributed in the time domain [**BergSoerensen2004**], the correlation function is given as:

$$\langle \hat{\eta}_k \hat{\eta}_l^* \rangle = t_{msr} \delta_{k,l} \rightarrow \langle \eta^4 \rangle = 2t_{msr} \quad (2.43)$$

We can therefore ignore the white noise from our analysis by looking at the spectral

## Chapter 2. Theory and methods

density of  $\hat{x}(f)$ :

$$S_x = \frac{\hat{x}^2}{t_{msr}} = \frac{D}{2\pi(f_c^2 + f^2)} \quad (2.44)$$

Where  $t_{msr}$  is the period over which we collected data. The Lorentzian can be fitted via a simplified geometric series  $S_x = 1/(A + Bf_k^2)$  which allows us to compute both the diffusion coefficient (in arbitrary units) and the corner frequency  $f_c$  which is directly related to the trap strength via  $f_c = \kappa_x/(2\pi\gamma)$ . The Lorentzian shape implies that the trap is harmonic - but not symmetric - which assumes that the particle itself is an isotropic scatterer. Anisotropic scatterers will not produce a Lorentzian curve due to the coupled rotation and translation, though depending on the nature of that rotation (i.e. whether it is stochastic [**Bang2020**] or periodic [**Yogesha2012**]) will effect how drastically it departs from a typical Lorentzian curve.

Like with the analytical expression of the mean squared displacement we see two distinct regions, when  $f \ll f_c$  the PSD reaches a plateau value that when converted to length units represents the maximum displacement the particle can move beyond the focus, however when  $f \gg f_c$  the PSD falls off exponentially which denotes the particle is freely diffusing within the beam focus.

The Lorentzian relationship is only valid for frequency terms up to the Nyquist frequency (half of our sampling rate), this is because we are only taking a finite sampling of the particle's trajectory meaning the signal is aliased. Berg and Sorensen provide a

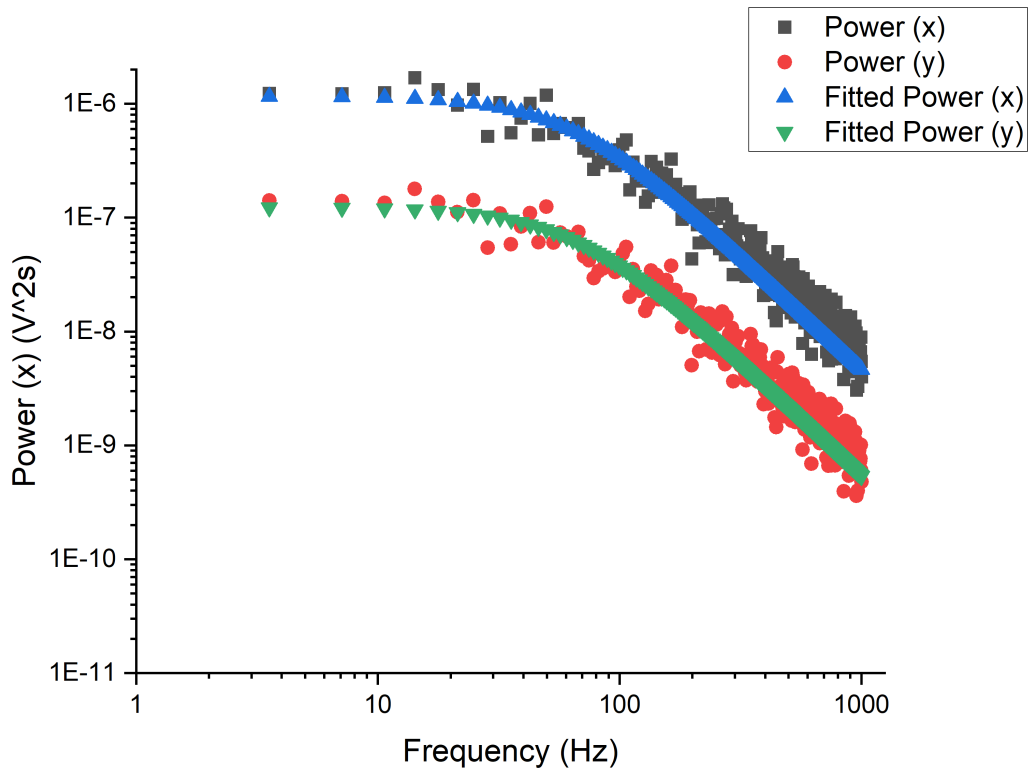


Figure 2.4: Example PSD fitted using (2.44), power spectra is collected from an optically trapped silica sphere suspended in water. The difference in magnitude is due to the asymmetry of the quadrant photo diode having a stronger signal response in the direction of the polarisation vector. Using a correction factor (see (??)) will adjust the power spectra to better describe the trap shape.

suitable modified Lorentzian to account for the aliasing effects [BergSoerensen2004]:

$$S_x = \frac{(\Delta x)^2 \Delta t}{1 + c^2 - 2c \cos 2\pi f_k \Delta t / N} \quad (2.45)$$

Where  $N$  is the total number of samples taken,  $\Delta x$  &  $c$  have no direct physical interpretation and are defined in [BergSoerensen2004]. Further modifications can be made to the power spectrum model but this is only useful when a high degree of accuracy is necessary. Typically power spectra are recorded using a Quadrant Photo

## Chapter 2. Theory and methods

Diode (QPD), which records motion in voltage units, not in units of length. There are two main methods for converting to physical units: If multiple photodetectors are available then a differential interference contrast (DIC) system can be used to compute the linear relationship between the beads displacement and the photodiodes signal [Capitanio2002]. While this is useful when high force precision is necessary it also allows you to collect information about the particle's motion along a single direction, making it ideal for less focused beams. Alternatively, if the size distribution is very wide but each particle can be accurately sized, then a conversion factor can be approximated by comparing the fitted value of the diffusion coefficient, and the reported value given by the Stokes-Einstein relation.

$$D_{SE} = \frac{k_B T}{\gamma_0} \Rightarrow \text{Conversion Factor } [m/V] = \sqrt{\frac{D_{SE}}{D_{fit}}} \quad (2.46)$$

With the latter method, the local fluid viscosity must be known to a high degree of accuracy, depending on the local heating effect this may be as trivial increase or it may be significant enough to drastically alter the characterisation. PSD analysis is often seen as the gold standard for calibration as it can be fine tuned to the point that optical forces can be computed on the order of  $10^{-15} N$  [BergSoerensen2004], it captures all of the information acquired by other calibration techniques while filtering out noise and requiring a relatively small amount of data collected.

#### 2.5.4.1 Power spectral analysis for rotating objects

The scattering from rotating objects can be partially characterised via the power spectrum density method. Typically papers reporting on the rotation rate of a trapped object will collect a power spectrum and look at the maximum frequency term to determine its rotation rate. However this often neglects any information on the trapping forces acting on particle and only looks at the torque applying around one of the particle's primary axis. There has only been one notable effort to fully characterise the full trapping dynamics on a rotating body, [Yogesha2012] developed a theoretical model for that relates the power spectrum to both the rotational and translational motion simultaneously.

## 2.6 Simulation of spherical aggregates

Later chapters cover the dynamics of spherical aggregates and anisotropic scatterers, these subjects are particularly difficult to characterise using conventional calibration techniques [Li2008, Yogesha2011PreciseCO]. As an example consider a symmetric dimer as a paradigmatic aggregate; if we consider the Langevin equation for such a aggregate within an optical trap we have:

$$\frac{d\vec{r}(t)}{dt} = \frac{\vec{\kappa}_x}{\gamma} \vec{r}(t) + \sqrt{2D_x} \eta(t) \quad (2.47)$$

Where  $x(t)$  is replaced with  $\vec{r}(t)$  to signify that the translational motion is generalised to a 3 dimensional case. Except now, the dimer is undergoing random rotational motion in addition to its Brownian translational motion the first term on the right hand

## Chapter 2. Theory and methods

side is no longer purely a function of the dimer's position but also on its orientation. The rotational form of the Langevin equation for a dipole within an external potential is given as:

$$\frac{d\vec{u}(t)}{dt} = \frac{\mu}{\gamma_R} [\vec{u}(t) \times \vec{E}(t)] \times \vec{u}(t) + \sqrt{2\vec{D}_R} \lambda(t) \times \vec{u}(t) \quad (2.48)$$

Where  $\vec{u}(t)$  is the unit vector aligned along the centres of the two spheres,  $\mu$  is its dipole moment, and  $\gamma_R$  is the rotational friction coefficient which is given as  $\gamma_R = 8\pi\eta r^3$  for a sphere, if the dimer is within a harmonic potential we can write the first term on the right hand side as  $\frac{\vec{\kappa}_u}{\gamma} \times \vec{u}(t)$ , where  $\vec{\kappa}_u$  is the rotational stiffness vector.  $\lambda(t)$  is the Brownian rotations from the surrounding fluid, like in the translational case the Brownian rotations are normally distributed and are also uncorrelated so that:

$$\langle \lambda(t)\lambda(t') \rangle = \delta_{ij}\delta(t-t') \quad (2.49)$$

For an asymmetric scatterer whose radius is comparable to that of the electric field's wavelength we now have a system of simultaneous equations:

$$\frac{d\vec{r}(t)}{dt} = \frac{\vec{\kappa}_x(\vec{u}(t))}{\gamma} \vec{r}(t) + \sqrt{2D} \eta(t) \quad (2.50)$$

$$\frac{d\vec{u}(t)}{dt} = \frac{\vec{\kappa}_u(\vec{r}(t))}{\gamma_R} \times \vec{u}(t) + \sqrt{2\vec{D}_R} \lambda(t) \times \vec{u}(t) \quad (2.51)$$

Fortunately, we do not need to solve these directly as the latter two random variables can be easily approximated if the thermal energy of the system is known, and the rate of change can be assumed as linear if we take a sufficiently small time step that

## Chapter 2. Theory and methods

$\Delta t \ll \kappa_x/\gamma$  &  $\Delta t \ll \kappa_u/\gamma_R$ . In doing so we now only need to compute the optical force and torque applied to the dimer.

Using a MATLAB package called *Optical Tweezer Toolbox* or *ott* [Niemenen2007] we can compute the beam shape coefficients ( $a_{nm}$  &  $b_{nm}$ ) for any desired beam type. Using the results from [Farsund1996] we can then compute both the optical force and torque using the beam coefficients and the scattering coefficients ( $q_{nm}$  &  $p_{nm}$ ) which are found by calculating the dimer's  $T$ -matrix via *mstm* [Mackowski2011] and then using (2.21). The form given by [Crichton2000THEMD] is an easier form to compute for higher orders of  $N_{max}$ :

$$\begin{aligned} \mathbf{F}_z = & -\frac{1}{4\pi k^2} \sum_{n,m} \left( \frac{m}{n(n+1)} \Im[a_{nm}b_{nm}^* - p_{nm}q_{nm}^*] \right. \\ & + \frac{1}{n+1} \left[ \frac{n(n+2)(n-m+1)(n+m+1)}{(2n+1)(2n+3)} \right]^{1/2} \\ & \left. \times \Im[b_{nm}b_{nm}^* + a_{nm}a_{n+1m}^* - q_{nm}q_{nm}^* + p_{nm}p_{n+1m}^*] \right) \end{aligned} \quad (2.52)$$

$$\begin{aligned} \mathbf{T}_z = & -\frac{1}{8\pi k^3} \sum_{n,m} \left( \frac{m}{n(n+1)} [|a_{nm}|^2 + |b_{nm}|^2 - |p_{nm}|^2 - |q_{nm}|^2] \right. \\ & + \frac{2}{n+1} \left[ \frac{n(n+2)(n-m+1)(n+m+1)}{(2n+1)(2n+3)} \right]^{1/2} \\ & \left. \times \Re[b_{nm}a_{nm}^* + a_{nm}b_{n+1m}^* - p_{nm}q_{nm}^* + q_{nm}p_{n+1m}^*] \right) \end{aligned} \quad (2.53)$$

where  $a_{nm}$ ,  $b_{nm}$ ,  $p_{nm}$ , and  $q_{nm}$  are the beam coefficients of the incident and scattered fields respectively. We can get the transverse force and torque components in a similar form by applying a simple rotation transformation. With the optical forces and torques computed all that remains is to compute the Brownian forces and torques which are

## Chapter 2. Theory and methods

constrained by the relation.

$$\langle q_i q_j \rangle = 2D_{ij}\Delta t \quad (2.54)$$

Vigilante et al compiled together a python package that combines both *ott* and *MSTM* to simulate the behaviour of spherical aggregates within a predefined optical trap [Vigilante2020].

### 2.6.1 Simulation parameters

Throughout this PhD we use the work of Vigilante to perform a systematic study of the dynamics demonstrated by asymmetric dimers in both plane and circularly polarised light. The simulations have two primary frames of reference that require explanation. Firstly, there is the laboratory frame which describes the coordinate system, we define the origin of our simulation as the focus of our trapping beam. While the choice in direction for the  $x$  and  $y$  axis are arbitrary the  $z$  axis is specifically chosen so that it is aligned with the direction of beam propagation.

Secondly there is the particle frame which describes the orientation state of the particle, orientations are reported as quaternions which can be readily transformed into rotation matrices. The matrix describes the direction of the particles 3 orientation axis  $U_x$ ,  $U_y$ , and  $U_z$ ; the latter is oriented so that it is collinear with the centres of the two spheres. The origin of the 3 axis' is set on the particle's centre of mass, this is also used to define it's displacement from the origin of the laboratory frame.

Furthermore we expand upon their work to create a fully functional quadrant photo-

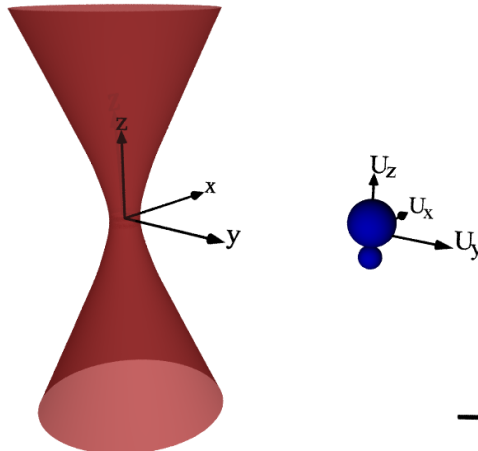


Figure 2.5: Ray scattering render of both the laboratory frame and particle frame for a dimer and a Gaussian beam. The origin of the laboratory frame is defined as the focus of the trapping beam, with the positive  $z$ -axis being aligned with the direction of beam propagation. The particle frame is centered on the dimer's centre of mass with the primary axis  $U_z$  being aligned with the centres of the two spheres. Black line is scaled to represent  $1 \mu m$ .

diode to simulate the response from a calibration test. This builds upon the work from [Rohrbach2002] which applied the fundamental principles of Lorenz-Mie theory to replicate the response signal of a QPD being used in back focal-plane interferometry.

## 2.7 Simulated Quadrant Photodiode

In order to simulate a typical experimental set up with a QPD installed as a position detection system we need to evaluate the total magnitude of the electric field incident on the photo-diode surface. While trapping a micro-particle, the scattered and incident fields combine together and interfere with one another. These fields are collected by a condenser lens in the far field limit and are focused onto the QPD surface, the total

## Chapter 2. Theory and methods

intensity can be evaluated as:

$$I(x, y) = \epsilon_0 c \left| \begin{bmatrix} E_{i,x}(x, y) + E_{s,x}(x, y) \\ E_{i,y}(x, y) + E_{s,y}(x, y) \\ E_{i,z}(x, y) + E_{s,z}(x, y) \end{bmatrix} \right|^2 \times \text{step}(NA_c - \sqrt{x^2 + y^2}) \quad (2.55)$$

The last term is simply a representative step term that defines the outer limit by which we evaluate the electric field, this is analogous to our condenser lens removing noise from other light sources by only accepting light at a specific acceptance angle defined by its numerical aperture  $NA_c$ . Depending on the relative size of our particle we can adjust the acceptance angle, this has very little effect on the transverse signals, but for axial evaluations of a trapped particle the numerical aperture should be tuned so that the resultant response curve has negative slope in order to allow for axial position detection, the method for finding this angle  $\theta_\Theta$  is discussed in [Friedrich2012].

The incident beam is simple enough to define given our set up parameters, for the sake of simplicity we assume that our beam is a Laguerre-Gaussian beam of mode  $[0.0, 0.0]$  (which is simply a pure Gaussian beam). *Ott* uses a point matching approach to approximate the beam shape coefficients of the incident field by fitting it to the far field estimate, the beam is of the form:

$$E_{\text{inc}}(kr) = \sum_n^{\infty} \sum_{m=-n}^n a_{mn} RgM_{nm}(kr) + b_{nm} RgN_{nm}(kr) \quad (2.56)$$

where  $RgM_{nm}(kr)$  &  $RgN_{nm}(kr)$  are regular vector spherical wave functions, these differ from (2.11) in the fact that the field can either be expressed as an incom-

## Chapter 2. Theory and methods

ing/outgoing wave (with a singularity at the origin) or as a regular wave around the origin; for incoming/outgoing waves the wave functions use the first/second forms of the Hankel function respectfully. In order to compute the regular spherical wave at the origin we replace the Hankel function with the Bessel function which is simply the average of the first and second forms of the Hankel function, so at the origin we avoid a singularity of the EM field.

We can if we want further restrict the incident beam by setting the truncation angle to match our microscope object, this applies a hard cut off to the incident beam to better represent experimental conditions. In order to compute the scattering from the target particle *ott* uses the *T*-matrix method, this is not essential for a simple sphere but is essential for complex shaped particles such as dimers. The matrix from *mstm* needs to be repackaged to work with the *ott* software, converting it from a column vector into a system of sub matrices.

The scattered and incident fields are then combined together in the far field to get  $I(x, y)$ , the quadrant and overall signals are calculated via:

$$Q_i = \sum_{n,m} I(x_{i,n}, y_{i,m}) \quad (2.57)$$

$$S_x = \frac{(Q_1 + Q_2) - (Q_3 + Q_4)}{\sum I_0(x, y)} \quad (2.58)$$

$$S_y = \frac{(Q_1 + Q_3) - (Q_2 + Q_4)}{\sum I_0(x, y)} \quad (2.59)$$

$$S_z = \frac{(Q_1 + Q_2 + Q_3 + Q_4)}{\sum I_0(x, y)} \quad (2.60)$$

Where the denominator is the total intensity on the QPD while there is no particle

## Chapter 2. Theory and methods

within the trap. The QPD sensitivity is dependent on both the polarisation of the incident beam and the displacement of the target sphere, this is shown in fig. 2.6.

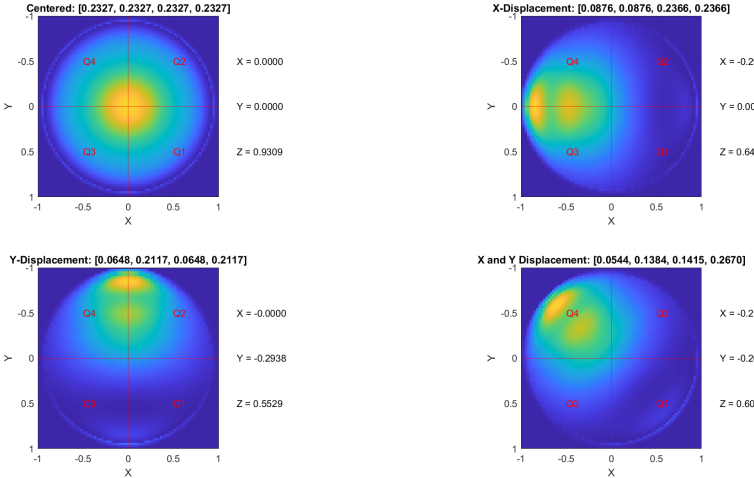


Figure 2.6: Total Field incident on the quadrant photo diode for several different displacements. Top Left:  $2\mu m$  diameter silica sphere placed at the focus of a beam. Top Right: silica sphere is now displaced by  $1\mu m$  along the x-axis. Bottom Right: silica sphere is now displaced by  $1\mu m$  along the y-axis. Bottom Left: silica sphere is now displaced by  $0.707\mu m$  along the x and y axis. The trapping beam is a  $TEM_{00}$  Gaussian, polarised along the x-axis.  $S_x$ ,  $S_y$ , and  $S_z$  are shown to the right of each graph,  $Q_1$ ,  $Q_2$ ,  $Q_3$ , and  $Q_4$  are shown above each graph.

While translational motion have no knock on effects to the QPD signal, rotational changes are between the incident and total fields. This results in rotational motion being biased in the QPD signal - even when collecting signals from isotropic scatterers. To remedy this an inverse rotation is applied to the total field.

To confirm that our method is producing accurate results, we ran a comparison between our simulative QPD and the results from [**Rohrbach2002**]. Where a  $300\text{ nm}$  diameter sphere is scanned across the path of a focused Gaussian beam ( $\lambda = 1064\text{ nm}$ ,  $NA = 1.2$ ), the sphere has a refractive index of 1.57 and is suspended in water

## Chapter 2. Theory and methods

( $n_{med} = 1.33$ ) and the condenser lens has its numerical aperture set to 0.5 ( $\theta_{max} = 30^\circ$ ).

Scanning across all three primary axis produced the following response curve:

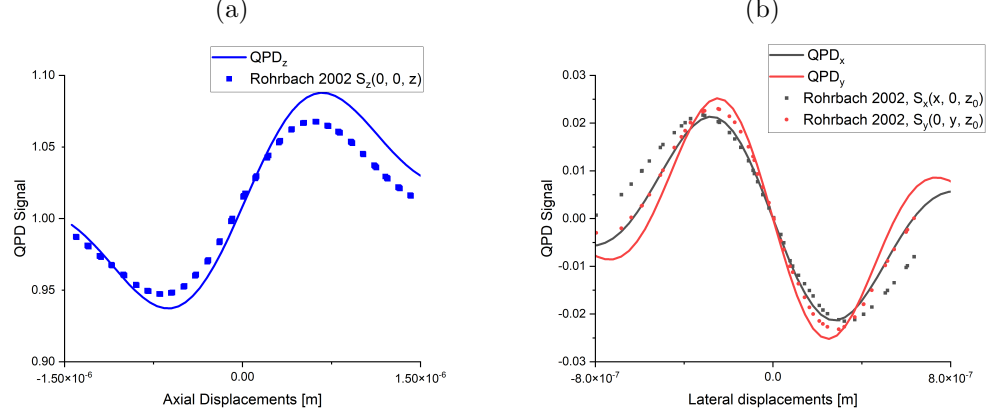


Figure 2.7: Comparison between QPD response signal versus work conducted by Rohrbach, single sphere ( $r = 150\text{ nm}$ ,  $n = 1.57$ ) is scanned by a  $1064\text{ nm}$  laser and the QPD signal recorded. Solid lines represent the signal produced by QPD using *ott* and points represent the signal response collected from **[Rohrbach2002]**.

The discrepancy between our simulated QPD and the results from Rohrbach can be attributed to the fact that the QPD signal With this any trajectory can be collected from the QPD by displacing and rotating the beam accordingly, later in chapters 4 and 5 we discuss how to extract information from the QPD's signal.

# Chapter 3

## Effects of localised shearing on crystal growth and nucleation

As outlined in Chapter 1, the original outline of the project is to investigate the possibility of using optical tweezing to induce nucleation by generating fluid flow within a supersaturated solution. The intent of which would be twofold: Firstly to have a repeatable means of inducing nucleation under different solution conditions. And secondly, to understand the influence of shearing on nucleation at a micro level as compared to results in bulk fluid. It has been shown that for macro-scale systems, the likelihood of nucleation increases to a maximum value under increased shearing [Debuysschere2023, Mura2016]. Mura and Zaccione developed a theoretical framework to describe how the a newly formed nucleus experiences two additional growth factors when placed in a moving fluid. Firstly, due to increased molecular transport of solute molecules the nucleation rate is enhanced in low to moderate fluid flows. But in addition, due to shear flow the crystal surface undergoes deformation which suppresses

the nucleation rate undergoing faster fluid flow [**Mura2016**]. The theory was confirmed for glycine solution by Debuyschere *et al* who identified that the nucleation rate of supersaturated glycine was enhanced up until  $\dot{\gamma} \approx 3000 \text{ s}^{-1}$  [**Debuyschere2023**]. After which the nucleation rate began to decrease but was still greater compared to the case where fluid flow was minimal.

Optical tweezers can been used to rotate a whole host of micro-rotors, with the fastest reported results exceeding 1000  $\text{Hz}$  in heavy water [**Arita2016**]. Therefore, it stands to reason that a micro-rotor rotating in a supersaturated solution could generate sufficient fluid flow such that the nucleation rate around said particle is enhanced compared to the bulk fluid. We focused on two primary candidates for micro-rotors, Vaterite and 4-Heptyl-4-biphenylcarbonitrile (7CB). The former being a polymorph of calcium carbonate and the latter an example of nematic liquid crystals, both of which have been used repeatedly in previous micro-rotor. In addition, we also consider the application of using techniques beam steering to generate fluid flow by trapping silica micro-beads. In this instance the fluid flow is generated not due to the transfer of angular momentum, but due to shearing caused by a moving sphere through stagnant fluid.

To begin with, the discussion of the necessary optical equipment is covered, drawing attention to specialised components and techniques that are not standard in optical trapping set ups.

### 3.1 Optical Tweezer Equipment

In general, all optical tweezers require a laser driver, a focusing microscope objectives, a position controller, and position detector. The laser used for this project was a  $1064\text{ nm}$  near infrared laser - provided by CNI Lasers – that was focused by a Nikon 100x oil immersion lens. The choice of an oil immersion lens is important as the optical oil used prevents a loss of focus when used on a glass cover slip. Now, experimental work has shown that the trapping efficiency increases with beam diameter up until it exceeds  $\frac{2}{3}D_{obj}$  [kim2003dependence] where  $D_{obj}$  is the diameter of the objective aperture. To expand the beam front we utilise a Galilean beam expansion arrangement (indicated by  $f_1$ , and  $f_2$  in Fig. 3.1) as recommended for high power laser applications. In our initial experiments the beam expansion provides a  $4\times$  magnification. Whereas in later experiments we utilised a galvano-mirror the beam expansion is  $3\times$  and then the 4f correlator provides a further  $1.25\times$  magnification (using  $f_3$  and  $f_4$ ) - the magnification is given by.

$$\frac{D_2}{D_1} = \frac{f_2}{f_1} \quad (3.1)$$

It should be noted that the galvano-mirror requires the use of a Keplerian beam expansion arrangement which reduces the transmitted laser power due to localised heating of the air. Afterwards the laser is passed through a dichroic mirror that separates incoming infrared and visible light, this is to prevent the laser from damaging the CCD camera used for imaging the trapping plane. The laser is then focused to a diffraction limited spot by the objective. Utilizing a high numerical aperture objective enhances

the gradient force at the focal point; the trade-off being that the for higher NA objectives the trapping depth is reduced due to spherical aberrations. While it is possible to increase the trapping depth [Reihani2006] by adjusting the objective's tube length this approach is incompatible with our trapping arrangement. A 0.25 NA condenser objective refocuses the scattered laser light and also provide an aperture for an imaging LED to illuminate the focal plane. Samples are loaded onto a piezo driven table to that is inserted between the trapping and condensing objectives; the piezo drivers allow for sub-micron control of the beam focus position to a degree as small as a 10 nm. To detect and monitor the position of a trapped particle a quadrant photo diode (QPD) was utilised.

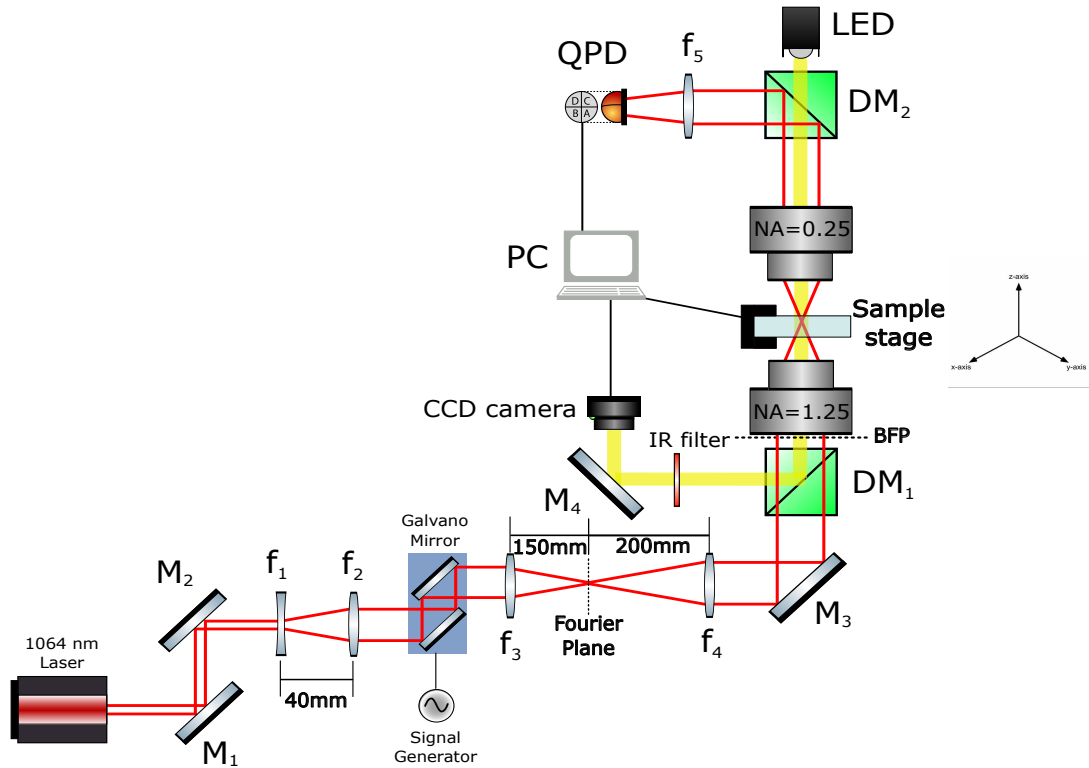


Figure 3.1: Optical tweezer set up used for the majority of the PhD. The focal lengths of  $f_1$ ,  $f_2$ ,  $f_3$ , &  $f_4$  are  $-20\text{ mm}$ ,  $60\text{ mm}$ ,  $150\text{ mm}$ , &  $200\text{ mm}$  respectively. Diagram not drawn to scale.

### 3.1.1 Position detection methods

In order to accurately capture the dynamics of a trapped particle, a position detection system is required. There are 3 possible methods of position detection: video-analysis, lateral-effect position sensing, and photodiodes. The former being ideally suited for multiple traps or situations where precision is not the top priority. In order to match the force measurements of back-focal plane interferometry requires the camera's frame rate to exceed 1  $kH\bar{z}$  which can be difficult to achieve while maintaining a decent resolution [Gibson2008]. In comparison off the shelf back-focal plane detectors can achieve temporal resolutions anywhere from 10 – 100  $kH\bar{z}$  [BergSoerensen2004].

A quadrant photo diode (QPD) is a frequently used position detection system for optical tweezers due to their high sampling rate, high degree of precision, and ease of set up. The QPD is constructed of four photo diodes assembled in a quadrant formation, when a particle is trapped the interference pattern produced is focused onto the QPD, with the maximum intensity mapping to the particle's centre of mass. By summing the voltages of the horizontal and vertical quadrants together the particle's centre of mass is tracked in the x-y plane. Axial displacement can be estimated by observing the change in the total voltage of the QPD. The outputted signal gives an indication of the particle's relative displacement from the beam focus, but in order to convert the signal to distance units the trap needs to be calibrated (assuming a linear response curve).

A lateral-effect sensor has a similar output but works using a the entire sensor as a single cell analogous to the focal plane of the trapping beam. The four corners of the sensor act as anodes connected to a base plate cathode, as the beam moves across the

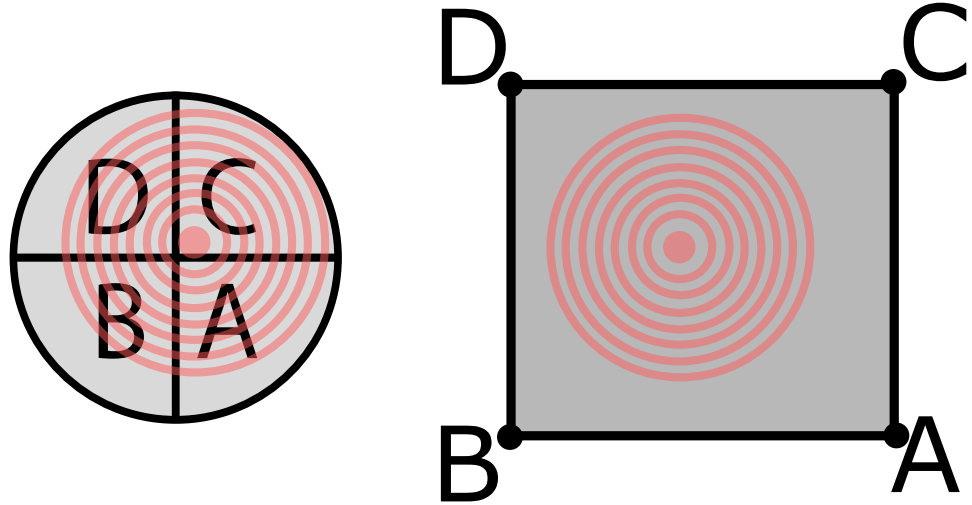


Figure 3.2: Comparison between QPD and Lateral effect photodiodes. The four quadrants of a QPD (left) experience different photocurrents based on the total intensity of light incident on each section (labelled A, B, C, D). Whereas a Lateral effect sensor (right) uses the resistive properties of the photodiode surface to create different photocurrents passing through the anodes A, B, C, and D.

surface of the detector each anode will experience a different photocurrent depending on how close the centre of the interference pattern is to each anode. The advantage of a lateral effect detector is that the linear regime is much larger than a QPD making it much better for monitoring the position of a trapped particle. However, Lateral-effect sensors are often limited in their spacial resolution due to high signal-to-noise ratios, requiring a high intensity of light on the sensor in order to get a clean signal. As a result, most optical force measurements are conducted using a QPD as opposed to a lateral-effect sensor, as often the displacement is small enough that the signal-displacement

curve can be considered linear.

### 3.1.2 Fourier Optics and 4f correlators

A 4f correlator is an example of Fourier optics in practice, understanding that a focused lens takes a Fourier transform of the light profile. Consider a laser with a circular Gaussian profile, if you were to place a detector there you would pick up the intensity as a function of its position within the beam. If however you focused the light into a single point (using a +ve focal lens) you are actually seeing a measurement of the phase of your laser with position, in which you would see a diffraction limited spot ( $d = \lambda/2nsin(\theta)$ ), indicating that the laser is collimated. In imaging systems, a series of focal lenses can be used to filter out unwanted scattering from an image (or in an inverse case differentiate between different images), the placement of each lens is shown below.

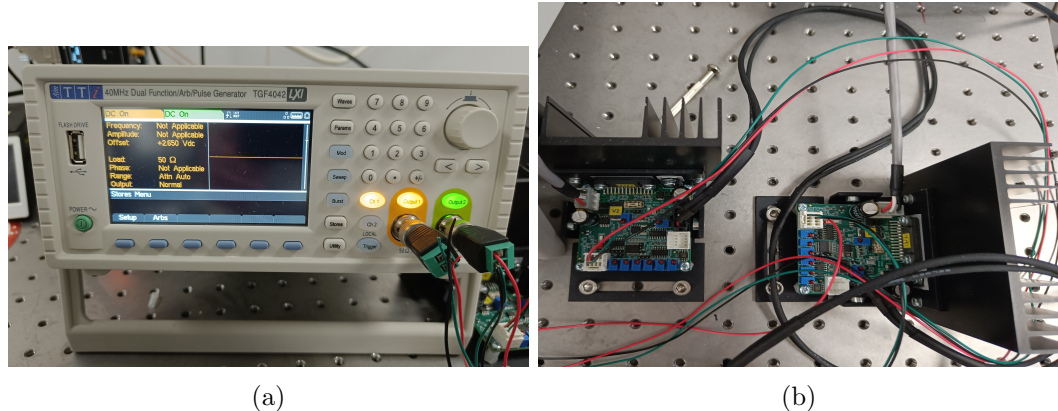


Figure 3.3: Signal generator galvano mirror controller, channel 1 controls the x-axis mirror, while channel 2 controls the y-axis mirror. Both channels can be manipulated independently.

For our applications a 4f correlator is utilised to ensure that the motion of the galvano-mirrors does not move the focal point of the laser, allowing for a stable trap

even while in motion. As shown in Fig. 3.1, after the galvano-mirror we have our two lenses -  $f_3$  and  $f_4$  - the former being installed 150  $mm$  from the second mirror of the galvano, and the latter being installed 200  $mm$  from the back focal plane of the trapping objective. The signal generator used was supplied by 'MCS Test Equipment Ltd', allowing for dual channel signal control. This allowed us to precisely control the alignment, amplitude, phase, and frequency of both mirrors making alignment much easier. For basic trapping calibration the galvano-mirrors were set to a simple DC output, providing a fixed spot which operates like a typical optical trap.

## 3.2 Synthesis of Birefringent Micro spheres

There are several options for particles that can be rotated using optical tweezers [Parkin2009, Saito2022]. Over the course of the project two different micro spheres where investigated, Vaterite and liquid crystal droplets. Both can be readily synthesised in the lab and are will rotate at a variety of sizes.

Vaterite is a polymorph of calcium carbonate that is rarely seen in nature due to its low stability [KonopackaLyskawa2019]. However unlike its other polymorphs of calcite and aragonite, when synthesised Vaterite will typically form small spherical particles making them ideal for optical trapping and rotation. Synthesis of Vaterite micro spheres requires fine control of the crystal growth process in order to maintain polymorphic stability. Though for the purposes of optical rotation the exact polymorph is not as important as its morphology as all 3 polymorphs are inherently birefringent.

Vaterite samples where made by the first preparing equal amounts of  $CaCl_2$  and

$Na_2CO_3$  at a concentration of  $0.33M$ , at the same time a vial of  $0.33M$   $MgSO_4$  was prepared and set aside for later. First a small vial was filled with  $1.5mL$  of  $CaCl_2$  followed by  $60\mu L$  and  $90\mu L$  of  $MgSO_4$  and  $NaCO_3$  respectively, forming a seed solution. Next, a larger vial was filled with  $5\text{ mL}$ ,  $1.5\text{ mL}$ , and  $1\text{ mL}$  of  $CaCL_2$ ,  $MgSO_4$ , and  $NaCO_3$  respectively followed by the seed solution. After 10 minutes of slow but continuous mixing a few drops of Agepon was added to halt the reaction, the solution was filtered and washed 3 times with distilled water before being suspended in water.

When trapped in circularly polarised light, the anisotropic crystal lattice allows spin angular momentum to be transferred to the Vaterite particle, resulting in a rotation about the beam axis. In addition, the anisotropic scattering causes the QPD signal to vary with a constant periodicity that is attributed to its rotation rate. Therefore, the resulting power spectrum is not a Lorentzian but now also displays peaks that appear at integer multiples of the particles rotational frequency.

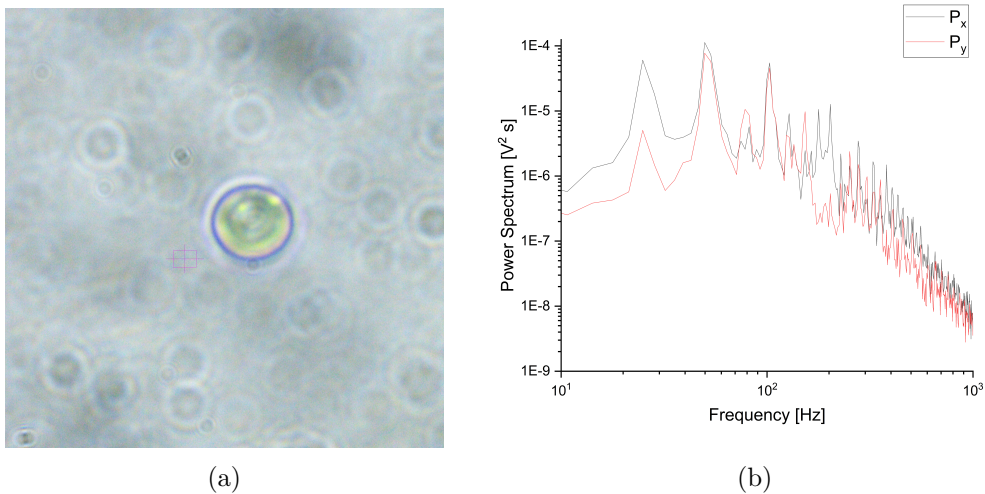


Figure 3.4: (a) Sample Vaterite sphere suspended in water and trapped by circular polarised trap. (b) Collected power spectrum from rotating Vaterite, peaks in the power spectrum appear at integer multiples of the rotational frequency ( $f_{rot} \approx 49.8$  Hz)

As shown by Fig. 3.4(b) the power spectra produced still demonstrates a Lorentzian curve but modified with these periodic peaks, while the Lorentzian can be loosely fitted to the end tail there exists no current model for describing the power spectra. The closest approximation to this was conducted by [Yogesha2012] where they describe the rotational motion of ellipsoidal polystyrene particles. The critical assumption being that the particle perfectly rotates in the  $x - y$  plane. It has long been suspected that birefringent microspheres experience torques outside of the  $x - y$  plane [Volpe2023] making it very difficult to characterise the behaviour of rotating birefringent microspheres without a proper understanding of the full optical torque being applied to it.

### 3.2.1 Liquid Crystal Rotors

Liquid crystals are an intriguing example of materials with mixed phase properties. Unlike typical solutes such as Glycine, a liquid crystal can still maintain some degree of order between its individual molecules while in the liquid state. This is due to the fact that liquid crystals are constructed of ordered molecules that demonstrate a long range ordering. There are three main types of liquid crystal transition methods: Thermotropic crystals will transition to their liquid crystal phase when sufficiently heated. Lyotropic materials can undergo this transition due to changes in temperature and concentration. And lastly, Metallotropic materials - which are composed of both organic and inorganic molecules - change phase according to the ratio of organic to inorganic molecules present. Liquid crystal rotors are rather simple in their production, 4-Heptyl-4-biphenylcarbonitrile (7CB) was purchased from Sigma Aldrich and a small amount was added to a vial of distilled water. The solution was then heated in a

water bath to 25° in order to transition the solid crystal into its liquid crystal state. The solution can then be loaded onto a sample cover slip and the individual droplets visualised. The molecules of 7CB will align with a strong electric field, and due to the spherical droplet geometry the droplets are inherently birefringent.

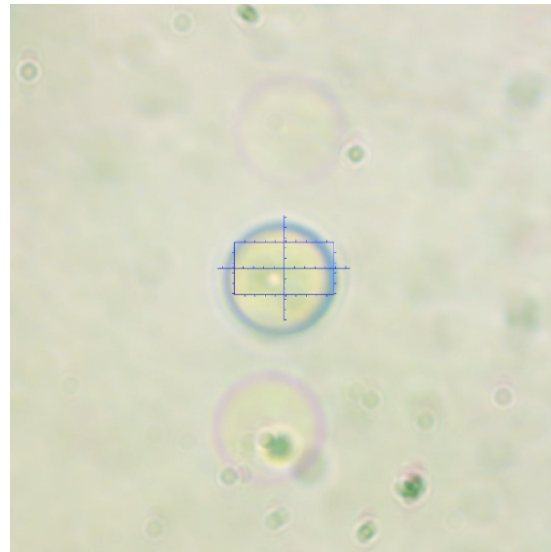


Figure 3.5: Liquid crystal undergoing rotation due to the circularly polarised trap.

The liquid crystal droplets had a much faster rotation rate than comparable Vaterite spheres, due to their higher degree of birefringence and the fact that the droplets are far closer to perfect spheres making angular momentum transfer more efficient.

### 3.3 Rotation of birefringent micro spheres

Optical tweezing has often been used for micro-rheology, by computing the exact forces being exerted on the trapped sphere, one can determine the local temperature/viscosity of the medium [Millen2014, RodriguezSevilla2018]. Using a birefringent particle and rotating it within the fluid, the maximum rotation rate is due to the fluid drag

resisting the torque of the trapping beam [**RodriguezSevilla2018**]. If you want to measure fluid flow you can instead use a micro-rotor to see how fluid flow propagates in the medium [**Knoener2005**]. Likewise, one can use a beam steering arrangement to probe the drag force of the fluid, by understanding the trap strength (calibrating using a low frequency signal) one can measure the drag force experienced by the local fluid [**RobertsonAnderson2018**]. I

Understanding the fluid velocity around our trapped object is determined mostly by the Reynold's number of the system, for a sphere submersed in a moving fluid of velocity  $U$  this is given by:

$$Re = \frac{\rho U D}{\mu} \quad (3.2)$$

Where  $D$  is the sphere's diameter, and  $\rho$  and  $\mu$  are the fluid's density and viscosity respectively. In our case we do not have a fluid moving around a sphere but a sphere moving through the fluid at some velocity  $U$ , assuming a no-slip boundary condition we can model the fluid velocity profile based on the velocity of the particle. There are two possible avenues for generating shear flow with a trapped particle; rotation of birefringent particles, and fluid flow induced by particle motion.

Rotating birefringent particles are by far the most common method for generating and measuring fluid flow in a solution. To see if we can even achieve the theoretical maximum shear rate, Vaterite spheres were synthesised (see Sec.3.2) submerged in water and trapped with the 1064 nm laser at set to 450 mW. The rotation frequency was determined using the QPD, and the particle sizes were computed by image analysis.

With the particle size and rotation frequency, the tangential rotation speed is calculated via:

$$u(r) = \frac{\pi}{4} \frac{d^3}{r^2} \omega \quad (3.3)$$

Where  $d$  is the particle diameter,  $\omega$  is the rotation frequency reported by the QPD, and  $r$  is the distance from the particle's centre. Using Eq.3.3 we calculated the fluid flow radiating outward from the centre of the sphere. The shear rate can then be computed as the partial derivative fluid flow (assuming shearing is generated purely by the flow field):

$$\dot{\gamma}(r) = \left| \frac{\delta u(r)}{\delta r} \right| = \frac{\pi}{2} \frac{d^3}{r^3} \omega \quad (3.4)$$

### 3.3.1 Estimation of fluid flow around micro-rotors in bulk fluid

First we determined the upper rotation rate that could be achieved using both Vaterite and liquid crystal spheres. Vaterite samples were synthesised according to [**Parkin2009, Bishop2004**] (see sec. 3.2), and then suspended in distilled water. A sample of  $200 \mu L$  was pipetted and a single microsphere was captured via a circular polarised beam.

Due to Van der Waal's forces some of the microspheres were stuck together, fortunately individual sphere's were still present. Multiple microspheres were trapped and their rotation rate was determined by looking at the peak frequency component of the collected power spectrum. The shear flow was estimated using eq.(3.4) assuming the spheres were operating in the bulk fluid and away from any boundaries.

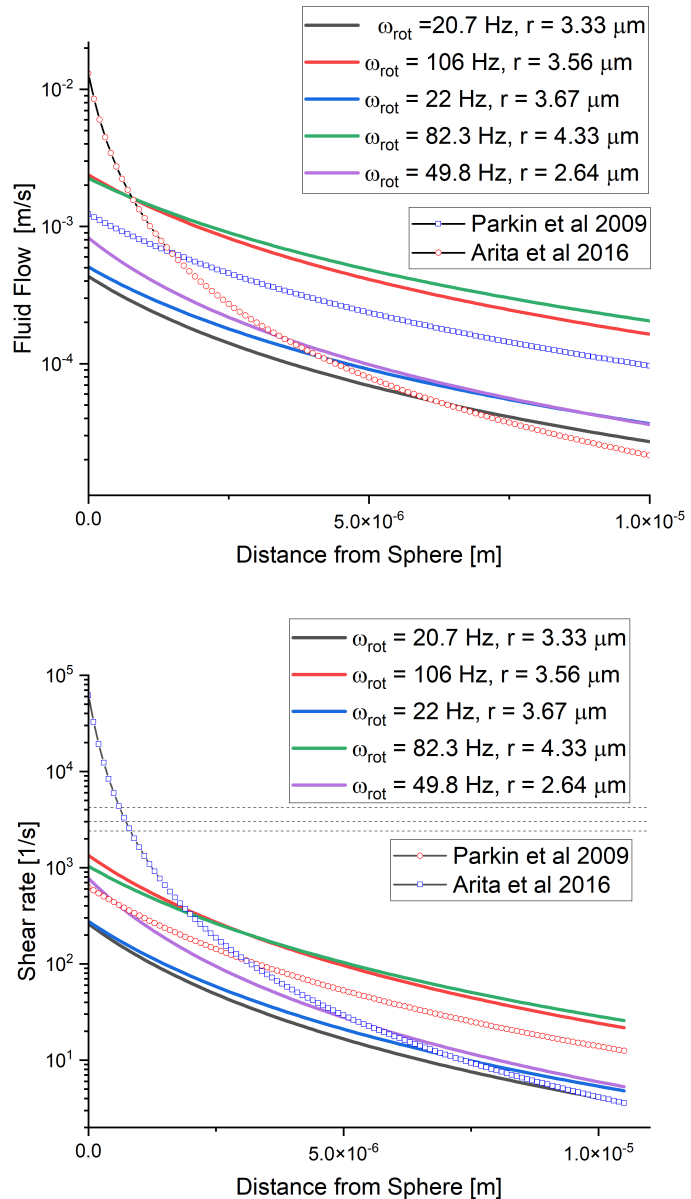


Figure 3.6: (Top) Fluid flow radiating out from the surface of a rotating Vaterite sphere. (Bottom) Shear rates computed using Eq.3.4, optimal shear rate is of  $3000 \text{ s}^{-1}$  is indicated by the dotted line. Vaterite radii and rotation frequencies are shown, the laser power was kept constant at 450 mW. Reported rotation rates, and their corresponding fluid flow and shear rates, for Vaterite are also plotted alongside lab results. Results from [Parkin2009, Arita2016] are included as well.

From Fig.3.6 there is not a strong relationship between particle size and rotation rate, this is contrary to much of the theoretical predictions that predict an exponential decay with particle size. This can be in part due to the fact that synthesising perfectly spherical spheres that have uniform birefringence across the whole population is difficult. Despite our best efforts at controlling the growth rate the smallest particle ever synthesised was around  $3 \mu m$  in diameter. The Vaterite spheres would often stick together while suspended in water after a short period of time. The fastest reported rotation rate found during this project was by [Arita2016] that achieved a rotation rate of  $5 kHz$ , this is plotted on Fig 3.6 as the dotted line. Even at that extreme a rotation rate the region in which nucleation is at its optimal likelihood is only  $20 nm$  wide. If instead the micro-rotor was within the vicinity of a solid boundary, the shear rate would be enhanced due to the no-slip boundary condition.

### 3.4 Micro-rotors in Supersaturated solution

If rotation rates in bulk solution are insufficient then a micro-rotor rotating close to an artificial barrier may be able to improve the shear rate of the surrounding fluid. Of course placing a solid barrier in a supersaturated fluid may well encourage nucleation somewhere on the surface outside of our control. Instead we chose to use the droplet edge of the supersaturated solution, while not a hard barrier per say, the molecular mobility close to the droplet edge is reduced due to surface tension. Furthermore, it has been shown through multiple results that nucleation is enhanced at the air-solution interface [Liao2022, Yuyama2010, Sugiyama2009].

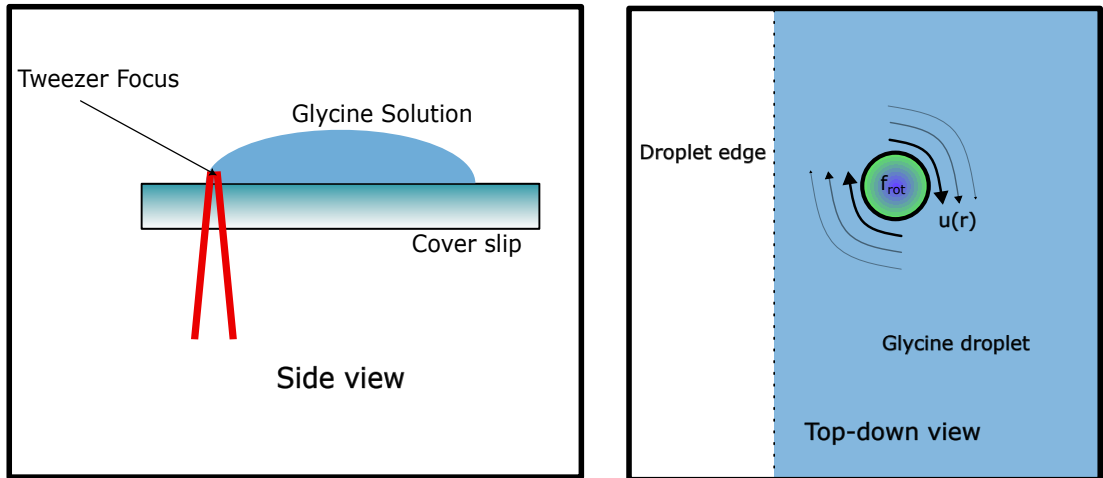


Figure 3.7: Diagram of optical trapping set up for rotating birefringent particles in a supersaturated solution. Left: side view of the trapping set up showing the location of the trap focus at the edge of the droplet of a supersaturated solution. Right: top down view of the glycine droplet with a trapped birefringent particle shown close to edge of the trap. As the particle rotates the drag force from the surrounding fluid generates a flow field around itself (see Eq. 3.3).

Supersaturated solutions of glycine and water were prepared and stored in an incubator prior to use. When ready to be studied 15  $\mu L$  was pipetted into the solution and 20  $\mu L$  was pipetted onto the cover slip. A Vaterite sphere was located, trapped, and moved as close to the droplet edge as possible. After measuring the microsphere's rotational frequency the sphere was left to rotate for a period of ten minutes after which, if no nucleation event was observed the particle was released. The overall results are catalogued in table 3.1

Trying to trap a particle close to the edge proved more challenging than expected. Unlike in previous reports where the beam is focused at the upper edge of the droplet [Liao2022, Yuyama2010, Sugiyama2022], we attempted trapping into the crook of the droplet. It is suspected that trapping is much harder at the interface due to increased surface tension and unpredictable scattering forces. The closest we could

Table 3.1: Results from rotating Vaterite within supersaturated solution of  $H_2O$  and Glycine. Solubility concentration for Glycine at  $16^\circ$  was  $C^* = 0.2016g/g$ 

Super Saturation	Particle radius [ $\mu m$ ]	$\omega$ [Hz]	Nucleation [✓/✗]
1.01	2.34	10.4	✗
	5.67	9.63	✗
	3.26	8.46	✗
1.14	1.89	1.23	✗
	3.75	3.54	✗
	4.35	4.86	✗
1.4	3.47	0.00	✗
	1.59	0.00	✗
	6.24	0.00	✗
1.45	6.32	0.00	✗
	3.68	0.00	✗
	5.43	0.00	✗
1.49	4.76	0.00	✗
	7.27	0.00	✗
	1.52	0.00	✗

trap a microsphere to the droplet edge was in the range of  $5 - 10\mu m$ , at that distance the fluid flow is so low that even the presence of a hard boundary would be insufficient for shearing the fluid. Furthermore, as is evident in Table 3.1, the rotation rate drops off significantly with increased supersaturation, due to higher fluid viscosities. While in theory a sufficiently focused laser could rotate any microsphere to a fast enough to reach the shear rate predicted by [Debuyschere2023] the localised intensity would be so large that even using  $D_2O$  would see a significant increase in temperature.

It is not impossible that fluid shearing could be used in the future to localise nucleation; but from these results, using individual micro-rotors is not an appropriate method. Firstly, the area of influence is far too small to see any noticeable increase in the nucleation rate. And secondly, increased fluid viscosity significantly reduces the limits the maximum rotation rate possible. If multiple micro-rotors could be trapped in close proximity to one another they could create a large region of fluid where nucle-

ation is more likely than the bulk fluid. Micro-rotors have been created that allow for precise control of suspended micro-particles [Butaite2019] and could potentially be used to generate sufficient shearing. However these could not be used in this project as we lacked the necessary hardware to form multiple gradient traps.

### 3.5 Shearing via Galvano-mirror manipulation

An alternative approach to generating fluid shear is to use a galvano-mirror to rapidly move a trapped particle in a bulk fluid. While typically galvano and gimble mirrors are used to trap multiple particles simultaneously, a single micro sphere can be moved quickly through a fluid along a preset path. The only limitation on the particle's speed being the ratio of the trap stiffness to the drag force. Calculating the shear rate around an individual particle is difficult to do precisely but for low Reynolds numbers we can get an adequate approximation.

For a simple circular path one can estimate the sphere's speed by the radius of its path and the frequency of its orbit  $U = R\omega$ ; however for a more complex path, such as an elliptical orbit the curve needs to be parametrised. One can describe the position parameter of a circular path as such:

$$r(u) = [rcos(2\pi u), rsin(2\pi u), 0] \quad (3.5)$$

If we say that  $u$  describes time from some initial point we can say  $u = t\omega$  where omega is the frequency of orbit. Substituting this in and then taking the partial deriva-

tive of position gives:

$$v(t) = \frac{dr(t)}{dt} = [-2\pi r\omega \sin(2\pi t\omega), 2\pi r\omega \cos(2\pi t\omega), 0] \quad (3.6)$$

In order to compute  $\mathbf{U}$  we simply take the magnitude of our velocity. For low velocities the fluid flow at the sphere's surface can be computed based on its velocity.

$$u_r(r) = -|v(t)|^2 \left(1 - \frac{3R}{2r} + \frac{R^3}{2r^3}\right) \quad (3.7)$$

Where  $r$  is the radial distance to that point. Again taking the partial derivative we can get the shear rate for a particle moving through the fluid:

$$\dot{\gamma}(r) = \left| \frac{\delta u_r(r)}{\delta r} \right| = |v(t)|^2 \left( \frac{3R}{r^2} - \frac{2R^3}{r^4} \right) \quad (3.8)$$

Moving a silica bead along an circular path can generate significant fluid flow around a larger volume compared to comparable micro-rotors. Using (3.8) we estimated the shear rate that the surrounding fluid would experience at varying speeds. The maximum speed of  $7000 \mu ms^{-1}$  equates to moving the silica bead around a circular path with a frequency of  $100 Hz$ .

From figure 3.8 it is clear that not only is a galvano mirror a better option for generating high shear rates but also over a larger volume.

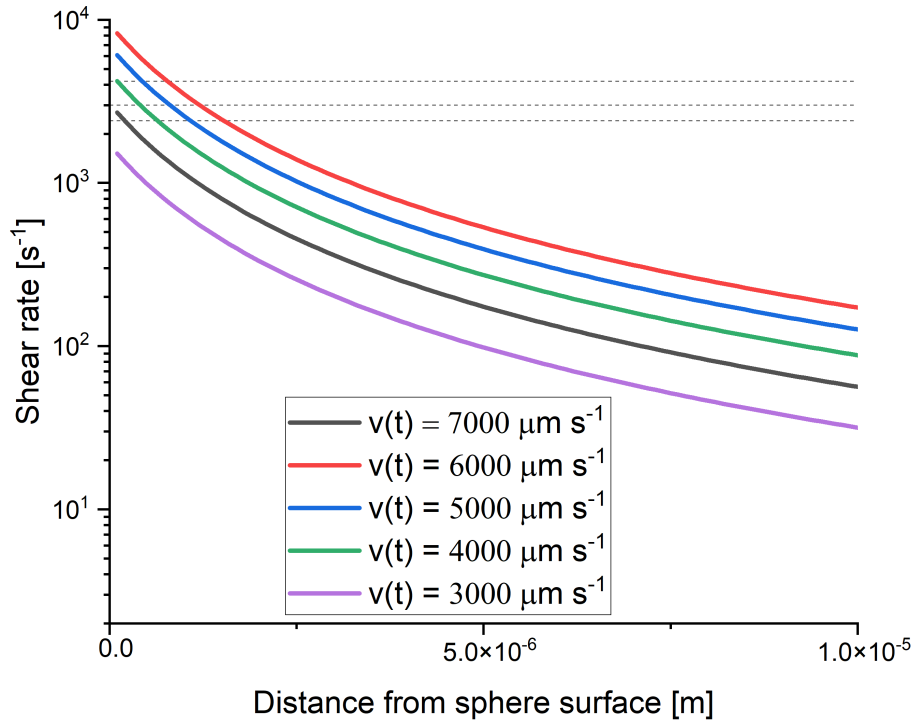


Figure 3.8: Shear rate generated by a silica microsphere ( $a = 1.57 \mu\text{m}$ ) in bulk fluid moving at different speeds. The shear rate is calculated using (3.8), with the assumption that the bead is moving in a circular path and so the speed is constant through out its path.

### 3.6 Nucleation with a Stationary and Moving Beam

As mentioned previously, shearing via optical rotation and particle displacement did not result in any localised nucleation events even while in the proximity of the droplet edge. During the experiments with the galvano-mirror, it was found that when no particle was present in the optical trap nucleation events would occur while the beam was close to the edge of the droplet, even though the solution was unsaturated. This has been reported prior [Rungsimanon2010, Liao2022], but was more interesting is how the beam's motion influenced the growth of the nucleus.

### 3.6.1 Stationary beam

Consider below in Fig. 3.9 the frames taken from a nucleation event in supersaturated glycine solution ( $S = 1.03$ ), the beam is a stationary being  $\approx 3.5\mu m$  from the droplet edge. After a period of roughly 5 minutes a nucleus forms at the trap focus, growing quickly (growth rate was approximated using imageJ to be on the order of  $700 \mu m^2/min$ ) from the focal point of the trap until after roughly 6 seconds the crystal escapes. Comparing to previous literature using optical tweezers shows that the growth rate is only loosely connected to the solutions supersaturation. Local conditions play a much larger role in the growth rate than just the concentration [Flannigan2023]. A likely reason that the trap is escaped is due to the fact that crystal is far too large to be held in place and is in fact still growing as the solution is supersaturated. The key take away to remember is that the beam has no influence over the crystal shape, instead it grows outward from the trap focus. Furthermore, due to the fact that the solution is supersaturated the crystal growth cannot be contained to the trap focus. Instead the crystal escapes as its size exceeds the trap focus.

### 3.6.2 Moving Beam

To test if a rapidly moving silica bead could generate the necessary shear rate for crystal nucleation we wanted to see if a trapped silica bead could be trapped and moved in an aqueous solution.  $20 \mu L$  of glycine and water ( $S = 1.03$ ) was added to  $10 \mu L$  of a dilute water-silica mixture making the solution unsaturated ( $S \approx 0.7$ ). However, due to the beam's motion we instead encountered several unexpected results.

Shown below in Fig. 3.10 where we have the laser focus moving in a small elliptical

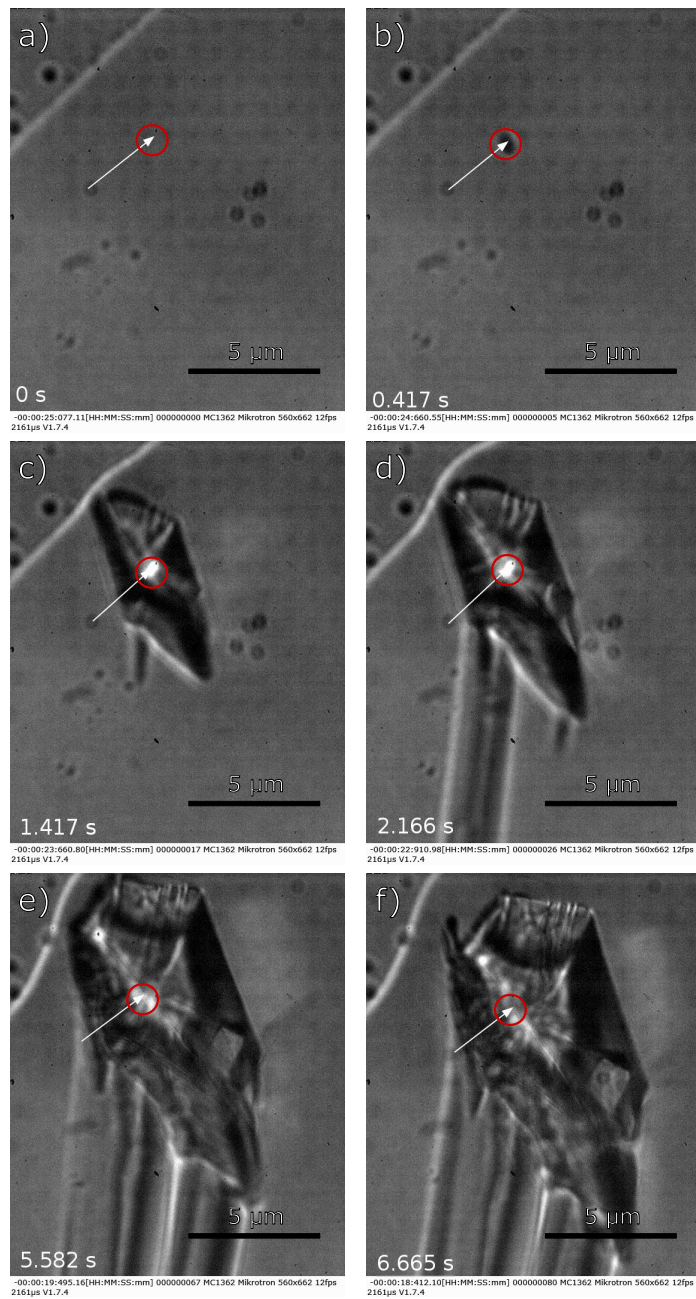


Figure 3.9: Laser induced nucleation at the edge of a droplet of supersaturated glycine solution. (b) shows the first instance of a crystal nucleus, growing quickly through (c)-(e) until after 6.665 s the crystal begins to escape the trap.

pattern; interestingly. After a few minutes we noted the appearance of several small droplets (see figure 3.11 for a larger example of these droplets). These appear too have

a wide distribution of sizes, unlike silica microspheres which have a uniform radius of  $1.57 \mu m$ . We surmise these could be small clusters of Glycine that had previously been shown to form when the aqueous solutions where irradiated with a focused laser [Tsuboi2009, Gowayed2021]. While no droplets are seen directly entering the focus a nucleus forms close to the droplet edge, unlike in Fig. 3.9 the crystal does not grow out from the focal point evenly. Due to the galvano mirror, the crystal is simultaneously being moved by and growing around the focal point of the trap. Because of this the crystal nucleus lacks a clear morphology at first. Until roughly  $20 s$  the crystal reaches a almost prismatic structure, with further irradiation increasing the size.

Interestingly the galvano-mirror allows the trap to impart a slight torque on the crystal, as shown in fig. 3.10(c) and (d), where even though the crystal is not directly in the trap focus it rotates in the  $x - y$  plane and gets trapped again at a corner. The rotation could not be due to fluid flow close to the surface of the crystal as the dipole moment of individual water molecules is too small to be influenced by an optical trap. In figs.3.10(e) and (f), the crystal growth becomes localised to the corner. The area growth rate between figures 3.10(a) and (d) was approximated using imageJ at  $45.03 \mu m^2/min$ , where as between figures 3.10(e) and (f) the growth rate at that particular edge was estimated at  $42.10 \mu m^2/min$ .

Nucleation in undersaturated conditions has been reported previously in  $D_2O$  [Rungsimanon2010] and  $H_2O$  [Flannigan2023], though not involving a moving beam. This modification allows for the crystal growth to be localised to a specific region of the bulk crystal whereas with a stationary beam there is no control over the crystal morphology.

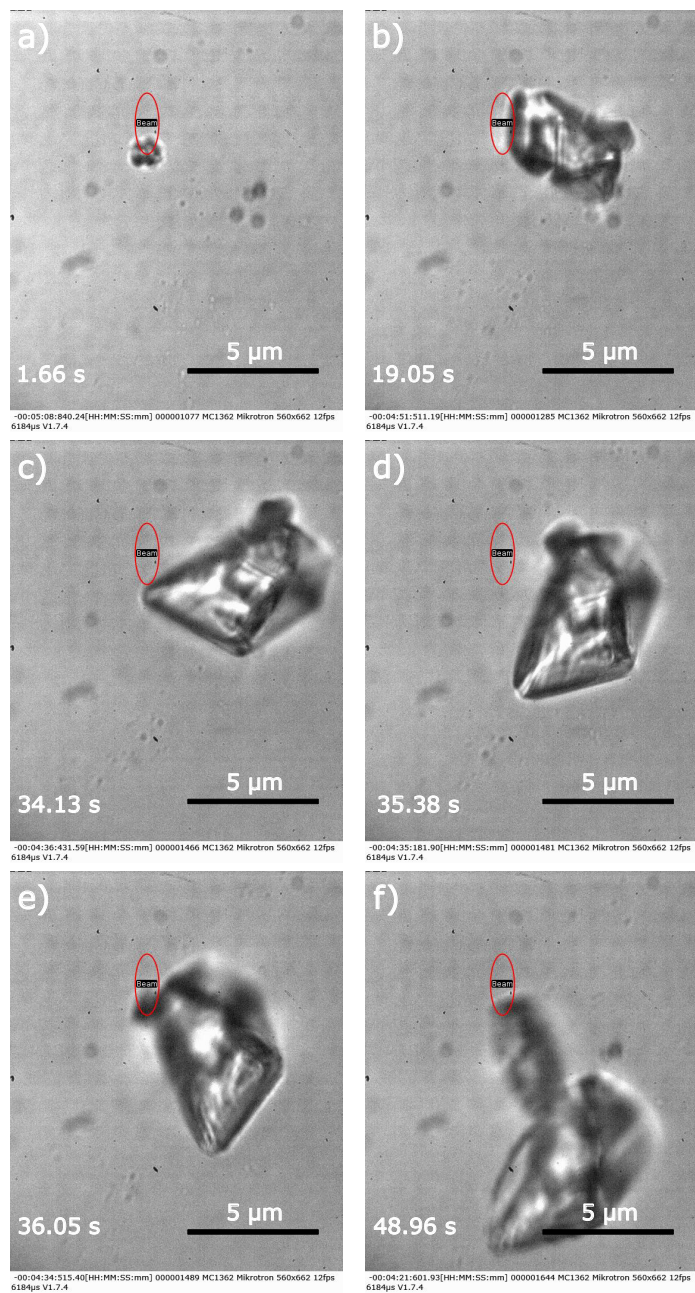


Figure 3.10: Frames from a longer video depicting the growth of a nucleus using a moving beam. Initially the crystal shape is amorphous (a) but eventually reaches a more regular shape (b). This crystal is still influenced by the optical trap as even when not directly irradiated by the laser the crystal rotates between (c) and (d). When the laser is focused on a corner the crystal growth is localised to that region, resulting in an elongated section forming between frames (e) and (f).

### 3.6.3 Direct trapping of Glycine clusters

One common aspect involving these droplets is the fact when brought to the laser focus the droplets would nucleate immediately [Liao2022]. A solution similar to Sec 3.6.1 was made up, but without any silica droplets. Once again the beam was focused close to the droplet edge, this time the galvano mirror was scanning a circular path (as shown in figure 3.11). After a few minutes of irradiation droplets were seen entering the camera frame, because no silica had been added these droplets had to be from the glycine solution. Trapping individual droplets did not result in immediate nucleation even after several minutes being trapped. Trying to bring two droplets together resulted in nucleation between the two droplets, compared to 3.6.1 & 3.6.2 the growth is much slower, taking nearly 40 seconds before the crystal structure becomes clearer.

The fact that these droplets can be trapped indicates they must have a higher refractive index than the surrounding solution. It has been shown that the concentration of glycine solution is correlated with the refractive indices of the liquid [Gowayed2021, Orttung1963]. This suggests that these droplets serve to provide solute material to the bulk crystal.

## 3.7 Influence of a moving beam front on seed crystals

Need to write up these results. To summarise the crystal dissolved around the laser focus instead of growing as the seed crystals are in the solution and not close to the air-solution interface

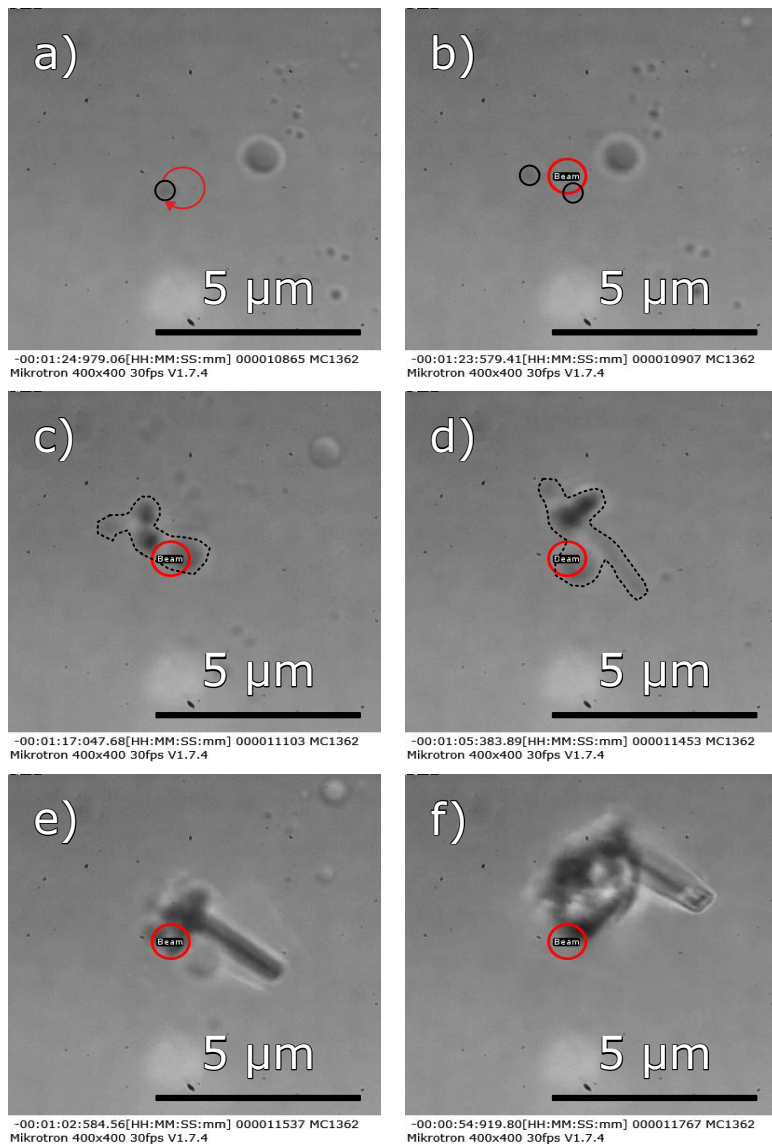


Figure 3.11: Frames from a longer video demonstrating the trapping of a glycine droplet. Solution is undersaturated glycine and water ( $S = 0.86$ ), with the laser power set at 750 mW. (a) shows a trapped droplet (outlined in black) being brought into contact with a larger droplet. (b) upon contact a nucleus can be seen between the two droplets. The growth is rather slow with the crystal having no clear defined morphology through (c) and (d). Between frames (e) and (f) the larger droplet finally joins the main crystal.

### 3.8 Summary of Moving Beam Phenomena

To summarise, the introduction of a moving beam helps to accelerate the local growth of a newly formed crystal. This is due to the presence of glycine droplets that accumulate near the interface between the liquid solution and air. The theory behind the localised growth can be summarised thusly.

Initial nucleation is similar to typical optical trapping induced nucleation, with the air solution interface limiting the molecular mobility of the solute molecules [**Liao2022**, **Sugiyama2009**, **Gowayed2021**]. The moving beam front can influence the motion of the nucleus initially, but eventually the drag force means the crystal is not moved by the optical trap. Localised crystal growth occurs when the trap is close to or partially over the interface of the crystal (see figure 3.12(a)). As shown in 3.6.3, the optical trap can manipulate these droplets similar to microspheres. When in close proximity to the trap these droplets are brought towards the crystal surface (see figure 3.12(b)). These provide material that grows the crystal around that region (see figure 3.12(c)). Eventually the local solution is either depleted of solute material or the crystal front has grown to fully encompass the trap, preventing further growth (see figure 3.12(d)).

The reason the seed crystals saw no further crystal growth when irradiated with the trap is due to the fact that these experiments were carried out in a bulk solution, absent of any interfaces. As such the clusters seen in 3.6.2 & 3.6.3 are not present and cannot provide material to accelerate crystal growth.

There are still several factors that need to be investigated, but due to time constraints it was not possible to properly study this phenomena. Firstly, there is the

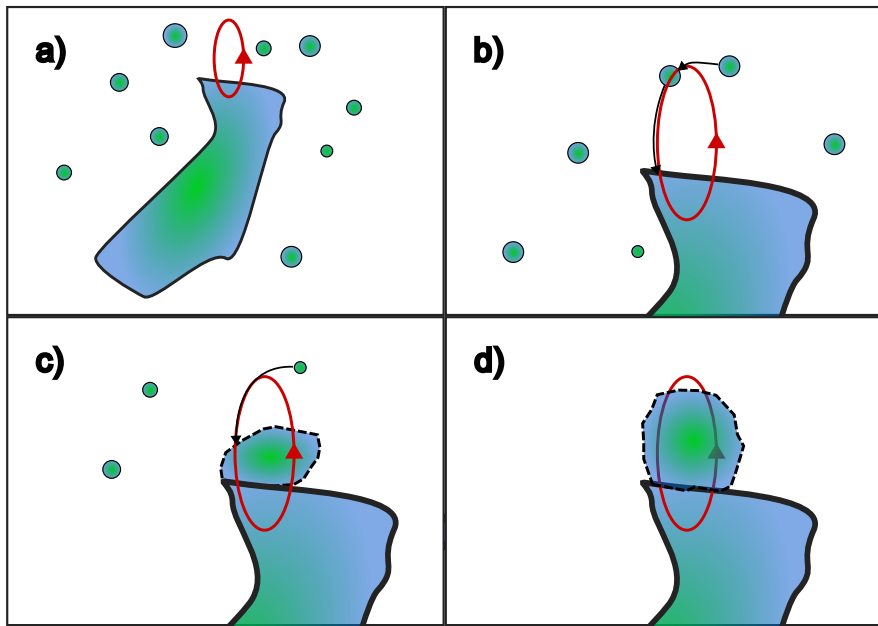


Figure 3.12: Diagram outlining how a moving beam assists in the growth of a crystal nucleus. (a) a crystal nucleus is partially trapped by a moving beam with solute droplets close to its surface. (b) droplets close to the laser focus are drawn in by gradient forces and moved towards the crystal surface. (c) these droplets provide material to the main crystal, resulting in localised growth around the laser focus. (d) eventually the crystal area either fully surrounds the laser focus or the solution surrounding the laser is depleted of solute material.

question of what conditions result in the production of concentrated droplets, it is not clear if the presence of a laser is required or if these droplets naturally occurring. Prior literature would suggest that the laser is required [**Liao2022**, **Tsuboi2009**], but this would not explain why in many cases the droplets are found far outside the influence of the optical trap. It has been suggested that optical traps can attract microspheres over a wider area, but it is hard to say that this would result in the creation of liquid droplets [**Yi2021**].

Secondly, there is the question of how these droplets supply material to the bulk crystal. In some instances it is clear that the droplets are being drawn into the trap, however, in other instances while there are no droplets close to the vicinity of the optical

### Chapter 3. Effects of localised shearing on crystal growth and nucleation

trap the crystal continues to grow. If these droplets are a necessary precursor to induce crystal nucleation then understanding how they are added to the bulk crystal may help with our understanding of the kinetics of multi-step nucleation.

### 3.9 Conclusion

## Chapter 4

# Complex Langevin dynamics of spherical dimers

Much of the calibration theory discussed in Chapter 2 assumes that the target particle in question is a single sphere, one who's scattering and motion is easily computed. However, while working with dense colloidal suspensions, one often ends up trapping more than one sphere. Li and Arlt [**Li2008**] studied the case of two microspheres trapped in a single OT and found that multiple trapped beads could be mistaken for a single trapped bead with altered trap stiffness. Theoretical studies on the case of two trapped microspheres by Xu *et al.* [**Xu2005**] employed a ray-optics based model to show that the two trapped beads are brought into physical contact with each other by optical forces and they also calculated the axial equilibrium positions of the two trapped beads as a function of their size. Experiments in [**Praveen2016**] confirmed that the two trapped beads indeed experience different trap stiffnesses in the vicinity of the same potential well. There are further discussions looking into the dynamics

of a whole host of asymmetrically shaped particles [**Loudet2014**, **ShengHua2005**, **Chetana2022**], their results all showing that predicting the behaviour of an arbitrary shaped particle comes with great difficulty due to the fact that the optical force is dependent on a greater number of variables such as orientation and size factors.

With the initial goal of the PhD being to induce nucleation events via a spherical micro-rotor the goal of this chapter was to - in a limited capacity simulate and investigate the influence of a second particle being bound to our target sphere. The choice of a dimer, instead of an amorphous solid that might better represent a growing crystalline solid, allows us to consider how the dynamics of the aggregate change by varying the size factor. We build upon the works of Vigilante *et al* [**Vigilante2020**] to consider asymmetric dimers and how varying size parameters alters the dynamics and additionally makes characterising their interactions within an optical trap more cumbersome. Attempting to simulate an amorphous aggregate is rather difficult as calculating the optical force and torque is computationally slow and orientation specific.

## 4.1 Positional and Orientational dependence of Trapping forces

If we wanted to start from first principles and determine the trap strength on our target particle the first step would be to locate the equilibrium position relative to the trap focus. For a single sphere it is easy enough to understand that its centre of mass will be drawn to focal point of the laser due to gradient forces, once there the force is analogous to a harmonic spring with a fixed trap stiffness. Now, if we consider instead

a dimer, we now have two spheres both being drawn to the focus along by the same gradient force; in addition the scattering force is significantly more complex due to both spheres scattering the electromagnetic fields. This mutual scattering between individual spheres is what makes simulating spherical aggregates far more difficult compared to a single sphere, and even harder still to predict the position where the dimer's centre of mass is in equilibrium.

Because the scattering force is only significant in the direction of beam propagation the potential well in the transverse plane can still be assumed to be harmonic around the central beam axis. The axial optical force cannot be assumed to behave as a simple harmonic trap. The methodology for computing optical forces has been covered extensively for a number of different trapping conditions [**RanhaNeves2019**], so it is relatively easy to compute the trapping force and determine where a simple sphere would be located relative to focal point of the laser by finding the position that minimises the net optical force in a negative feed back loop ( $\delta F/\delta x < 0$ ) - we can assume that for a dielectric sphere the optical torque is negligible. For a dimer (or any arbitrary spherical aggregate), we now must consider both its position and orientation and find where the net optical force and torque are minimised.

**Simulation Parameters** As a paradigmatic example, consider a dimer suspended in water ( $n_p = 1.59$ ,  $n_m = 1.33$ ) located at the focus of a Gaussian beam (more specifically a Laguerre-Gaussian beam of mode  $[0, 0]$ ), the beam is focused by a objective with numerical aperture of 1.2 and is x polarised. The size ratio of the two sphere's is given by  $a_I/a_{II} = 2$  where  $a_I$  is kept at  $1 \mu\text{m}$  unless specified otherwise; the dimer's

orientation is given by a unit vector connecting the centres of both spheres, we define the 'standard' orientation as being aligned with the direction of beam propagation direction - and therefore the 'inverted' orientation is defined when the dimer is orientated against the direction of beam orientation (see left hand side of figure 4.1).

After computing its  $T$ -matrix via *mstm* and supplying that to *ott* we compute the optical force exerted by a 50 mW laser via (2.52) in the axial direction while the dimer is in its 'standard' orientation. As expected we see a single point where the dimer will be in equilibrium, the linear fit in fig. 4.1 (a) indicates that the force can be modelled as a harmonic potential close to the equilibrium position ( $F_z \approx -\kappa_z z$ ). The second point where the axial force goes to 0 cannot be considered as equilibrium position as the positive gradient indicates that the trap is unstable unless Brownian motion is ignored.

We repeated the same calculation but now while the dimer is in its 'inverted' orientation, instead of a single point where the optical force is minimised we see that there are instead two separate equilibrium positions, one above the focus and one below the focus. In this particular example the two positions are far enough apart that both can be considered as separate harmonic traps.

We can see that both equilibrium positions have comparable axial trap stiffness ( $\kappa_z$ ), however the difference in the transverse trap stiffness ( $\kappa_x$ ) is far more noticeable. The same dimer was trapped at each of the axial equilibrium positions and the transverse force was evaluated. While in all three cases the dimer can be trapped the linear range where that would typically associated with a stable trap is far narrower in the 'standard' orientation compared to the 'inverted' cases. This highlights one of the challenges

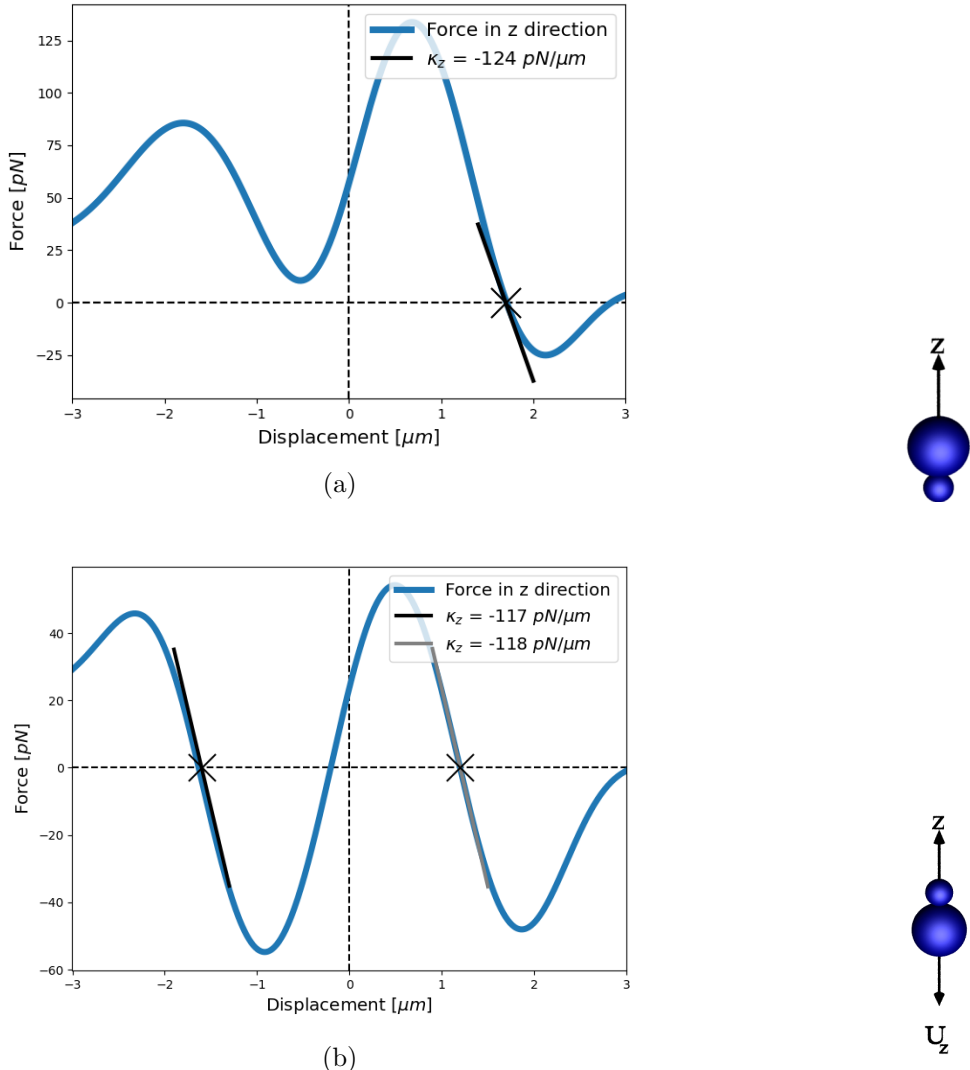


Figure 4.1: Plots of force vs displacement of the centre of mass of the dimer ( $\mu\text{m}$ ) for the case of a dimer of size ratio 2. (a) is the case where the dimer is in its' 'standard' orientation, where the dimer is trapped at  $z = 1.71 \mu\text{m}$ . (b) is the case where the dimer is in its' 'inverted' orientation, the dimer is trapped at two positions:  $z = 1.20 \mu\text{m}$  &  $z = -1.63 \mu\text{m}$ . On the left are renders to visualise the dimer orientation are shown below each plot. The black lines on each force-curve is a linear fit with the slope being reported as the trap stiffness in the legend.

involved with studying asymmetric particles, even though its a simple enough process to trap them they maybe characterised very differently depending on their relative

position and orientation towards the focus. This can have a significant impact on rheological studies - or attempting to probe any local property - as the variance in trap strength can result in large errors over repeated measurements.

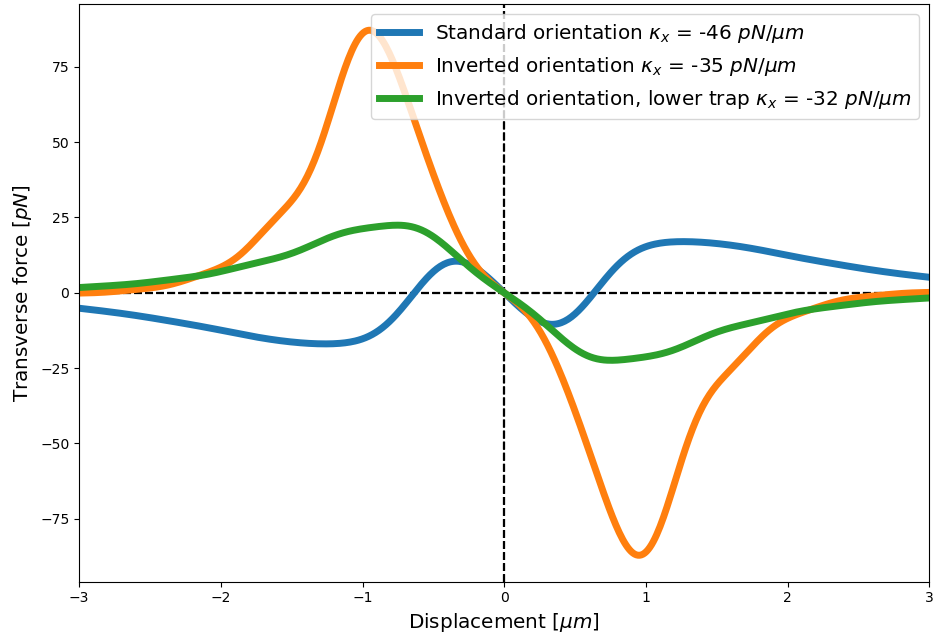


Figure 4.2: Plots of force vs displacement of the dimer's centre of mass spheres, where a positive force indicates the dimer is directed right on the x-axis, and vice versa for a negative force. The same simulation parameters are used here as in fig 4.1(a) and (c). The blue curve representing the force response for a dimer in its standard orientation, orange being the inverted case, and green the same case but placed below the focus.

For completeness the harmonic traps were located for dimers across a range of size ratios - from  $a_I/a_{II} = 1$  to  $a_I/a_{II} = 10$  - while also recording the trap stiffness for each trap. The same simulation parameters are used here as for figures 4.1 & 4.2. As shown in Fig. 4.3  $a_{II}$  decrease the dimer begins to approximate a single homogenous sphere - at least in terms of location and trap strength. However, for intermediate sized dimers (between  $a_I/a_{II} = 1.1$  to  $a_I/a_{II} = 4$ ), a second equilibrium position is found below the trapping focus. Previous work using the ray-optics model have confirmed even in the case that two spheres begin separated the electric field will align the particles as such that they make contact and are trapped together about a single trapping position [Xu2005]. Furthermore it has been shown through proper manipulation of the Gaussian or Bessel beam modes that any number of trapping potentials can be developed [Shahabadi2020] for nanoparticles. This result however, is the first example of an orientation dependent trapping situation using only a  $TEM_00$  beam. Typical experimental arrangements cannot determine much information on the axial position of a trapped particle relative to the trap focus; this result indicates not only that dimers can be trapped in multiple axial positions but also their trapping behaviour is heavily dependent on said axial position. As such it is necessary that positional information in the z-axis can be elucidated if multiple spheres are trapped simultaneously.

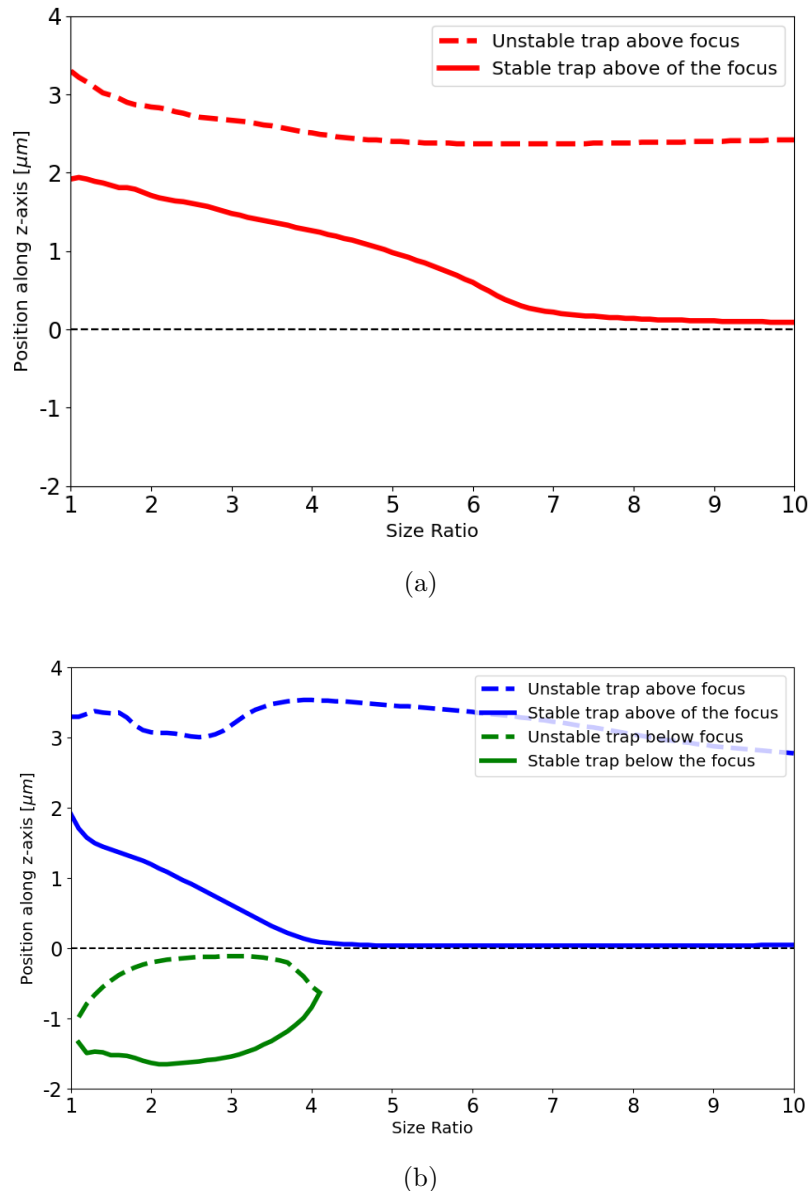


Figure 4.3: Equilibrium positions of optically trapped dimers with varying size ratio, dashed lines represent unstable traps whereas solid lines are for stable equilibrium positions. (a) shows that dimers while in their 'standard' orientation will always have a single equilibrium position. (b) shows that when the same dimer is in its' 'inverted' orientation can be trapped in two axial positions, one below the focus and one above the focus.

### 4.1.1 Non-trivial equilibrium configurations

Computing the equilibrium positions when a dimer is aligned with the electric field is relatively simple as the orientational torque is minimised (see Eq.1.5), meaning once trapped the dimer is unlikely to change orientation enough to escape the trap. However, that does not rule out the possibility that there is a stable configuration where the orientation not strictly vertical, in fact most experimental work with symmetric nano-dimers will trap them lying perpendicular to the beam direction [**Ahn2018, Reimann2018**]. Unlike in Sec. 4.1 we cannot simply measure the optical force and torque as the parameter space is too large and determining if a particular position and orientation is stable is not clear based solely on force and torque measurements [**Bui2017**]. Using the same simulation parameters as before we ran a number short simulations (total simulation time was 0.005 s) with the laser power increased to 500  $mW$ . Each simulation started with the dimer in a different starting position and orientation, due to the high laser power the dimers either escaped the trap or were stably trapped. The  $z - \theta$  phase space - where  $\theta$  is the angle between the direction of beam propagation and the dimer's orientation vector ( $\theta = 0^\circ$  is the 'standard' orientation) - can be divided into different regions depending on which equilibrium configuration is reached.

Interestingly while the trap strength of these off-axis traps are similar in magnitude to the vertically aligned dimers, but when the laser power is lowered (around 5  $mW$ ) the traps become metastable; after reaching its' equilibrium configuration the particle behaves similarly to a typically trapped dimer but the trapping potential is small enough that the dimer escapes in as little time as less than a second or after nearly a full 3

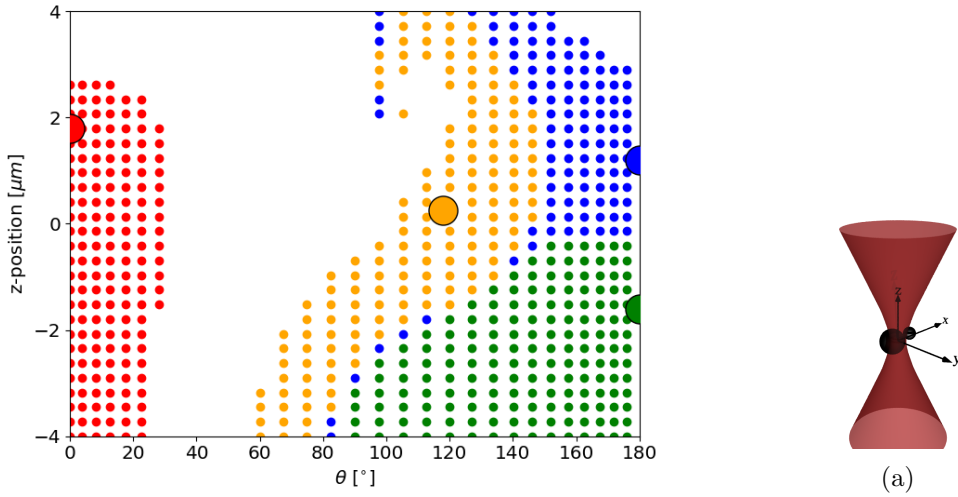


Figure 4.4: Map of  $z - \theta$  phase space using a dimer of size ratio 2 with a laser power of 500 mW ( $\theta = 0^\circ$  is the 'standard' orientation and  $\theta = 180^\circ$  is the 'inverted' orientation). The stable configurations are indicated by the larger circles and the starting conditions are colour coded to match the stable point they end up in. Right hand render shows a dimer in its off-axis configuration.

seconds. Running similar simulations but for vertical configurations sees the dimer remaining trapped, even after 30 seconds of run time, indicating that the trapping potential is far greater than the thermal energy. This suggests that the reason this off-axis configuration is due to the rotational motion more than translational motion. If the overall potential depth could be characterised then dimers placed into this orientation could be used as a micro-scale temperature alarm, where by fine tuning of the dimer's parameters would allow you to construct a potential well that can only be escaped when the local fluid temperature exceeds a certain maximum value.

## 4.2 Continuous rotational motion due to second-order scattering

One aspect that has yet to be covered in depth with regards to spherical aggregates of any construction is their interaction with circularly polarised light. For homogenous spheres the optical torque is regarded as being negligible as the spin density cannot impart angular momentum while propagating in a homogenous medium. Dimers however, have been shown to experience an optical torque [**Vigilante2020**, **Ahn2018**, **Reimann2018**] while trapped in a circular polarised beam.

First we wanted to confirm that the rotation seen in our simulations is based on the polarisation of the trapping beam. To that end, we simulated the motion of an optically trapped dimer in beams of varying polarisation ( $NA = 1.2$ ,  $P = 100 \text{ mW}$ ), the dimer is composed of polystyrene ( $n_p = 1.59$ ,  $n_m = 1.33$ ). Each simulation was run for 1 second ( $\Delta t = 10^{-5}$ ) and at the end we looked at the orientational time series; the dimer's orientation is recorded as a quaternion which can be easily converted to a 3-dimensional rotation matrix. By considering only the transverse components ( $U_{1,x}$ ,  $U_{1,y}$ ,  $U_{2,x}$ , &  $U_{2,y}$ ) of the rotation matrix and taking the Fourier transformation of their time series reveals the rotational frequency. The laser power is set to 100 mW to avoid large thermal fluctuations and so that the Fourier series of the transverse components approximates  $\delta(\omega_{rot} - f)$  - the Dirac delta function centred at the rotational frequency  $\omega_{rot}$ .

$$q(t) \rightarrow R(t) = \begin{pmatrix} U_{1,x}(t) & U_{2,x}(t) & U_{3,x}(t) \\ U_{1,y}(t) & U_{2,y}(t) & U_{3,y}(t) \\ U_{1,z}(t) & U_{2,z}(t) & U_{3,z}(t) \end{pmatrix}$$

$$\rightarrow \int_{-\infty}^{\infty} R(t) e^{-i2\pi f t} dt = \begin{pmatrix} \delta(\omega_{rot} - f) & \delta(\omega_{rot} - f) & \delta(f) \\ \delta(\omega_{rot} - f) & \delta(\omega_{rot} - f) & \delta(f) \\ \delta(f) & \delta(f) & \delta(f) \end{pmatrix} \quad (4.1)$$

If the rotational frequency was not immediately obvious the simulation was repeated but over a longer simulation time. Four different size ratio of dimers were studied, both in their 'standard' and 'inverted' orientations. The results of this are displayed in Fig. 4.5:

This shows us that these optical rotations are polarisation dependent and not merely an example of the dimer scattering light asymmetrically. The question then becomes, by what mechanism is the angular momentum of the trapping beam being transferred to the dimer.

The rotation was first noted by Vigilante and co-workers who only considered this behaviour for a symmetric dimer [Vigilante2020]. In their work they attribute this to spin-curl effects, in which the curl of the spin density leads to a second order optical force that orbits around the beams central axis [Yevick2017]. While several papers have demonstrated this phenomena [Zhao2007, Zhao2009, Wang2010] it was only properly formalised by [Ruffner2012]. In which they showed that the seemingly random trajectory of a trapped sphere was biased by the polarisation state of the

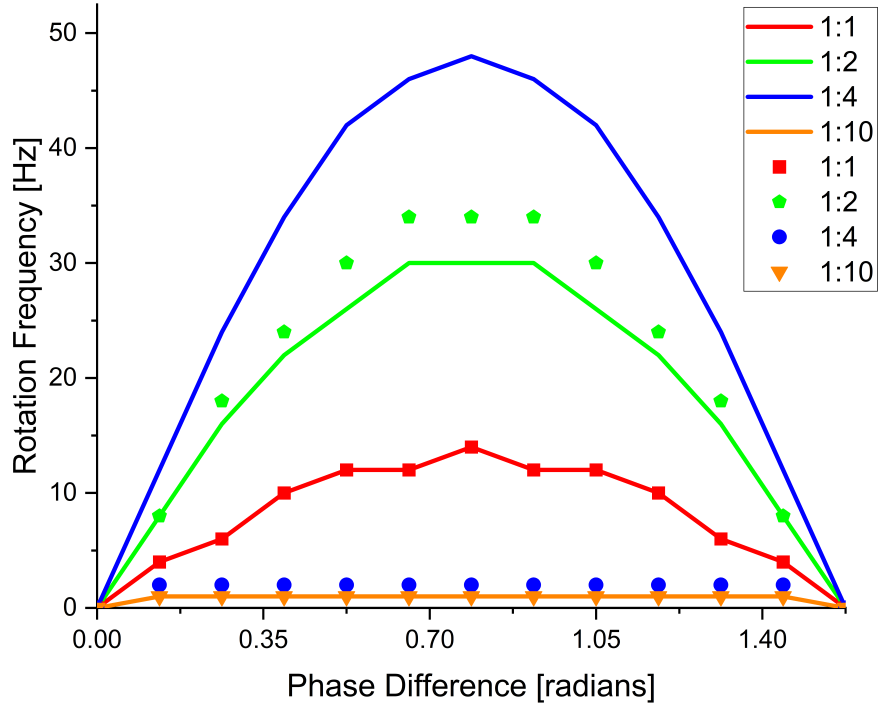


Figure 4.5: Rotation frequency vs component phase difference for differently sized dimers. The solid lines represent the rotation rate experienced while the dimer is in its standard orientation, whereas the solid points are for the case where the orientation is inverted. Laser power = 100 mW.

trapping beam. While not immediately evident from the trajectory the helicity of the trapping beam was revealed by computing the particle's probability flux using.

$$j(r) = \frac{1}{N-1} \sum_{j=1}^{N-1} \frac{r_{j+1} - r_j}{\tau} \delta_{sigma_j} \left( r - \frac{r_{j+1} + r_j}{2} \right) \quad (4.2)$$

where  $\delta_{sigma_j}$  is the kernel of an adaptive density estimator [Silverman1986]. (4.2) describes the direction a trapped sphere is most likely move in given our statistical knowledge of the trajectories probability density function. A finite estimation of the

density function  $p(r)$  is used in [Ruffner2012].

$$p(r) = \frac{1}{N} \sum_{j=1}^N \delta_{\sigma_j}(r - r_j) \quad (4.3)$$

The probability flux reveals a biased motion in the trajectory of a single sphere (see Fig. 4.6). This biased motion results in a slight orbital motion about the central axis of the trapping beam, the orbital frequency is shown to be proportional to the polarisation state of the trapping beam.

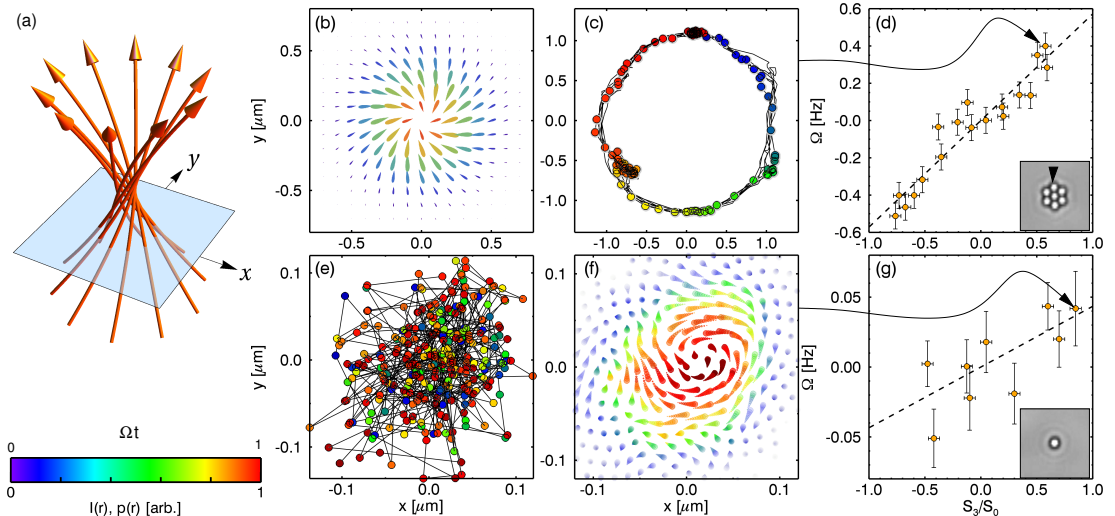


Figure 4.6: Figure reused from [Ruffner2012]. (a) shows how the momentum density of a Gaussian beam is twisted while using circularly polarised light. The top row (figures (b)-(d)) shows a 7 sphere cluster trapped in a circularly polarised beam. Due to the clusters asymmetric susceptibility to polarization the cluster rotates in the  $x - y$  plane. Whereas the bottom row (figures (e) - (g)) show the similar results for a single sphere. In this instance the sphere does not rotate but instead orbits the beam axis. In both instances the motion is proportional to the degree of polarisation (see figures (d) and (g)) but for the single sphere this motion is only revealed when using (4.2) & (4.3). Reused with permission from author

While the results from [Ruffner2012] suggest that the optical rotation seen in asymmetric dimers is attributed to the same spin-curl forces there are several dis-

crepancies that cannot be explained purely by the spin-curl force. Firstly, there is the question of how the spin-curl force results in an optical torque: Comparing figures 4.6(c) and (e) we can see that the behaviour of the 7 sphere cluster rotates about the central axis whereas the single sphere has an only slight orbital bias in its motion. The authors attributed this to the fact that the cluster is scattering light where the spin-curl force is more substantial due to it having a wider profile. This would suggest that particles' whose longer axis lies in the plane perpendicular to the direction of propagation should experience any notable degree of torque. And indeed this appears to be the case for a number of experiments involving nano-dimers and ellipsoidal particles [**Ahn2018**, **Reimann2018**].

It does raise the question of how come our simulations show that despite the dimer being orientated so their long axis' align with the parallel to the direction of propagation they still readily rotate. You would not expect that the addition of a single additional sphere should drastically adjust the torque especially if said sphere is relatively small. However when we measured the optical torque of a single sphere and a dimer -  $a_I/a_{II} = 10$  - we found the exact opposite. In both cases we used the same trapping beam as used for figure 4.5 but with a circularly polarised beam. Both the sphere and dimer were rotated in the  $x - z$  plane and the all three components of the optical torque were recorded.

It should be noted that the difference in magnitude is not clearly shown in figure 4.7. In truth, the optical torque acting on the dimer  $10^{13}$  times greater than the torque applied to the single sphere. The torques about the  $x$  and  $y$  axis can be somewhat understood as the second sphere is being drawn back towards the centre of the trap by

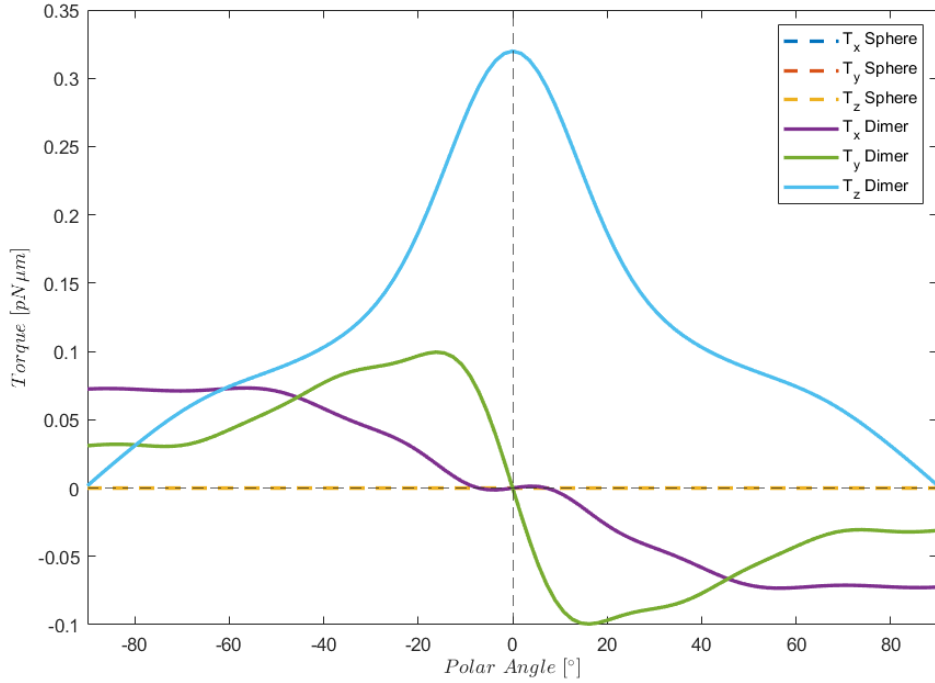


Figure 4.7: Optical torque experienced by a dimer ( $a_I/a_{II} = 10$ ) and a single isotropic sphere. Both were rotated in the  $x - z$  plane and the angle between  $U_z$  and the beam axis gives the polar angle. The solid lines denote the torque experienced by the dimer whereas the dashed lines represent the torque experienced by the sphere.

the gradient forces. The same cannot be said for the  $z$  component of the optical torque; while this effect could still be attributed to the spin-curl force, but it is clear that the internal scattering between the two spheres has some unintended effects.

By repeating the same kinds of simulation as used in 4.5 but for a circularly polarised beam  $\phi = 90^\circ$  it was found that not only is the rotation rate dependent on the size of the dimer, but also on its orientation and therefore their axial position.

It is difficult to see from the graph, but the rotation rate never truly goes down to zero, reaching a minimum of 2 Hz, which would imply that a second sphere of radius 200 nm is enough to induce rotational motion. This brings into question what mecha-

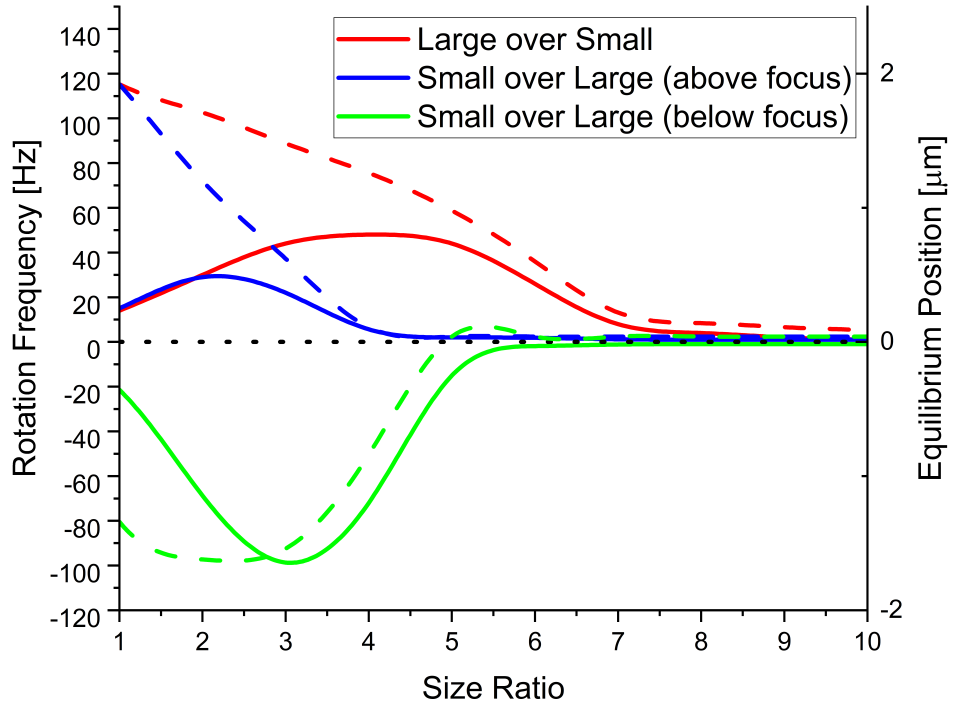


Figure 4.8: Rotation rate plotted against dimer size ratio while trapped in a circularly polarised beam; a positive rotation rate indicates clockwise rotation, whereas a negative rotation rate indicates counter-clockwise rotation. The red line is for the case of a dimer in its 'standard' orientation. The blue line is for the case when the dimer is in its 'inverted' orientation while trapped above the focus of the beam. And lastly the green line is for the case when the dimer is in its 'inverted' orientation, but when it is trapped below the focus of the beam.

nism is generating the optical torque. We used *mstm* to look at the stokes parameters from the scattered field from a simple plane wave incident on a symmetric dimer, the proportion of circularly polarised light is minimal compared to the proportion of plane polarised light, which indicates that this rotational motion is not due to any inhomogeneity in the dimer that might impart angular momentum to the scattered beam - as compared to a anisotropic scatterer like vaterite. Therefore the rotational motion must be due to

These results are somewhat contradictory to other work with silica dimers [**Ahn2018**, **Debuyschere2023**, **Reimann2018**]; previous experiments have trapped the dimer in an orientation perpendicular to the beam propagation direction. The rotational motion is attributed to the dimers asymmetric geometry creating an unbalanced polarisation susceptibility along its long axis as compared to its short axis; therefore its long axis is aligned with the polarisation vector and can rotate freely [**Ahn2018**]. This however cannot be the case with our simulations as the dimer rotates about its long axis, meaning there cannot be an asymmetric axis to align with the beam's polarisation vector. Furthermore, we see a non-linear increase in the rotational speed of our dimers with size, the drag torque from the surrounding fluid is  $\propto r^3$  so the expectation is that the rotation frequency should fall off with increasing size. This indicates that the rotational motion is due to the shape asymmetry of the dimer and not solely due to the beam's angular momentum. Measurement of this photo-kinetic force is difficult to achieve due to the fact that previous analysis was conducted in the Rayleigh regime, where the polarizability of our dimer can be approximated as:

$$\mathbf{p}(\mathbf{r}, t) = \alpha_x E_x(\mathbf{r}, t) \hat{\mathbf{e}}_x + \alpha_y E_y(\mathbf{r}, t) \hat{\mathbf{e}}_y + \alpha_z E_z(\mathbf{r}, t) \hat{\mathbf{e}}_z \quad (4.4)$$

where the polarizability is given as a 3D vector for the three principle Cartesian directions. In order to measure the magnitude of second order contributions we would need to construct a dipole array that fully captures the scattering of a dimer. Measuring the optical torque makes it clear that the polarizability is a contributing factor to this optical rotation phenomena. Rotating a symmetric dimer in the  $x-z$  plane reveals that

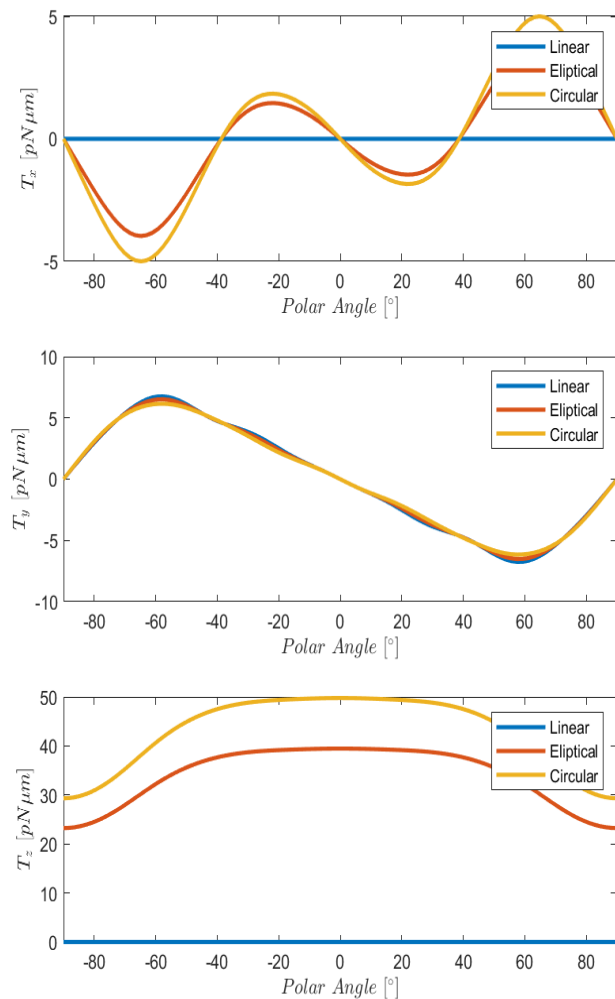


Figure 4.9: Optical torque against polar angle  $\theta$  about the three primary axis (top: torque about the x-axis; middle: torque about the y-axis; bottom: torque about the z-axis) on a symmetric dimer in linear, elliptical, and circular polarisation beams. Diagram to the right is for visual clarity about the direction of  $\theta$ .

while the dimer can be rotated in an orientation perpendicular to the beam rotational torque is maximised when rotated while aligned with the optical axis.

### 4.2.1 Gyroscopic Precession using asymmetric dimers

As mentioned in section 4.1.1 for specificity sized dimers there is the potential for non-vertical trapping orientations in which the dimer is still stably trapped. When a circularly polarised beam is used the dimer exhibits gyroscopic precession. As shown in fig 4.10 the dimer's trajectory exhibits periodic rotation about its long axis  $U_z$ , precession motion as the dimer spins around the central beam axis, and nutation motion as the dimer's orientation rocks backwards and forwards.

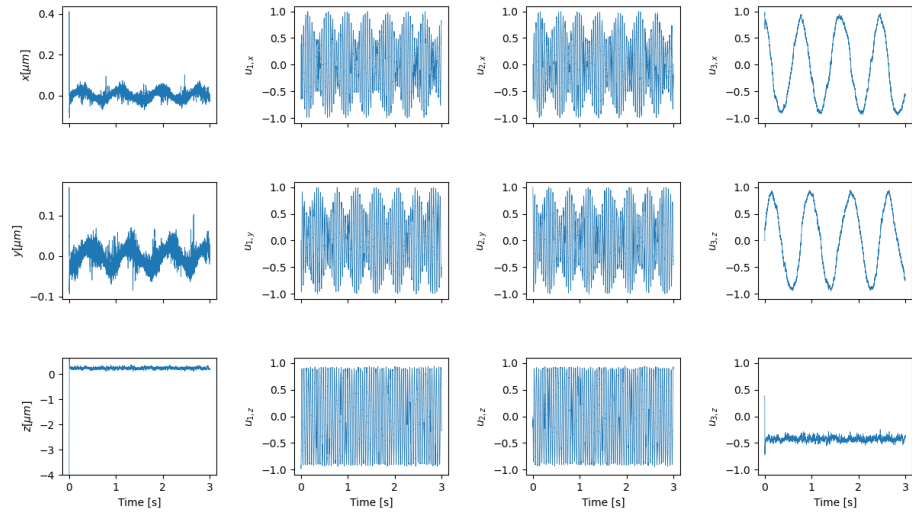


Figure 4.10: 3 second trajectory of a dimer ( $a_I/a_{II} = 2$ ) trapped in an off axis orientation with a circularly polarised beam ( $P = 100 \text{ mW}$ ). The far left column depicts the dimer's centre of mass position with time; middle two columns are the  $x$ ,  $y$ , and  $z$  components of the vectors  $u_x$  and  $u_y$ ; last column depicts the components of the vector  $u_z$  which defines the dimer's orientation.

Applying a Fourier analysis to the above trajectory reveals the 3 fundamental frequencies typically associated with precession; the  $u_{z,1}$  and  $x(t)$  series show a precession frequency of  $1.33 \text{ Hz}$  whereas the series  $u_{x,1}$  and  $u_{y,1}$  show a combined periodic signal

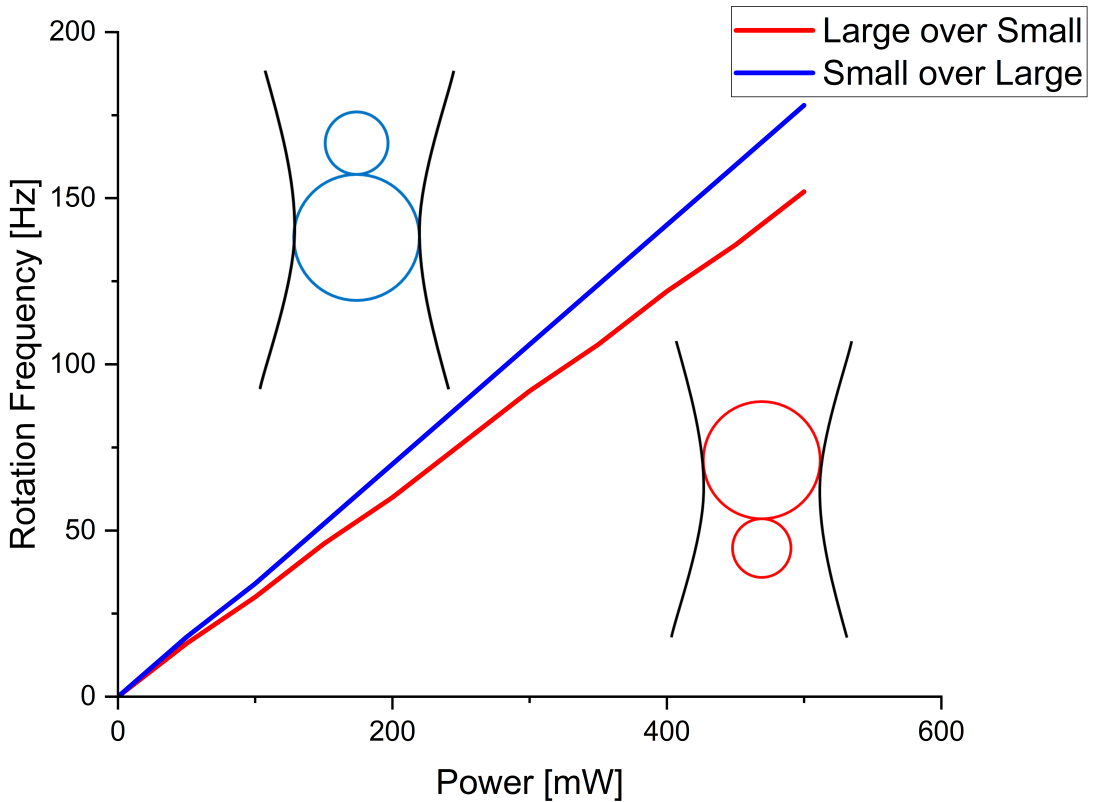


Figure 4.11: Rotational frequency vs laser power for a dimer in both vertical orientations.

- a rotational frequency of  $23\text{ Hz}$  and a nutation frequency of  $20\text{ Hz}$ . Previous studies into amorphous silica nanoparticles found a linear relationship with the rotational frequency and the laser power, but no such relationship existed with the precession frequency. Our own results shows a similar linear relationship with vertically aligned dimers.

The linear relationship could partly be due to fact that we do not account for the change in viscous forces with increasing laser power. Due to the localised heating effect It is far more likely that the rotational frequency reaches a maximum value assuming that the bulk fluid can readily absorb the laser.

This gyroscopic motion has been demonstrated previously in nanoparticles [**Zhu2021**, **Rashid2018**, **Hoang2016**, **Kuhn2016**] but has not been observed for micron scale aggregates. Since the torque applied to the dimer is computed by evaluating the beam coefficients of the scattered field it is difficult to apply this result to micro-rheology experiments as one would need to know the exact magnitude of the optical torque ahead of time in order to make estimations about the local fluid viscosity. This is trivial for a birefringent spherical particle, less so for spherical aggregates whose equilibrium position and orientation are unknown. However, further analysis of the mechanism behind the precessive motion of off-axis dimers may provide insights into controlling Brownian motion. An experimental work trying to 'cool' nano-dimers by controlling the motion in all 6 degrees of freedom found that even while the rotation about the short axis' could be controlled the free rotation around the dimers' long axis resulted in an unpredictable torsional vibration [**Bang2020**]. Understanding how rotational motion arises in the Mie-Regieme could allow researchers to build a robust theoretical framework to construct beam structures that eliminate any unwanted rotational motion from a target particle. Conversely, the same framework could allow for precise measurements of the optical torque applied to a target particle, allowing for characterisation of complex shaped particles' interactions with an optical trap.

### 4.3 Characterisation of asymmetric dimers via PSD analysis

As discussed in 2.7, one of the methods developed to work in conjunction with [Vigilante2020] is a simulated quadrant photo diode for as a position detection system. While it is possible to extract all of the relevant dynamical information from a simulation, confirming the same behaviour in an experimental setting can be challenging if dealing with a non-birefringent particle.

As a benchmark we start by considering a single sphere within an optical trap. A single polystyrene sphere suspended in water ( $a = 1\mu m$ ,  $n_p = 1.59$ ,  $n_m = 1.33$ ) is trapped by a focus Gaussian beam and its trajectory was recorded. A 3 second is trajectory is a typical measurement time for collecting a power spectrum, the spectra was fitted to eq. 2.45.

As shown in fig. 4.12, the two power spectra report different corner frequencies which would indicate that the trap is not perfectly circular. Using *ott* we can compare the expected trap strength to what is reported by a quadrant photo diode:

Fitting parameter	<i>ott</i> estimates		QPD fitting		Simulation fitting	
$f_c$ [Hz]	447	450	439	474	523	513
$\kappa$ [ $pN/\mu m$ ]	53.05	53.40	51.96	56.09	61.94	60.7
Ellipticity	8.16 %		27.17 %		13.8 %	

Where the ellipticity of the beam is given by  $e = (1 - \kappa_y/\kappa_x)^{0.5}$  and is a measure of the symmetry of the beam wavefront. Its clear from these initial results that the QPD is more sensitive to changes along the y-axis than the x-axis when compared to the direct

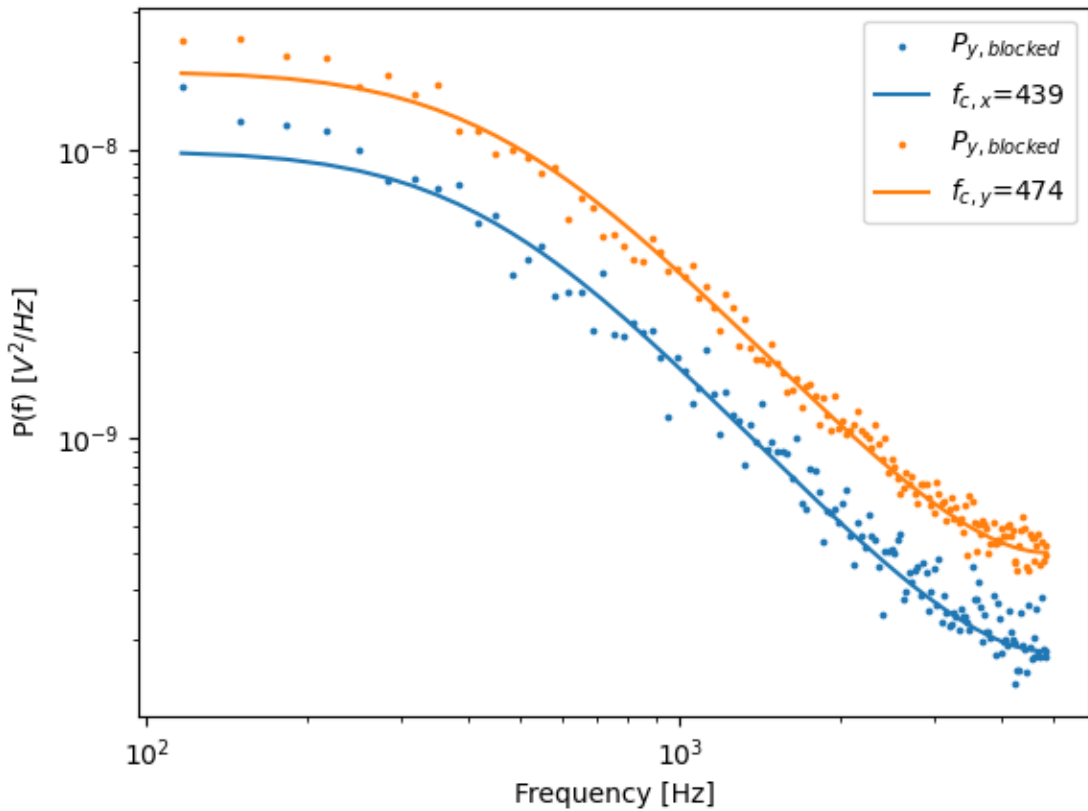


Figure 4.12: Recorded power spectra fitted to eq. 2.45, scattered points represents the blocked data ( $n_b = 100$ ). Corner frequency for the Lorentzian curves are reported in the legend.

*ott* calculations. Typically, even an industrial Gaussian beam will produce an elliptical diffraction limit spot when heavily focused; in their tutorial for optimizing the PSD analysis, Berg and Sorensen reported a ellipticity of around 15 % after a total calibration time of 81 seconds [**BergSoerensen2004**]. The reason for this discrepancy can be explained partly by the fact that our estimation of the trap geometry via *ott* is based on the force-displacement curve while the sphere is moving in only one direction, whereas the QPD is estimating the trap geometry by extrapolating from far field scattering signals. We now consider a symmetric dimer in identical simulative conditions.

Fitting parameter	<i>ott</i> estimate		QPD fitting		Simulation fitting	
$f_c$ [Hz]	409	334	431	424	274	285
$\kappa$ [ $pN/\mu m$ ]	48.51	39.58	51.13	50.26	32.45	33.75
Ellipticity	42.8 %		12.7 %		13.8 %	

Now we see that the *ott* predicts a more elliptical trap compared to the QPD model which says the trap is far more symmetrical while trapping a symmetric dimer. A potential reason that *ott* no longer expects a circular trap could be due to how it computes the beam shape coefficients; by point matching in the far field before the focus means a loss in accuracy for objects that trap above the focus. The change in the QPD estimation can be partially explained by the fact that rotational effects are not accounted for in the Lorentzian power spectra, only translational motion. Typically, rotational motion is only ever detected when it is periodic (take for example Fig. 3.4), when the motion is stochastic the entire power spectra is effected making it near impossible to separate the translational and rotational contributions from a single power spectra.

## 4.4 Conclusions

Considering the simplicity of a scatterer such as a dimer, one would assume that the dynamics of such an object would be relatively easy to predict. Simulations of dimers in the Mie regime show that not only do they have multiple positions and orientations in which they can be trapped but also that their interaction with circularly polarised light is heavily dependent on the axial position and trapping orientation. Dimer's have the potential to be used as adaptive micro-rotors, being simple to synthesise and can

## Chapter 4. Complex Langevin dynamics of spherical dimers

be made out of any material of choice, but in order for these particles to be used as such one needs a means of characterising the optical torque applied. While estimations can be made in the Rayleigh regime due to the dimer being treated as point dipole, Mie regime micro rotors require an in-depth theoretical description of the mechanism that is creating this optical torque.

## Chapter 5

# Detection and Characterisation of rotational spherical aggregate rotational dynamics

As outlined in the end of Chapter 4, one of the difficulties in characterising interactions with asymmetric objects is the coupled motion between translation and rotation. This can be somewhat ignored if the rotational motion is periodic, like when the power spectra of elliptical polystyrene particles was fitted by Yogesh *et al* [**Yogesha2011PreciseCO**], however in the case where rotational motion is stochastic the problem is more complex. For example, when a novel trap characterisation technique was implemented by Saffron *et al* [**BarZiv1997**, **Meller1998**], they were able to use dynamic light scattering to characterise both the axial and lateral trap stiffness acting on microspheres. The only drawback admitted to in their work was that the technique was constrained to

Chapter 5. Detection and Characterisation of rotational spherical aggregate  
rotational dynamics

isotropic scatters as their theoretical model for describing the auto-correlation function was predicated on the fact that any variations in the signal are due to the particles translational motion within the confines of a cylindrical trap [BarZiv1997]. However, it is somewhat naive to assume that the orientational change

## 5.1 Simulative QPD

A QPD is simply a measure of the total electric field incident on a photo diode, in order to accurately simulate a QPD response careful consideration of how the Electromagnetic fields are defined is required.

### 5.1.1 Incident beam

The incident beam is simple enough to define given our set up parameters, for the sake of simplicity we assume that our beam is a Laguerre-Gaussian beam of mode  $[0.0, 0.0]$  (which is simply a pure Gaussian beam). \*Ott\* uses a point matching approach to approximate the beam shape coefficients of the incident field by fitting it to the far field estimate, the beam is of the form:

$$E_{inc}(kr) = \sum_n^{\infty} \sum_{m=-n}^n a_{mn} RgM_{nm}(kr) + b_{nm} RgN_{nm}(kr) \quad (5.1)$$

Where  $RgM_{nm}(kr)$  &  $RgN_{nm}(kr)$  are regular vector spherical wave functions, \*ott\* allows us to change the basis of the the incident beam to suit our needs, because we are measuring in the far field we want to set our incident beam to be an outgoing

Chapter 5. Detection and Characterisation of rotational spherical aggregate  
rotational dynamics

spherical wave so that we can compute the intensity on the QPD. For spherical waves the field can either be expressed as an incoming/outgoing wave (with a singularity at the origin) or as a regular wave around the origin; for incoming/outgoing waves the wave functions use the first/second forms of the Hankel function respectfully. In order to compute the regular spherical wave at the origin we replace the Hankel function with the Bessel function which is simply the average of the first and second forms of the Hankel function, so at the origin we avoid a singularity of the EM field.

We can if we want further restrict the incident beam by applying setting the truncation angle to match our microscope object, this essentially applies a cut off point to the In order to compute the scattering from the target particle \*ott\* uses the t-matrix method, this is not essential for a simple sphere but is far more important for complex shaped particles such as our dimers. If the T-matrix is loaded in from \*mstm\* we need to convert the \*mstm\* t-matrix to a form more suitable for \*ott\*:

$$\begin{pmatrix} p_{nm} \\ q_{nm} \end{pmatrix} = T \begin{pmatrix} a_{nm} \\ b_{nm} \end{pmatrix} = \begin{pmatrix} aT_{nm}^{TM} & aT_{nm}^{TE} \\ bT_{nm}^{TM} & bT_{nm}^{TE} \end{pmatrix} \begin{pmatrix} a_{nm} \\ b_{nm} \end{pmatrix} \quad (5.2)$$

For \*mstm\* the T-matrix is packed as a column vector:

$$T_{MSTM} = \begin{bmatrix} aT_{n,-n}^{TE} & bT_{n,-n}^{TE} \\ aT_{n,-n+1}^{TE} & bT_{n,-n+1}^{TE} \\ \dots & \dots \\ aT_{n,n}^{TE} & bT_{n,n}^{TE} \\ \hline bT_{n,-n}^{TM} & bT_{n,-n}^{TM} \end{bmatrix} \quad (5.3)$$

Where as \*ott\* packs the T-matrix with sub matrices:

$$T_{Ott} = \begin{bmatrix} \begin{pmatrix} aT_{n,-n}^{TM} & aT_{n,-n}^{TE} \\ bT_{n,-n}^{TM} & bT_{n,-n}^{TE} \end{pmatrix} \\ \begin{pmatrix} aT_{n,-n+1}^{TM} & aT_{n,-n+1}^{TE} \\ bT_{n,-n+1}^{TM} & bT_{n,-n+1}^{TE} \end{pmatrix} \\ \dots \\ \begin{pmatrix} aT_{nm}^{TM} & aT_{nm}^{TE} \\ bT_{nm}^{TM} & bT_{nm}^{TE} \end{pmatrix} \end{bmatrix} \quad (5.4)$$

### 5.1.2 Scattered and Total Fields

With the T-matrix in hand we can compute the scattered beam by multiplying our beam shape coefficients with the T-matrix to get out the scattered field. Now in order to simulate a real QPD we need to account for the motion of our target particle within the trap, taking a typical trajectory file we read off each line in order to translate and

## Chapter 5. Detection and Characterisation of rotational spherical aggregate rotational dynamics

rotate the beam. Translation is a rather simple process, simply involving us to shift the beam laterally, small deflections are generally unnoticeable for the incident beam but are much more noticeable in the scattered field (the below figure shows the result of shifting the incident beam  $1\mu m$  to the right):

The QPD does not just pick up the scattered light however, it instead is receiving a combined signal from both the incident field and scattered field simultaneously, as mentioned by [Rohrbach](#) the total intensity can be computed by taking the magnitude of both the incident field \*focused at the origin  $[0, 0, 0]$ \* and the scattered field originating from  $[\delta x, \delta y, \delta z]$  (top left and bottom right plots in the above figure). This means we do not need to worry about any translation effects being 'double-counted' in the QPD's signal as we are only shifting the scattered field meaning the QPD signal is only picking up the interference due to the shifted scattered field. I conducted some unitary tests where I scanned the beam position laterally along the x-axis and measured the QPD's 'x-signal' for x, circular and y-polarized light which yielded the following QPD responses. The target particle was  $1.57 \mu m$  and the scan range is set to  $[-4, 4\mu m]$

Where  $S_x$  is given in blue, and  $S_y$  is given in orange, the plots make it clear that the polarisation of the beam have a minimal effect on the QPD signals if the particle is traversing in one direction, its clear that the displacement from the beam centre is far more important than the polarization of said beam. This is backed up when we look at [Rohrbach's](#) results, who studied a  $150 nm$  sphere ( $n = 1.57$ ) submerged in water with a focusing lens of numerical aperture 1.2, and beam power of  $3 mW$ . The condensing lens' numerical aperture was not set to a particular value and was instead varied between 0.13-1.2, as a compromise we selected a condenser numerical aperture

of 0.525, corresponding to a acceptance angle of  $31.6^\circ$ .

Where the points are Rohrbach's results and the solid line's are our QPD's own replication. The dashed horizontal lines on the left represent the maximum displacement in the lateral displacement which is given by the combined beam radius and particle radius (assuming a beam radius of  $0.54 \mu m$ ); we can say that any displacements beyond this distance, while non-zero these displacements are unlikely to occur while a particle is trapped at the focus. Whereas the right most plot's dashed horizontal lines represents the Rayleigh range of the Gaussian beam, this represents the transition between plane wave and spherical wave regimes. Interestingly while our results close to Rohrbach's while close to the focus we see it begins to diverge beyond the first peak, this shouldn't be an issue for a typical optical tweezer calibration as we can assume that the maximum displacement will be within this linear regime.

Now the above plots only consider the QPD response to movements along the cartesian axis, however obviously for any Brownian motion the movements are a combination of displacements in each cartesian direction. We might assume naively that any displacement  $\Delta r$  will result in a linear combination of QPD responses; for low precision force measurements this assumption is adequate, however when high precision is required we find that this assumption is longer adequate due to something referred to as cross-talk. Cross talk arises when movement in one direction results in a QPD response change in the other orthogonal direction, there is no one reason for this effect, it could be a result of differing sensitivity in the photo diodes, it could be because the scattering is slightly asymmetric meaning the scattering falls outside the QPD, or it could be a result of mis-alignment in the set up. This can have unintended effects, for example

it may lead to the apparent rise of a curved trajectory rather than a straight path:

Consider a particle moving purely along the x-axis, with 0 cross-talk the QPD response should perfectly match the above curve  $S_x(x, 0, z_0)$ , with  $S_y$  being flat in comparison; if however there is cross talk between the channels then  $S_y$  will have some significant non-zero value (or it may even grow with increasing displacement), implying that the particle is actually moving in both the x and y directions simultaneously. First we checked for this by measuring the QPD response for random positions within the XY plane:

Where  $S_x$  is plotted on top and  $S_y$  is plotted below, as shown by the above plot we see that they still possess similar shapes to the previous plots but now with additional noise terms, making it clear that for any trajectory there will be cross talk. This means that trying to get a one-to-one measurement of the particle's displacement is not possible by simply looking at the QPD response, to do that we can need to calibrate the trap.

[Berg and Flyvbjerg](#) have an excellent breakdown for accurately calibrating an optical tweezer, in addition they discuss how to minimise cross-talk effects. For two correlated power spectra, the cross correlation is given as:

$$P_x = |\hat{S}_x(f)|^2 \quad (5.5)$$

$$P_y = |\hat{S}_y(f)|^2 \quad (5.6)$$

$$\rightarrow P_{xy} = \text{Re}(\hat{S}_x \hat{S}_y^*) \quad (5.7)$$

Now if the two directions are correlated then  $|P_{xy}|^2/P_x P_y$  should be non-zero for all frequencies, in order to eliminate cross-talk effects we need to minimise the cross-correlation for all frequencies. They showed that it is possible to find a transformation of the time series  $(x(t), y(t))$  to one that possesses the property that  $P_{x'y'}(f) = 0$  for all frequencies. They found these transformed positions by minimising the sum cross-correlation:

$$\sum \frac{P_{x'y'}}{P_{x'} P_{y'}} = \sum \frac{(1 + bc)P_{xy} + cP_x + bP_y}{(P_x + 2bP_{xy} + b^2P_y)(Py + 2cP_{xy} + c^2P_y)} \quad (5.8)$$

Where  $b$  and  $c$  are fitting parameters, by minimising this function one can adjust each spectra in order to eliminate cross talk effects and provide a more accurate calibration of the optical trap. Furthermore with the fitting completed, the time series can be then transformed in order to eliminate the cross talk effects:

$$x'(t) = S_x(t) + bS_y(t), \quad y'(t) = S_y(t) + cS_x(t) \quad (5.9)$$

Where  $x'$  and  $y'$  are now uncoupled coordinates that when Fourier transformed provide the uncorrelated power spectrum. With the fitting complete we can now adjust our time series in order to get a replication of the lateral trajectory.

## 5.2 Rotations and Asymmetric particles

Rotational motion is something that is not often necessarily considered when characterising Brownian motion, often because separating the contributions from rotational and translational motion is challenging. Depending on the rotational and translational trap stiffness the collected QPD signal will be aliased and typical calibration techniques cannot characterise the particle and trap interactions. This is often why most of the research into trapping asymmetric objects does not delve into power spectra analysis, as there is no real way of modelling the QPD response from an asymmetric object.

Now for isotropic scatterers any rotation is often not an issue when it comes to QPD analysis, even if a sphere rotates  $180^\circ$  the scattering should be identical (assuming its relative position is the same). Now \*ott\* deals with both translations and rotations by moving the beam itself and computing the scattering from by once again expanding the spherical wave functions, the problem that arises from this is that the portion of the spherical wave that is evaluated by the QPD will pick up said rotation and produce a non-zero signal even if the scatterer in question is isotropic. This means we need to counter rotate the total field prior to collecting the QPD signal, this captures the effects of an anisotropic scatterer but has no effect for an isotropic scatterer. As a test the QPD response from an isotropic sphere of  $1.57 \mu m$  was collected at multiple angles, between  $0$  and  $2\pi$ , then as a comparison a symmetrical and 1:2 dimer were also subjected to the same rotations and their QPD responses evaluated.

Where on the left we have an isotropic sphere, then a symmetrical dimer, and lastly a 1:2 dimer. The left most plot shows that simply using the inverted rotation matrix is

Chapter 5. Detection and Characterisation of rotational spherical aggregate  
rotational dynamics  
sufficient to prevent rotation effects being double counted. For dimers however, rotating  
about a given axis gives us a clear change in the signal for even a slight rotation about  
any axis.

### 5.3 Power Spectra of single sphere vs spherical aggregates

In order to verify that the QPD is outputting correct signals we first compared the module to the only other known instance of simulating a QPD response, that being the work of [Rorrbach](#). In their paper they looked at the signal response produced by a single sphere ( $r = 150 \text{ nm}$ ,  $n = 1.57$ ) being scanned along the three Cartesian axis in the proximity of a  $1064 \text{ nm}$  NIR beam with a numerical aperture of 1.2. As shown by fig 2.7 the two responses are remarkably accurate close to the origin; with only slight deviations as you move past the harmonic region, the difference can be explained due to how the two evaluate the total fields. Where in our case the incident and scattered fields are reduced to 0 at the origin, whereas Rohrbach's work evaluates the fields the fields as being non-zero at all points, as you move beyond the origin this discrepancy grows.

Since we are only interested in the dynamics of spherical aggregates upon reaching equilibrium we do not need to be concerned about the deviation from Rohrbach's results so long as the particle's displacement does not exceed the linear region at the origin. The axial response curve is slightly more involved, requiring that the condenser lens numerical aperture is adjusted until a harmonic response curve is achieved [\[Friedrich2012\]](#).

## Chapter 5. Detection and Characterisation of rotational spherical aggregate rotational dynamics

In order to verify that the QPD can accurately capture the dynamics of the target particle we first simulated a single sphere ( $a = 1\mu m$ ,  $n = 1.59$ ) in the focus of a  $1064 nm$  laser. Using  $ott$  the trap stiffness is computed by applying a linear fit to the force-displacement curve along the x and y axis'; for a linearly polarised trap the gradient force is greater in the polarisation direction than transverse case. We see this reflected in the simulated QPD, the fitted Lorentzian curves have different corner frequencies indicating that the beam's polarisation is influencing the dynamics of the trap.

Next we consider a dimer composed of two sphere's similar to the previous sphere, we again apply the QPD module to reproduce the power spectrum. Previous experimental work found that a pair of trapped beads would half the corner frequency from the reported power spectra. However, in our own simulations we see instead an increase in the expected trapping force from our QPD method, with the maximum trap stiffness expected for a dimer of size ratio 5. Compared to  $ott$  in which the maximum trapping strength is expected at a size ratio of 2. This can be somewhat explained by the fact that as the second sphere shrinks the centre of diffusion approaches the centre of the larger sphere and thus the dimer's orientational behaviour is similar to a single sphere, only subject to slight Brownian motion. Therefore one should expect that for aggregates containing multiple sized particles (e.g. cellular samples) typical characterisation techniques may over estimate the strength of the trap.

## 5.4 Monitoring Stochastic rotational motion using static light scattering

Orientational dynamics to an anisotropically scattering shape are difficult to characterise due to the coupling of rotational and translational effects. As shown in the previous chapter the dynamics of even simple dimers are heavily dependent on the particle's position and orientation, this is reflected in literature where several engineering solutions have been devised to decouple translational and orientational motion [ , ].

While a majority of latter work has been focused on nano-particles (falling into the Rayleigh Regime) and utilising florescence

### 5.4.1 Coordinate System

In the case of our probe beam the  $+z$  direction points from the surface of the probe directly to the centre of diffusion in our dimer, with the  $+y$  direction pointing towards what would be our trapping beam, and the  $+x$  direction pointing into the page. The origin of our coordinate system is fixed on the centre of the focus of our trapping beam, meaning as our dimer's centre of diffusion moves the origin is kept constant.

### 5.4.2 Beam

The probe is defined as a plane wave by setting the Gaussian beam parameter  $C_B$  to 0. We also say the beam is un-polarized by defining the Stokes vector as  $[1, 0, 0, 0]$ . The plane wave in *mstm* is given by (2.11).

### 5.4.3 Dimer

The dimer is defined by two spheres, in the trapping frame this would be orientated by  $s = [0, 0, 1]$  however in our scattering set up this is rotated to  $s = [-1, 0, 0]$  as the large sphere is furthest from the trapping beam. We scale the position of each sphere by the factor L:

$$L = \frac{1}{k} = \frac{\lambda}{2\pi} \quad (5.10)$$

Where  $\lambda$  is the wavelength of light and is given in nanometres, this means every position must be also provided in nanometres.

### 5.4.4 Detectors and Pixels

Each detector is placed roughly  $2 \times 10^5 nm$  from the dimer (can be adjusted later for testing), with the position of the detector being defined by the polar and azimuth angles ( $\theta$  &  $\phi$  respectively) such that:

$$[x_{fiber}, y_{fiber}, z_{fiber}] = [r\cos(\phi)\sin(\theta), r\sin(\phi)\sin(\theta), r\cos(\theta)] \quad (5.11)$$

So if you were to place the fibres in the trapping frames x-y plane (i.e. flat against the cover slip in a covenantal trapping context), in the probe beam frame will only have x and z components. The orientation of the detector is just the -ve of its position and not scaled by the distance term r, the orientation being the vector from the origin of the detector to the center of the dimer.

Pixels can be thought of as points lying on the surface of the detector, by getting the spherical coordinates of each pixel we can compute the intensity at each point on the detector, allowing us to determine the average intensity on a given detector.

Where each point is first scaled to the size of the detector - for now we assume a radius of  $2.5 \times 10^4 \text{ nm}$  - and then translated from its position on the surface of the detector to the main coordinate system. Their orientation is treated much in the same as the detector's orientation, being its -ve position and scaled down by the radial distance from the dimer to the pixel, making it a unit vector. From their position we can also grab their spherical coordinates to create a list of points for *mstm* to evaluate. In order to accurately describe any detector surface we can use a Householder transformation to get the perpendicular circular surface of any vector.

This allows us to define the surface of any detector perpendicular to the origin of our coordinate system, we can freely choose the size and resolution of our fibre's. For every pixel we define the spherical coordinates relative to our origin, this is added to a list of  $\theta, \phi$  pairs that are evaluated by *mstm*.

## 5.5 Interpretation of scattering data into orientation estimates

Consider a dimer in the optical trap (Fig. 5.1a), we can define at any point in time a unit vector  $\hat{s}$  pointing from the centre of the larger sphere to the centre of the smaller sphere. A plane wave probe beam is incident on the trapping laser, is incident on the dimer, generating a scattering pattern dependent on the dimer's orientation  $I(\hat{s}, \theta, \phi)$  which

can be computed using *mstm* [**I.Mishchenko1996**]. To represent the experimental set up consisting of a set of optical fibres recording scattered light, we choose four sets of spherical angles  $[(\theta_1, \phi_1), (\theta_2, \phi_2), (\theta_3, \phi_3), (\theta_4, \phi_4)]$  and record the calculated intensity at each angle  $I(\hat{s}, \theta_k, \phi_k)$ .

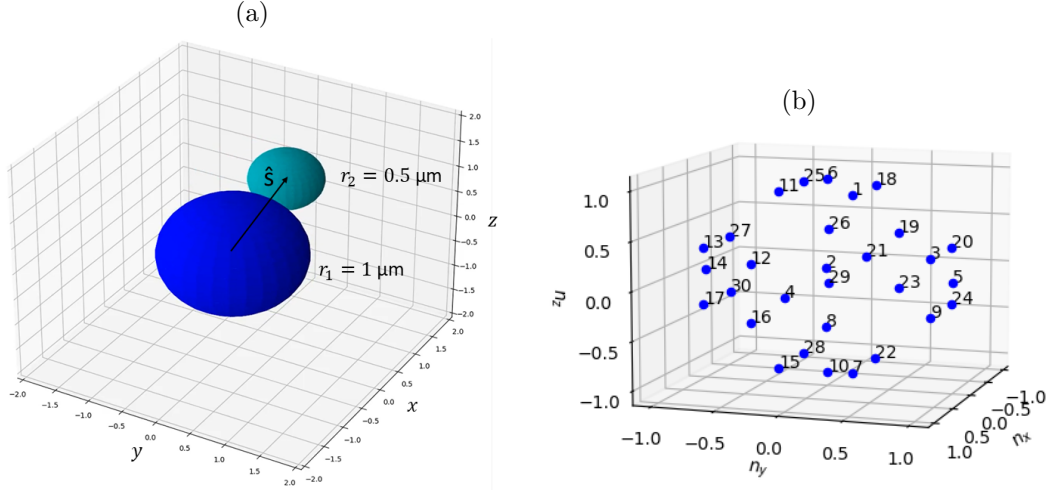


Figure 5.1: (a) Example dimer in orientation  $\hat{s}$ , (b) 30 Reference orientations represented by vectors pointing from  $[0,0,0]$  to each point

Our goal is to determine the orientation of the trapped dimer based on the measured intensity  $I(\hat{n}, \theta_k)$ . Rather than aim immediately for an exact estimate of the dimer's orientation, for the purposes of interpretation of the scattering and optimisation of the measurement setup it is more convenient to discretize the possible orientation space into a number of possible reference orientations, which we can then use as 'classification categories' in a neural network methodology to map scattering data to orientation (see below for further discussion). Here we choose  $n_{ref} = 30$  reference orientations  $\hat{n}_\alpha$  evenly distributed on a unit sphere [**Reyuthor2006**] (Figure 5.1b) leading to a maximum nearest-neighbour spacing between two neighbouring reference orientations of 0.895 radians. Using MSTM we compute the raw intensities at each of the mea-

surement angles that would be generated by a dimer in each reference orientation,  $I(\hat{\mathbf{n}}_\alpha, \theta_k)$ . While the number and position of detection fibres is technically arbitrary there are several constraining factors that limit our ability to infer useful information from the trapped object, see Section ?? for a detailed breakdown of our choice of detection angles. The raw intensities are normalized according to:

$$y_k(\hat{\mathbf{n}}_\alpha) = \frac{I(\hat{\mathbf{n}}_\alpha, \theta_k) - \langle I(\hat{\mathbf{n}}, \theta_k) \rangle}{\langle I^2(\hat{\mathbf{n}}, \theta_k) \rangle - \langle I(\hat{\mathbf{n}}, \theta_k) \rangle^2} \quad (5.12)$$

where the denominator is simply the standard deviation across the set of values  $I(\hat{\mathbf{n}}, \theta_k)$ . The reference orientations, raw intensities, and scaled signals are given in Tables ?? and ??.

Note that the collected scattering signals are not necessarily simply related to their associated reference orientations: as is well known from such examples of the inverse scattering problem. While it is trivial to compute the light scattering pattern for any given particle with any particular characteristic (i.e. size, shape, or orientation), inferring the light scattering from a unknown particle to determine said characteristic is incredibly difficult due to complex mapping between scattering and said characteristic. Even if the orientation space is divided evenly between reference orientation the subsequent signal space ends up being appearing mixed making simple comparisons of signals useless for inferring information on the particle. Shown below is two clusters of orientation vectors and there respective measured scattering signals - the points have been coloured based on their proximity to the centre of their respective cluster. While the orientation space appears tightly packed and ordered the signal space quickly spreads

## Chapter 5. Detection and Characterisation of rotational spherical aggregate rotational dynamics

out in an asymmetric fashion. Furthermore as seen in Fig 5.2b the signal mapping can intersect itself which only further increases the complexity. While in some instances the mapping between one reference orientation and another is discrete, in other instances the mapping becomes far more complex to discern.

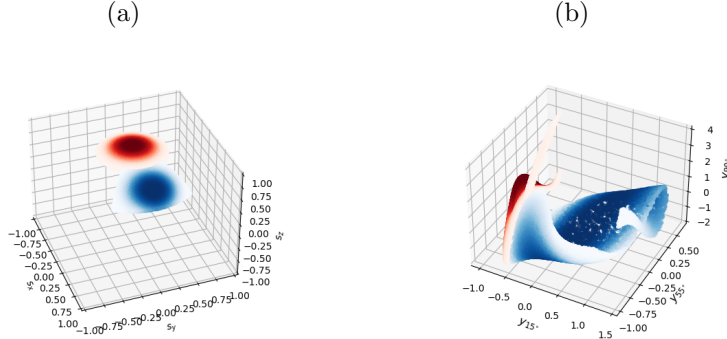


Figure 5.2: (a) Distribution of orientation vectors and (b) their respective scattering signals. Points are coloured according to their distance from the centre of each cluster (red points centred around  $[0.00, 0.00, 1.00]$ , blue points centred at  $[0.71, 0.00, 0.71]$ )

Nevertheless, at least where the uncertainty in signal measurements is low (see below), we can predict the orientation from the scattering by utilising computational techniques such as neural networks. We thus utilised the Python machine learning program *scikit-learn* [**Pedregosa2011**] to build a neural network for identifying the dimer's orientation from its light scattering signal. The network was trained by generating a database of random orientation vectors, calculating the corresponding light scattering signals, and then using the network to estimate the probability of a given signal coming from a dimer in a given reference orientation. The network's loss function was evaluated and used to improve the estimation, the network being trained until the improvement in the loss function was less than 0.0001.

Importantly, the estimation provided by the neural network can be improved further

## Chapter 5. Detection and Characterisation of rotational spherical aggregate rotational dynamics

by accounting for any prior information we know about the dimer, utilising Bayesian inference to update the neural network's estimation:

$$p(\hat{\mathbf{n}}_\alpha | y_k(\hat{\mathbf{s}})) = \frac{p(y_k(\hat{\mathbf{s}}) | \hat{\mathbf{n}}_\alpha) p(\hat{\mathbf{n}}_\alpha)}{p(y_k(\hat{\mathbf{s}}))} \quad (5.13)$$

where  $p(\hat{\mathbf{n}}_\alpha)$  and  $p(y_1, y_2, y_3)$  are the prior estimates of the distributions of particle orientations and instantaneous signals, respectively. *Without* any prior evidence we must assume that the orientation prior of the dimer  $p(\hat{\mathbf{n}}_\alpha)$  is uniform. However, inference about the dimer's possible current orientation from knowledge of previous measurements can be used to inform our estimate of  $p(\hat{\mathbf{n}}_\alpha)$ . The latter prior  $p(y)$  is the probability of measuring a signal  $(y_1, y_2, y_3)$ . This is given by taking the discrete integral over the collection of reference orientations:

$$p(y_1, y_2, y_3, y_4) = \sum_{\alpha=1}^{n_{\text{ref}}} p(y_1, y_2, y_3, y_4 | \hat{\mathbf{n}}_\alpha) p(\hat{\mathbf{n}}_\alpha) \quad (5.14)$$

From (5.13) we obtain the key result, a mass probability distribution denoting the probability that our dimer is in orientation  $\hat{\mathbf{n}}_\alpha$  given a measured signal  $(y_1, y_2, y_3)$ , *i.e.* an estimated mapping from scattering measurement to orientation estimate.

### 5.5.1 Calculation of error

To evaluate the above estimation of dimer orientation from scattering signal, we use a Brownian simulation of a dimer in the optical trap (Section 5.5.2) to compare estimated most probable reference orientation, derived from the dimer's scattering through Eq. (5.13), with the dimer's known *actual* orientation  $\hat{\mathbf{s}}$ . MSTM provides calculated

light scattering from the simulated dimer  $I(\hat{\mathbf{s}}, \theta)$  and we use (5.12) to obtain normalized values at each measurement angle  $\theta_k$ ,  $y_1(\hat{\mathbf{s}})$ ,  $y_2(\hat{\mathbf{s}})$ ,  $y_3(\hat{\mathbf{s}})$ , from which we obtain  $p(\hat{\mathbf{n}}_\alpha \parallel y_1, y_2, y_3)$ . Because we know the actual orientation  $\hat{\mathbf{s}}$  we can measure the error in the model's estimate by comparing the reference orientation closest to  $\hat{\mathbf{s}}$ , denoted as  $\hat{\mathbf{n}}_{best}$ , with the most probable predicted orientation from Eq. (5.13). An ideal result would be one where the probability distribution is 0 for every  $\hat{\mathbf{n}}$  apart from  $\hat{\mathbf{n}}_{best}$ :

$$p_{best} = \begin{cases} 1 & \text{when } \hat{\mathbf{n}}_\alpha = \hat{\mathbf{n}}_{best} \\ 0 & \text{anywhere else} \end{cases} \quad (5.15)$$

In reality the distribution from Eq. (5.13) will assign some non-zero probability to every reference orientation, leading to some level 'confidence' in orientation prediction, which can be quantified by calculating the Kullback-Leibler divergence  $K_l$  between the two distributions:

$$K_{l,\#}(p_{best} \parallel p(\hat{\mathbf{n}}_\alpha | y_1, y_2, y_3)) = p_{best} \ln \left[ \frac{p_{best}}{p(\hat{\mathbf{n}}_{best} | y_1, y_2, y_3))} \right] \quad (5.16)$$

where a larger value of  $K_l$  indicates that our model is less confident in its prediction of the dimer's orientation. The divergence  $K_l$  thus illustrates the 'spread' in the estimated dimer orientation probability — a distribution strongly peaked at some value would give us more confidence in that value than a near-uniform distribution where the scattering measurement could imply a wide range of possible orientations — but it does not directly indicate our estimates actual accuracy, that can be simply defined as the percentage of our estimations that are correct.

### 5.5.2 Brownian Simulation

We use the Brownian OT package developed by Fung *et al* [Vigilante2020Brownian'OT] to simulate the motion of an asymmetric dimer (Figure 5.1a) within an optical trap. Brownian OT combines MSTM [Mishchenko1996MSTM] and “Optical Tweezer Toolbox” (*ott*) [Lenton2020] to simulate the motion of arbitrary shaped sphere clusters. We simulate the motion of a dimer trapped in a highly focused Gaussian beam by calculating the optical forces imparted by the laser, and the Brownian force due to the surrounding fluid. MSTM provides the necessary T-matrix to compute the optical force via *ott*. The Brownian force is found by computing the dimer’s diffusion tensor according to the analytical solutions provided by Nir and Acrivos [nir·acrivos·1973]. We simulated a polystyrene dimer ( $n = 1.59$ ) in a suspension of water ( $n_{med} = 1.33$ ) over the course of 1 s with a simulation time step of  $1 \times 10^{-5}$  s. We placed the dimer 4 microns below the trap focus at an angle 30° from the horizontal, the resulting trajectory is shown below in Sec 5.5.4. We chose these initial parameters because it demonstrates our model’s performance in non steady state conditions.

The exact number of detectors was initially assumed to be arbitrary, in that it made no difference to our estimate whether we used 2 angles or 200. For practical purposes it seemed beneficial that we demonstrate our method works for a minimal number of detection angles, as geometric constraints come into play when trying to install a high number of detection fibres for any optical tweezer set up.

When all of the detectors lie in the same plane the expected signal can appear identical despite the dimer being in completely different orientations. This is shown in

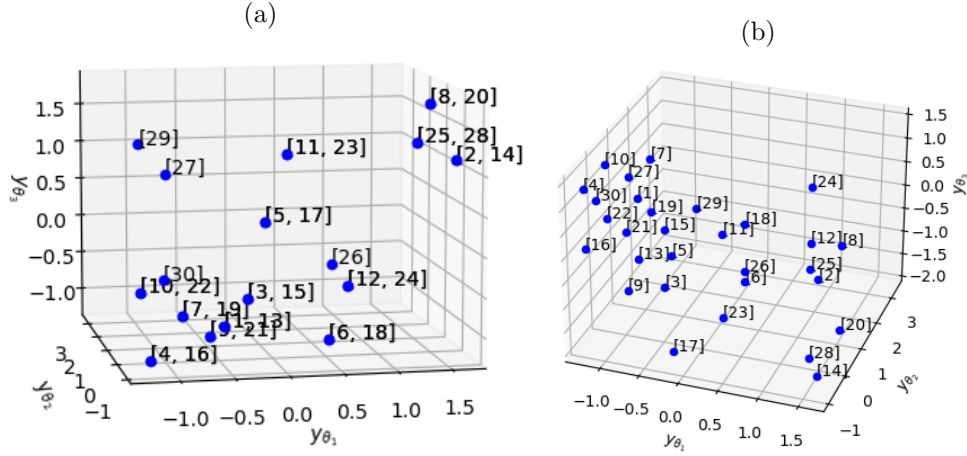


Figure 5.3: Expected scattered signals from reference orientations -see fig 5.1 - when: (a) all three detectors are in the X-Y plane, (b) when 1 detector is raised out of the X-Y plane.

Figure 5.3 which plots the expected signals from 30 reference orientations, each point is labelled with its corresponding reference orientation, the fact that points have multiple labels is because the dimer's scattering is indistinguishable in these two reference orientation. It should be noted that these pairs are reflected in one or more axis which suggests that these are due to the arrangement of our detectors. More specifically, if the detectors are placed say in the x-y plane then only when the dimer is pointed nearly fully upright will the expected signal be entirely unique. This is illustrative of the difficulty behind the inverse light scattering problem; as one cannot always map a given signal to a particular parameter value.

To remedy this we raise the third detector out of the x-y plane; as such the expected signals from each reference orientation is unique. As seen between Figures 5.3a & b each reference orientation now has a unique scattering signal, though with only three detectors the difference in expected signals can appear insignificant. By adding a 4<sup>th</sup> detector we can differentiate signals more reliably, improving the neural networks

performance. In line with our goal of making this method viable in a laboratory setting we decided not to increase the number of detectors further than 4.

### 5.5.3 Testing the Model

Using our simulation from Section 5.5.2 we simulated the motion of a silica dimer ( $n = 1.45$ ) trapped in water ( $n = 1.33$ ) within a 5 mW optical trap. The trapping laser is 1064nm NIR focused through a 1.25 NA objective. The dimer is comprised of two tangent spheres with radii  $1\mu\text{m}$  and  $0.5\mu\text{m}$  respectively. We simulated the first 10 seconds of motion, calculating the orientation and position every 1 ms.

We applied Eq. (5.13), taking the reference orientation with the highest probability as our estimate of the dimer's instantaneous orientation  $\hat{\mathbf{n}}_{est}$ . To visualise the model's performance we plotted the radial distance between our estimation  $\hat{\mathbf{n}}_{est}$  and the dimer's *actual* instantaneous orientation  $\hat{\mathbf{s}}$  versus time. For comparison, we also plotted the radian distance between the dimer's instantaneous orientation and the closest reference orientation, denoted  $\hat{\mathbf{n}}_{best}$ . The dotted line indicates the maximum radian distance (0.896 radians) between two *neighbouring* reference orientations: if we are under this line then we know our estimate is at least neighbouring the best result. Assuming a uniform prior of the reference orientations  $p(\hat{\mathbf{n}}_\alpha)$  the neural network's predictions ( $\hat{\mathbf{n}}_{est}$  from Eq. (5.13)) are at times reasonable, but there are significant large and random jumps away from the correct result (Fig. 5.4).

One reason we observe such large jumps in orientation estimated from scattering signals is that there is no simple correlation between the 'distance in scattering space' between scattering signals from two different orientations, and their separation in orien-

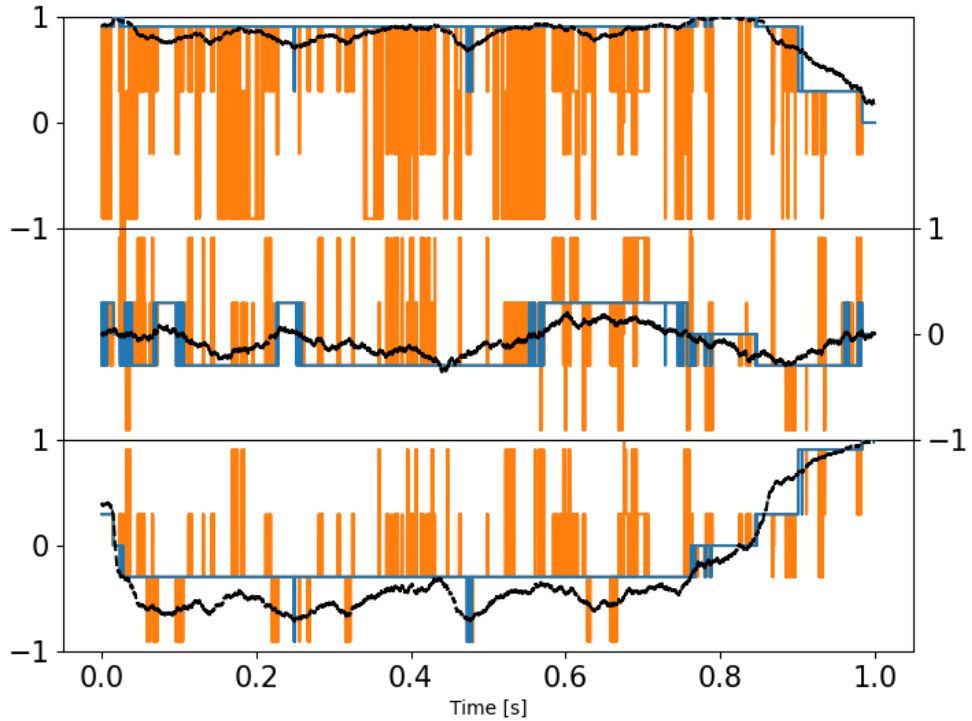


Figure 5.4: Model's estimation of dimer orientation over the simulation time, assuming uniform prior  $p(\hat{\mathbf{n}}_\alpha)$ , broken up into x, y, and z components for clarity. Blue line denotes the best result we can achieve (the reference orientation  $\hat{\mathbf{n}}_{best}$  that is closest to the actual orientation), orange line denotes the result provided by eq 5.13: where the orange line is not visible, the model's prediction agrees with  $\hat{\mathbf{n}}_{best}$ . Dotted black line is the instantaneous orientation  $\hat{\mathbf{s}}$ .

tation space: even a large change in orientation can involve a small change in scattering. Combining this fact with use of a uniform prior, indicating essentially no knowledge of how orientation should behave, there is no constraint on how much estimated orientation can change from time-step to time-step. To improve the estimation we can therefore use knowledge of the physical limitations of the object in the trap and its dynamics, imposing a more physically grounded prior, accounting in this case for the fact that the motion of the dimer is limited due to the trap stiffness. Here the prior of

Chapter 5. Detection and Characterisation of rotational spherical aggregate  
rotational dynamics

the reference orientations  $p(\hat{\mathbf{n}}_\alpha)$  was redefined at each time step as a Boltzmann distribution of the physical distance between the previous estimate  $\hat{\mathbf{n}}_{est}(t - \Delta t)$  and each reference orientation  $\hat{\mathbf{n}}_\alpha$ . Put simply, we are reweighing our estimation based on the size of rotation required, with smaller movements being favoured over large movements:

$$p(\hat{\mathbf{n}}_\alpha) = \frac{e^{\beta(\hat{\mathbf{n}}_\alpha \cdot \hat{\mathbf{n}}_{est}(t - \Delta t))}}{\sum_{\alpha=1}^{n_{ref}} e^{\beta(\hat{\mathbf{n}}_\alpha \cdot \hat{\mathbf{n}}_{est}(t - \Delta t))}} \quad (5.17)$$

Here  $\beta$  is a weighting factor describing the dimer's freedom of motion within the trap. As shown in Figure 5.5 implementation of Eq (5.17) helps significantly reduce the large random excursions of estimated orientation away from the 'best' result.

The simulation data from Section 5.5.2 was used to evaluate our model's performance — covered in Section 5.5.1. By summing the divergence of each measurement across the entire simulation we get an evaluation of how well the model performed in estimating the dimer's orientation. To compare the effects of changing certain parameters on the performance of our model we compare our result of  $K_{l,total}$  to a worst case scenario and evaluate how much it improves upon this, denoted as  $F(K_l)$ :

$$K_{l, total} = \sum_{\#=1}^{timesteps} K_{l,\#} \quad (5.18)$$

$$K_{l, worst} = \sum_{\#=1}^{timesteps} \ln \left[ \frac{1}{1/n_{ref}} \right] \quad (5.19)$$

$$F(K_l) = \frac{K_{l, worst}}{K_{l, total}} \quad (5.20)$$

The worst case scenario is akin to randomly choosing a reference orientation at

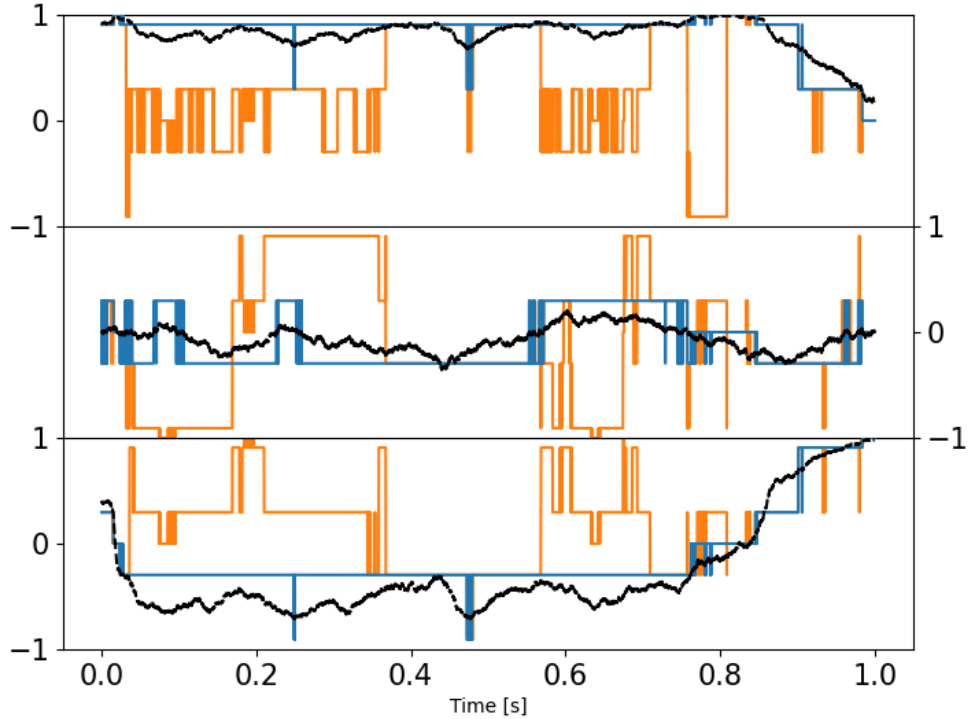


Figure 5.5: Estimation of dimer orientation with  $p(\hat{\mathbf{n}}_\alpha)$  defined by Eq (5.17). Blue line denotes the best result we can achieve, orange line denotes the result provided by eq 5.13. Dotted black line is the instantaneous orientation  $\hat{\mathbf{s}}$  (see Section ??).

each time step. The greater the value of  $F(K_l)$ , the better our model's confidence is in characterising the dimer's motion. Because our model is dependent on several parameters we need to a sophisticated method for understanding how these parameters correlate with  $F(K_l)$ .

#### 5.5.4 Asymmetric dimer dynamics

A simulation of a asymmetric dimer ( $a_1 = 1 \mu\text{m}$ ,  $a_2 = 0.5 \mu\text{m}$ ) trapped in an off-axis trapping orientation was used as a test case for our model, since it was previously shown that dimers can be optically rotated

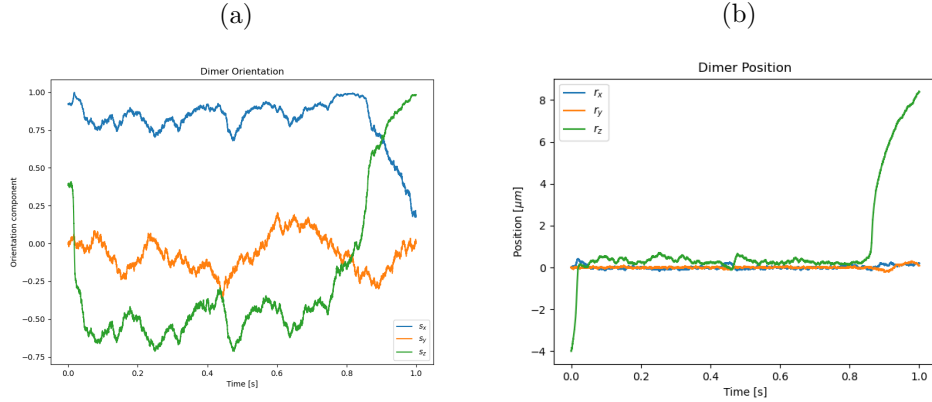


Figure 5.6: Simulation results of: (a) the dimer’s orientation vector with time, (b) the dimer’s [x,y,z] position with time.

In the simulations of Vigilante *et al.* [Vigilante2020BrownianOT], trapped symmetrical dimers were investigated; their findings showed that the optical torque on the dimer goes to zero while aligned vertically and is at its maximum in a horizontal alignment. However as seen in Figure 5.6 asymmetric dimers demonstrate dynamics that do not immediately achieve steady state. We chose to use asymmetric dimers as our benchmark due to this fact, as its orientational motion is far more complex than a symmetric dimer. In the future we hope to further investigate the motion of asymmetric dimers.

### 5.5.5 Accounting for sources of error in light scattering measurements

When it comes to analysing light scattering from any size particle, error analysis becomes a significant factor. Typically this can be accounted for by averaging over long periods of time to get an assessment of the steady state conditions of the target particle. However in our case where we wish to know the instantaneous orientation, we instead have to rely on our understanding of how uncertainty can effect our model’s

performance. We identified two areas which are likely sources of error in our estimation: firstly, an incorrect modelling of the target particle, and secondly, signal noise arising from experimental factors. We highlight how we address these areas below.

### **Impact of incorrect dimer sizing**

One of the main limitations of our model is that we assume that the dimer being modelled in MSTM is accurate to the dimer being trapped in the optical tweezer. Sizing molecules accurately is a significant challenge for single particle analysis so there is bound to be some uncertainty with the measurements.

We ran our model 3 times with the neural net being trained on a dimer of size ratio 1 : 1.95, 1 : 2.00 and 1 : 2.05.

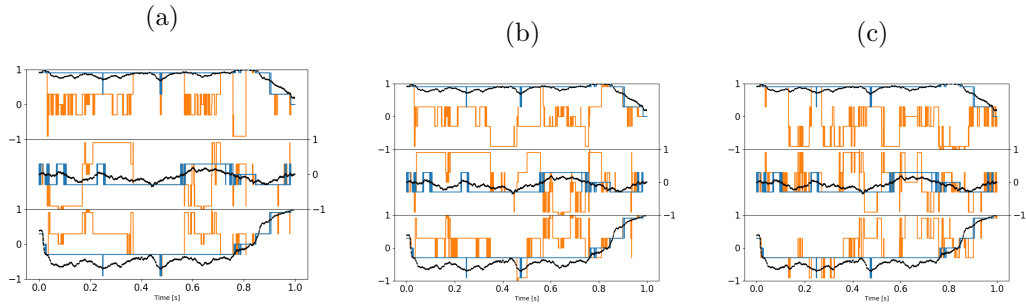


Figure 5.7: Model estimates of orientation when neural net has been trained on dimer of size ratio: (a) 1:2 [ $F(K_l) = 9.456$ ], (b) 1:2.05 [ $F(K_l) = 1.324$ ], (c) 1:1.95 [ $F(K_l) = 1.325$ ] ( $n_{refs} = 30$ )

As can be seen from Fig 5.7 even the slightest change in size ratio makes a very significant difference to the performance of our model. This amounts to just over 100 nm in the dimer's overall size, yet results in our model being correct from over 90 % of the time to now as low as 30 %. This highlights the importance of correctly sizing trapped entities before performing any in depth analysis of the scattering pattern, as even the slightest deviation can have a serious impact. We addressed this by increasing the

number of available reference orientations from 30 to 126 (following the same procedure as given by [Rey2006] to evenly space out the coordinates) and increasing the weighting factor in Eq 5.17. While this didn't have a significant improvement on the overall accuracy of the model, in the worst case having a slight increase from 30.5 % to 40.3 %, it did help to significantly reduce the magnitude between our model's estimations and the dimer's motion as seen below in Fig 5.8.

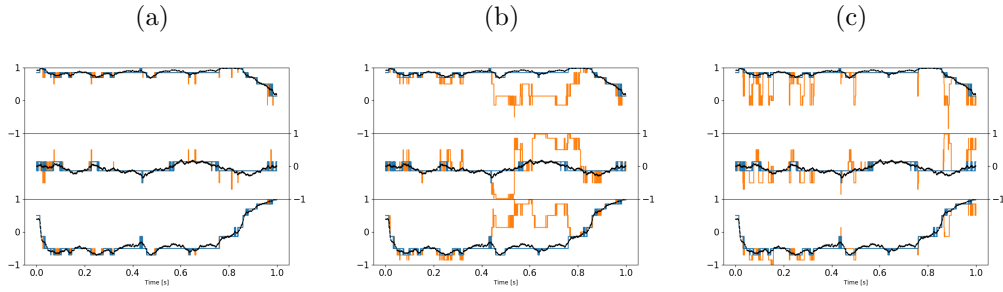


Figure 5.8: Model estimates of orientation when neural net has been trained on dimer of size ratio: (a) 1:2 [ $F(K_l) = 11.756$ ], (b) 1:2.05 [ $F(K_l) = 1.233$ ], (c) 1:1.95 [ $F(K_l) = 2.128$ ], ( $n_{refs} = 126$ )

Notably the increasing the number of reference orientations had a greater effect when our neural network was trained on a 1:1.95 dimer than a 1:2.05 dimer. This suggests that overshooting our size estimate will be less detrimental to our estimation. Notably if the our sizing is off the neural network does not predict a smooth motion within the trap; instead predicting that the dimer is jumping back and forth between different orientations. This suggest that we can narrow down our estimate of the particle's size by assessing how the dimer is reorienting within the trap, as we should expect a smooth continuos prediction. Since we are working with a spherical dimer it also stands to reason that techniques such as image analysis could be used in part to address this, so long as the trapped entity is sufficiently illuminated.

**Impact of measurement noise on model predictions** So far a key assumption of the neural network implementation is that the detected scattering signal has no uncertainty associated with it. In reality of course scattering signals will always have some non-zero measurement noise. This can be attributed to a variety of factors, from a measurement bias in the detector, to the Brownian motion of the dimer itself. To explore the impact of measurement uncertainty on orientation estimation model performance we introduce a Gaussian noise to the measured signal:

$$I(\hat{\mathbf{s}}) = I(\hat{\mathbf{s}}) \pm \epsilon I(\hat{\mathbf{s}}) \quad (5.21)$$

where  $\epsilon$  is the percentage error associated with the scattering signal. Figure 5.9 shows the performance of the model at a range of  $\epsilon$  using in-plane detector angles  $15^\circ$ ,  $55^\circ$ ,  $90^\circ$  and out-of-plane detector at  $75^\circ$ , with  $\beta$  set to 1:

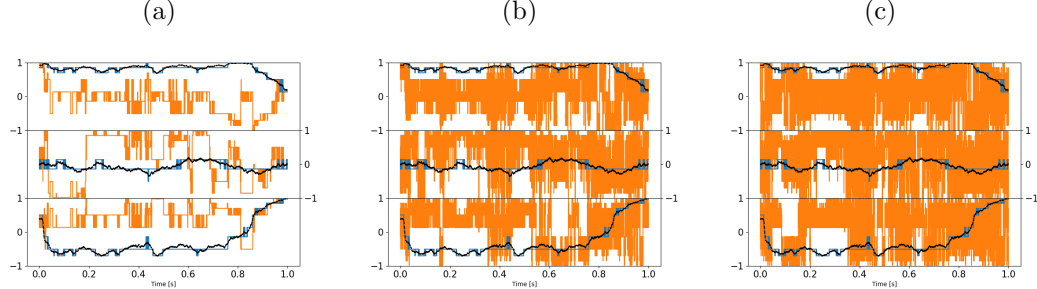


Figure 5.9: Model prediction for signal error of (a) 1% [ $F(K_l) = 7.246$ ], (b) 15% [ $F(K_l) = 0.511$ ], and (c) 25% [ $F(K_l) = 0.536$ ].

As can be seen from Figure 5.9, the inclusion of signal noise quickly leads to a decrease in the model's performance. This is due to an inherent feature of the inverse scattering problem: two distinct regions in orientation space can become heavily intertwined and thus no longer well separated when mapped to intensity space (even though

the mapping remains continuous): so even small uncertainties in the scattering data can lead to large 'mistakes' in the choice of orientation by the neural network. (Indeed if this was not the case the inverse scattering problem would be quite simple.)

To reduce the effects of the signal noise we took the time average of the expected signal over  $0.001\text{s}$  and then had our neural network estimate the orientation based on the average signal.

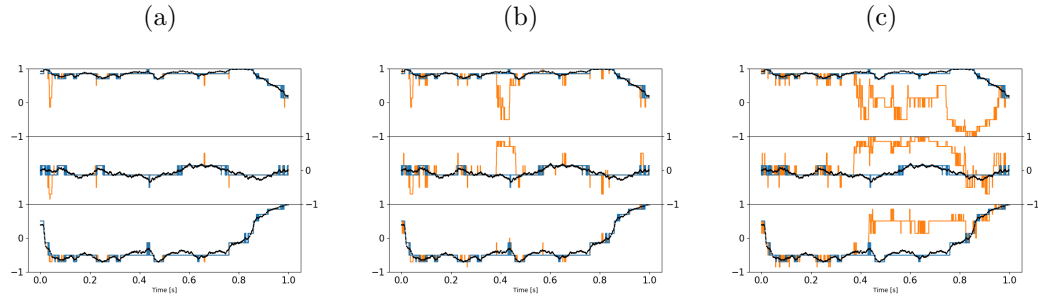


Figure 5.10: Model prediction for signal error of (a) 1% [ $F(K_l) = 4.823$ ], (b) 15% [ $F(K_l) = 1.494$ ], and (c) 25% [ $F(K_l) = 0.882$ ], time averaged over 1 ms

This resulted in a reduction in the overall signal noise and provided a higher degree of accuracy for our model. There appears to be no clear correlation between the length over which we time average and the performance of our model. Time averaging over every  $0.05\text{s}$  resulted in a drastically worse performance; this is due to the fact that over longer time periods there is greater uncertainty regarding how the dimer's orientation has changed, thus tracking the instantaneous orientation becomes harder for the neural network. Fortunately, time averaging even over  $1\text{ ms}$  seems to provide a satisfactory estimation of the dimer's angular dynamics within the optical trap.

From the above discussion it's clear that estimation of the dimer's orientation is a problem that can be endlessly tuned to fully maximise our end result. Here we sim-

plify the problem somewhat by employing a relatively small finite number of 'reference orientations' to map between scattering and dimer orientation: the precision of estimation could be improved by utilising a greater number of reference orientations, although there remains a balance between the realisable precision of orientation estimate and the noise level of the scattering measurement. Another avenue to further explore would be using the method to optimise the choice of detection angles, essentially to find the region in the mapping between measured scattering and orientation that others the best degree of confidence through optimal separation of scattering signals for distinct orientations. For sequences of data such as dynamic measurements, a further potential enhancement would be to consider more complex correlations based on prior expectations of the dynamics. Here already we improve the method using a non-uniform prior based on only the immediately previous measurement in time (see Section 2.1): considering a non-uniform grouping of reference orientations might result in a better estimation, if we have information regarding the dimer's preferred axis of rotation.

## 5.6 Conclusion

We have developed a method for measuring the dynamics of an optically-trapped colloidal objects based purely on measurements of the object's light scattering at a small number of detection angles. We demonstrate the method using the orientation of an asymmetric dimer as the dynamic variable and object of interest respectively, but in principle the model can be applied to any characteristic that impacts the light scattering pattern produced by a trapped entity such as size and shape. The MSTM

## Chapter 5. Detection and Characterisation of rotational spherical aggregate rotational dynamics

package is a flexible tool for calculating the light scattering of complex objects using a representation of the object as a set of micro-particles, enabling training of a neural network to enable categorisation of the mapping between scattering and trapped object characteristics. By taking account of the physically realistic behaviour of the trapped object and the characteristics of the trap (which impact the dynamics of the object), the Bayesian inference method can be refined to provide a reliable estimation of object characteristics of interest, even in the presence of measurement noise. Fundamentally, the inverse scattering problem is difficult to solve, since the mapping between object characteristics and scattering can be highly complex. We determined the minimum number of detectors required for a reliable estimation in the presence of measurement noise; furthermore, we demonstrated that the arrangement of these detectors is critical for a reliable estimation of an objects orientation. However, Bayesian inference based on neural network estimation of the mapping provides a powerful method for practical applications, extending the use of optical trapping beyond measuring microscopic force response toward detailed structural and dynamic information about complex trapped entities.

## **Chapter 6**

## **Closing Remarks**

## **Appendix A**

### **Stuff That Didn't Fit Anywhere**

#### **Else**